Integration of Theory to Computations of Spray and Turbulent Flows

by

Jung Eun Park

A Dissertation Presented in Partial Fulfillment
of the Requirements for the Degree
Doctor of Philosophy

Approved October 2022 by the
Graduate Supervisory Committee:

Taewoo Lee, Chair
Huei-Ping Huang
Kangping Chen
Jeonglae Kim
Carl Gardner

ARIZONA STATE UNIVERSITY

December 2022

ABSTRACT

Theoretical analyses of liquid atomization (bulk to droplet conversion) and turbulence have potential to advance the computability of these flows. Instead of relying on full computations or models, fundamental conservation equations can be manipulated to generate partial or full solutions. For example, integral form of the mass and energy for spray flows leads to an explicit relationship between the drop size and liquid velocities. This is an ideal form to integrate with existing computational fluid dynamic (CFD), which is well developed to solve for the liquid velocities, i.e., the momentum equation(s). Theoretical adaption to CFD has been performed for various injection geometries, with results that compare quite well with experimental data. Since the drop size is provided analytically, computational time/cost for simulating spray flows with liquid atomization is no more than single-phase flows. Some advances have also been made on turbulent flows, by using a new set of perspectives on transport, scaling and energy distributions. Conservation equations for turbulence momentum and kinetic energy have been derived in a coordinate frame moving with the local mean velocities, which produce the Reynolds stress components, without modeling. Scaling of the Reynolds stress is also found at the first- and second-gradient levels. Finally, maximum-entropy principle has been used to derive the energy spectra in turbulent flows.

DEDICATION

I would like to thank my advisor Dr. T.-W. Lee.

TABLE OF CONTENTS

Page

LIST OF TABLES v

LIST OF FIGURES vi

CHAPTER

1 INTRODUCTION (PART I) 2

1.1 Liquid Breakup Process to Droplets 2

1.2 Statistical Equilibrium in a Macroscopic Description 3

2 LITERATURE REVIEW 5

2.1 Research on Spray Atomization in Early Decades(~ the 1980s) 5

2.2 Research on Spray Atomization in Modern Decades(the 1980s~2000s) 7

2.3 Research on Spray Atomization in Recent Decades(the 2000s ~) 11

2.4 Modeling of Drop Size Distribution 14

3 MATHEMATICAL FORMULATION 18

3.1 Equations of Conservation: Liquid Jet in a Quiescent Ambient 18

3.2 Equations of Conservation: Liquid Jet with Added Gas Momentum 22

3.3 Validations and Considerations on the D_{32} Quadratic Formulation 24

4 MOMENTUM ANALYSES 32

4.1 The Use of Momentum Analyses 32

4.2 Formulation of Momentum Equations 33

4.3 Validations of Momentum Equations 36

4.4 Methods for Drop Size Distributions 42

4.5 Chapter Summary 54

CHAPTER Page

5 COMPUTATIONAL PROTOCOL FOR SPRAY FLOWS, INCLUDING PRIMARY ATOMIZATION 56

5.1 Basic Spray Geometries 56

5.2 Liquid Jets Atomized by High-Speed Gas Flows 79

5.3 Jets on the Sea Surface Plumes 88

5.4 Liquid Jets in Sydney-Burner Flows 99

5.5 Chapter Summary 109

6 TURBULENCE THEORY (PART II) 112

6.1 A New Set of Turbulence Transport Equations 113

6.2 Scaling in Gradient Profile of Reynolds Stress 132

6.3 Gradient Structure Functions for Reynolds Stress 143

6.4 Maximum Entropy Turbulence Energy Spectra 150

6.5 Chapter Summary 162

REFERENCES 166

APPENDIX

A DERIVATION OF MOMENTUM EQUATIONS 177

LIST OF TABLES

Table Page

5.1. Test Conditions 82

5.2. Boundary Condition Parameters 90

6.1. Coefficients Used in the Functions 144

6.2. Parameters of the Energy Spectra for Various Data Sets 157

LIST OF FIGURES

Figure		Page
2.1.	Illustration of Disintegration on a Liquid Sheet	7
2.2.	Illustration of Surface Instability on the Liquid Sheet	11
3.1.	Dynamic Relation of Drop Size and Velocity, Jet in Quiescent Ambient Gas	26
3.2.	Dynamic Relation of Drop Size and Velocity, Jet with Gas Momentum	27
3.3.	Schematic of the Experimental Setup	29
3.4.	Comparison of SMD with Other Atomization Model and Correlation	31
4.1.	Spatial Development of the Liquid and Gas Velocities	37
4.2.	Density Effects on the Drop Size in Swirl Sprays	40
4.3.	Comparison of Drop Size and Velocity, Shock-Induced Breakup	41
4.4.	Comparison of Discrete Probability, Pressurized-Straight Liquid Jet	44
4.5.	Comparison of Discrete Probability, Liquid Jet in Cross-Flows of Gas	45
4.6.	Comparison of Discrete Probability, Liquid Jet in Coaxial-Flows of Gas	47
4.7.	Comparison of Continuous Probability, Pressurized-Straight Spray	50
4.8.	Comparison of Continuous Probability, Jets in Cross-Flows of Gas	52
4.9.	Comparison of Continuous Probability, Jets in Coaxial-Flows of Gas	53
5.1.	Schematic of the Computational Protocol for Straight Liquid Jets	58
5.2.	Profiles of the Velocity and its Gradient; (a) Radial (b) Axial Centerline	59
5.3.	Comparison of the (a) Drop Velocities (b) Drop Sizes	64
5.4.	Contour Plot of the Drop Number Density, Pressure-Atomized	65
5.5.	Comparison of the SMD, Diesel Spray	66
5.6.	Comparison of the Centerline SMD, Diesel Spray	67

Figure Page

5.7. Simulation for Swirl Sprays 68

5.8. Comparison of (a) Drop Velocities (b) SMD, x = 8~14mm Swirl Spray 70

5.9. Comparison of (a) Drop Velocities (b) SMD, x = 16~20mm Swirl Spray 71

5.10. Global Drop Size Distribution, Swirl Spray 72

5.11. Simulation for Liquid Spray in Cross-Flows 73

5.12. Comparison of (a) Drop Velocity (b) D_{32}, x/d = 138~168, Cross-Flows 74

5.13. Comparison of (a) Drop Velocity (b) D_{32}, x/d = 183~215, Cross-Flows 75

5.14. Comparison of the Volumetric Flux, Spray in Cross-Flows 77

5.15. Global Drop Size Distribution for Liquid Spray in Cross-Flows 78

5.16. Volume Fraction near Injector Exit, Air-Assist Flat Spray 82

5.17. Centerline Velocity and Axial Velocity Gradient, Air-Assist Flat Spray 83

5.18. Particle Tracks, Air-Assist Flat Spray 85

5.19. Comparison of Averaged (a) Particle Velocity (b) D_{32}, Air-Assist Case 1 86

5.20. Comparison of Averaged (a) Particle Velocity (b) D_{32}, Air-Assist Case 2 87

5.21. Simulation Domain for Jets on Sea Surface Plumes 89

5.22. Comparison of the Sea Surface Undulations in Various Wind Speed 91

5.23. Velocity Profiles in the Simulation of Jets on the Sea Surface Plumes 94

5.24. Normal Distributions of Velocity and Drop Size, Sea Surface Plumes 95

5.25. Discrete Probability Distribution of Drop Size, Sea Surface Plumes 96

5.26. Comparison of Drop Size Distributions, U_{10} = 31.3m/s 97

5.27. Comparison of Drop Size Distributions, U_{10} = 41.2 m/s 98

5.28. Comparison of Drop Size Distributions, U_{10} = 47.1 m/s 98

Figure Page

5.29. Simulation Domain including Velocity Field, Jets in Lr = 25mm 101

5.30. Simulation Domain including Velocity Field, Jets in Lr = 80mm 101

5.31. Comparison of Velocity Profiles, Jets in Sydney-Burner Lr = 25mm 103

5.32. Comparison of Velocity Profiles, Jets in Sydney-Burner Lr = 80mm 104

5.33. Comparison of Drop Sizes, Jets in Sydney-Burner Lr = 80mm 105

5.34. DPM Simulation including Particle Tracking and Velocity Field 106

5.35. Drop Size Distribution, Jets in Sydney-Burner Flows Lr = 80mm 107

6.1. The u′ Momentum Budget for the Reynolds Shear Stress Gradient 115

6.2. Schematics of the Dynamics in the Lagrangian Turbulence Transport 117

6.3. Displacement Concept leading to d/dx → d/dy Transform 117

6.4. The u′v′ and dU/dy in Comparison to DNS 120

6.5. Budget for u'^2 Kinetic Energy in Comparison to DNS 122

6.6. Budget for v′ Momentum in Comparison to DNS 124

6.7. Reynolds Shear Stress Gradient Budget, Flat Plate Flow at ZPG 125

6.8. Reproduced Profiles of Basic Turbulence Variables -u′v′, u'^2, and v'^2 126

6.9. Reynolds Shear Stress Gradient Budget, Flat Plate Flow at APG 127

6.10. Turbulence Kinetic Energy u'^2, Iterated Using Transport Equations 131

6.11. Normalized Mean Velocity Profile, Iterated Using Transport Equations 132

6.12. Reproduced u'^{2+} Profiles Showing Progression From Re_τ = 110 to 5200 134

6.13. Total Turbulence Kinetic Energy E and Dissipation Φ, Re_τ = 110 to 5200 ...135

6.14. The du'^{2+}/dy^+ Profiles From Re_τ = 110 to 5200 137

6.15. Comparison of the Scaled Profiles of du'^{2+}/dy^+, Re_τ = 110 to 5200 138

Figure Page

6.16. The (a) dv'^{2+}/dy^{+} Profiles (b) $d^2v'^{2+}/dy^{+2}$ Profiles, From Re_τ = 110 to 650 140

6.17. Comparison of the Scaled Profiles of $d^2v'^{2+}/dy^{+2}$, Re_τ = 1000, 5200 141

6.18. The $d^2u'v'^{+}/dy^{+2}$ Profiles From Re_τ = 110 to 5200 142

6.19. The du'^{2+}/dy^{+} Profiles With Gradient Structure Functions 145

6.20. The $d^2v'^{2+}/dy^{+2}$ Profiles With Gradient Structure Functions 146

6.21. The $d^2u'v'^{+}/dy^{+2}$ Profiles With Gradient Structure Functions 146

6.22. Scaling Factor for the Gradient Structure in Channel Flows 147

6.23. Secondary Peak Structure at High Reynolds Numbers 149

6.24. Comparison $u'(k) \sim m - \log(k)$ with $u'(k) \sim k^{-1/3}$ 154

6.25. Various $u'(k)$ Scaling Used by Equation of Turbulence Energy Spectra 154

6.26. Comparison of Maximum-Entropy Spectra for Re_λ = 71.6 ~ 1500 155

6.27. Comparison of the Turbulence Energy Spectra, Decaying Turbulence 158

6.28. Comparison of the Turbulence Energy Spectra, Two- to Three-Dimension ...159

6.29. Comparison of the Turbulence Energy Spectra, Channel Flows 161

A.1. Description of Reduction in Drag Force to the Local Spray Volume 183

PART I

Spray Atomization Theory and Integration into a Computational Protocol

CHAPTER 1

INTRODUCTION

1.1 Liquid Breakup Process to Droplets

Liquid breakup process consists of serial occurrences. In the preliminary stage, the liquid discharging from an injector undergoes forming processing that depends on the design of the injector. This makes the intended shape of being physically vulnerable, like a liquid column or sheet. In the next stage, it encounters the disintegration of the discharged continuum liquid, as it is subjected to severe drag and shear stress while traveling in a medium like air. This leads to primitive droplets, fragments, or ligaments out of the issuing liquid, called “Primary Atomization”. Subsequently, those resultants experience even further breakup caused by complex reasons likely turbulence dynamics, triggered instabilities, collisions, or heat exchanges surrounding them. This is called “Secondary Atomization”.

Hereafter primary atomization is mainly dealt with, in the view of momentum and kinetic energy exchanges between liquid and gas. Although there are neither identifiable signs nor a watershed moment clearly to distinguish between primary and secondary breakup processes in real, in pursuit of our analytic study we ideally confine our scope to the primary breakup. In addition, isothermal conditions are assumed in order to circumvent intricate analyses, but rather the focus is on constructing a theoretically simpler model. At the completion of primary breakup processes, the thermodynamic equilibrium state is postulated as being reached with maximum entropy.

1.2 Statistical Equilibrium in a Macroscopic Description

During the successive processes of spray breakup, we could set specifically a partial equilibrium state at which the primary atomization is finished. This approximation is possible if we assume a closed system in which the series of spray atomization processes is entirely terminated and reached equilibrium states. Although dissipation, i.e., internal friction, is inherent thereby it could not maintain a perfect closed system, it is still a useful consideration in that we apply integral formalism over a control volume occupied by a fluid and deal with it global extent, which is similar context to Navier-Stokes Equation. Therefore it is like a closed system with steady ambient around. The time duration to reach equilibrium states is called “relaxation time”, and for being a steady state much longer period of time is required than the relaxation time. Ideally, we separate one of the subsystems consisting of a closed system, where primary atomization is being performed and then terminated at its relaxation time. Given that the subsystem states can be described in a macroscopic view, the “statistical equilibrium” characterizes its properties on average. In this manner, the subsystem could be regarded as a nearly closed system, and its relaxation time is proportional to the size of the subsystem [1].

In this regard, we approximate the closed subsystem to a form of control volume where primary atomization is only considered, which is starting from the injection of continuous liquid to a group of discrete droplets being reached statistical equilibrium, for the duration of relaxation time. It is worth noting that statistical description for the given subsystem does not depend on the initial states, which means many parameters related to injector performance, e.g., discharge effect and turbulent intensity, or intermediate events, e.g., distortion or deformation in flow morphology by complex dynamics, can be

excluded. Hence it enables our analysis to be valid over various conditions with different injections under universal principles such as mass, momentum, and energy conservation, essentially rendering better generalized core results.

CHAPTER 2

LITERATURE REVIEW

2.1 Research on Spray Atomization in Early Decades (~ the 1980s)

At that time CFD usage was not prevalent, there were some devised mathematical expressions derived from classical analyses to explain the breakup mechanism of a liquid jet. For instance, instability theories or turbulence characteristics were accounted to predict liquid core dynamics and droplet formation. A liquid jet, emanating from a nozzle and then being fragmented thus evolving into discrete drops through the breakup process, was regarded as being subjected to perturbation, e.g., surface displacement on a liquid jet, induced velocity or pressure fluctuations, and so on.

Linear Instability on Liquid Jet

In those early days, the study on the capillary jet of inviscid liquid without surrounding gas was conducted by Rayleigh in 1878 [2], and he demonstrated axisymmetric surface instability by equating potential and kinetic energies. Accordingly, he derived an equation for the wave growth rate. On top of that, it was postulated that the disturbance with the fastest wave growth rate essentially incurs liquid core breakup, and the wavelength of that disturbance is of the order of drop size. This analysis was advanced by Weber in 1931 [3] with viscous liquid and inviscid coaxial gas stream. From this investigation, he concluded that the fastest growing waves are to be longer in wavelengths, and their growth rates are to be slower. Taylor in 1950 [4] addressed an instability theory based on that, having an acceleration normal to the interface between two fluids with different densities incurs instabilities under certain conditions, whether

the acceleration is directed from the lighter to heavier fluid or vice versa. A further enhancement was achieved by taking into account the aerodynamic effects, from Sterling and Sleicher in 1975 [5]. They considered the influence of density ratio and the relative velocity between liquid and gas, however, the suggestion was limited to uniform relative velocity. Later, Reitz and Bracco in 1982 [6] proposed the general dispersion equation for an axisymmetric liquid jet breakup mechanism to reinforce the previous shortcoming.

Force Balance on Wavy Liquid Sheet

There is a type of spray for which the internal design is specially devised to pull out a liquid in sheet shape rather than cylindrical, one is advantageous to result in small drops. As it is thought that the drop sizes are in the same order as the thickness of the liquid sheet, the apparatus which emanates a thin liquid sheet is used in favor. Long ago, Savart 1833 [7] studied the dynamics of a fluid sheet with the axisymmetric flat or bell-shaped one. The breakup mechanism for a liquid sheet was explored by Dombrowski and Johns in 1963 [8] as illustrated in Fig. 2.1. In their study, the inviscid liquid sheet moving to a stationary gas was assumed. They postulated a wavy attenuating sheet motion governed by the force balance equation, which includes four forces of pressure, surface tension, viscous acting on the sheet, and inertia. Given that the wave amplitude grows as time passes until it reaches a critical value, it was predictable when the sheet disintegration occurs. And this leads to the tearing off the cylindrical-shaped ligaments. Thereafter, the ligament breaks down into droplets due to varicose wave instability.

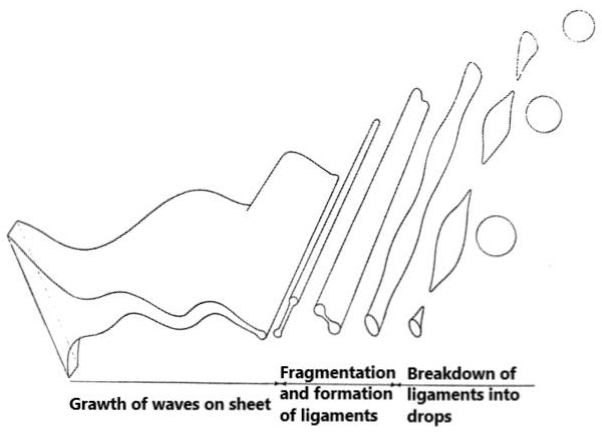

Fig. 2.1 Illustration of disintegration on a liquid sheet. Drawing from Dombrowski and Johns [8]

2.2 Research on Spray Atomization in Modern Decades (the 1980s ~ 2000s)

A stream of interest, coming from industries pursuing optimal fuel injectors for internal combustion engines, drew one's attention to the passage to accomplishing efficiency as well as satisfying environmental standards. The demands came up with CFD as an advantageous tool. Numerous breakup modeling with numerical techniques were pioneered, and it was realized in computational simulations.

Breakup Induced by Turbulence

Faeth et al. in 1995 [9] observed the phenomenological analogies between fully developed turbulent pipe flow with round pressure-atomized spray near the exit where the dense spray region was found, as comparing the flow structures. They assessed that the flow structures are dependent on the turbulence levels at the exit. The primary breakup was incurred by aerodynamic pressure reduction over the liquid tips, which assists the liquid turbulence kinetic energy to provide the surface tension energy needed to form

small drops. Huh et al. in 1998 [10] presented a primary atomization model by jet turbulent fluctuations and wave growth on the jet surface. They addressed that the disturbance, owing to turbulence that originated from shear stress or cavitation through a nozzle, grows over time. Turbulent kinetic energy and energy dissipation rate, which rely on nozzle parameters, were used in deriving the expressions on turbulence length and time scale. Those scales were assumed to be dominant scales for the primary atomization process, thus leading to possible calculation on the primary breakup drop size.

Secondary Breakup Model

O´Rourke and Amsden in 1987 [11] proposed TAB model, i.e., Taylor Analogy Breakup model. This is based on Taylor's theoretic study of the analogy between a distorting and oscillating droplet and a mass-spring-damping system. The idea described such that force corresponds to the aerodynamic interaction between droplet and gas, restoring effect by surface tension, and damping effect by liquid viscosity. Accordingly, an equation of the oscillator was derived from those analogy relations in which the coefficients of the equation are obtained from the relevant physical dependencies. The critical value for the oscillator was set in predicting secondary breakup initiation, i.e., the amplitude of oscillation of the north and south poles equals the drop radius. The production of the subsequent droplets was deemed as being governed by energy conservation, so their energy after the breakup was equated to the that of parent drop. Accordingly, produced drop size was evaluated. Simultaneously Reitz in 1987 [12] came up with WAVE model, which describes the atomization processes as the breaking of parcels into drops. He assumed that liquid is sprayed out in the form of discrete parcels of

drops like cylindrical blobs. The Surface instability on those blobs was introduced by linearized hydrodynamic equations that give the dispersion relations. From this analysis, the breakup length and time scales were derived for the blobs, that were necessary to generate smaller droplets. The drop size of the newly formed was assumed to be proportional to the calculated wavelength, under the premise that the wavelength is smaller than the parent drop circumference. To improve the prediction of the breakup process, e.g., shorten liquid penetration lengths observed in a combustion diesel engine, Patterson and Reitz in1998 [13] suggested accelerated breakup modeling. To introduce more fast-growing instability, the previous WAVE breakup model was complemented with Kelvin-Helmholtz instability and Rayleigh-Taylor instability.

Liquid Jet Breakup Model

The simulation for primary breakup modeling was deployed in such a way that it makes the breakup event delayed until the liquid core length matches to which experimentally observed data, and then the breaking event is triggered by the TAB model. The fragmented liquid core at the nozzle exit was nozzle-sized large drops, and they are initially unstable. So their lifetime is maneuvered to prolong, and after the primary atomization length, the drops turn to break. They start to split into smaller product drops until they reach a stable condition. Tanner in 2003 [14] presented CAB model, i.e., cascade atomization and drop breakup. He designed it such that product drops are governed by the cascade breakup law, and improved treatment was added to it. For more realistic-looking in simulations, the initial drop size distribution is equipped so that

the fragmented liquid core can reflect the surface stripping effect near the nozzle exit through small drops.

Wave Instability on Liquid Sheet

Sirignano and Mehring in 2000 [15] proposed a linear instability method at the interface between liquid and gas. An inviscid liquid sheet was subjected to two types of disturbance, either a sinuous wave or varicose wave as seen in Fig. 2.1, and compared which would make the liquid sheet more vulnerable. While varying conditions to density and weber number for liquid and gas, it was found that the sinuous wave was higher for maximum growth rate when it is a low-density ratio, the varicose wave, however, tended to increase significantly for that as density ratio increases. In addition to that, a larger weber number always led to a higher maximum growth rate for both waves. Senecal et al. in 1999 [16] compared a viscous liquid sheet with an inviscid one for a growth rate by a sinuous wave disturbance, and they assessed that viscosity affects the maximum growth rate to reduce. Schmidt et al. in 1999 [16,17] sought to apply a swirl spray atomization with CFD breakup models. They used spray angle and mass flow rate to estimate the thickness of the torn-off sheet at which primary break up occurs with its length and time scale, followed by calculations of the primary drops sprouted from the torn sheet ligaments. Then secondary breakup modeling activated the primary drops to split into smaller ones afterward.

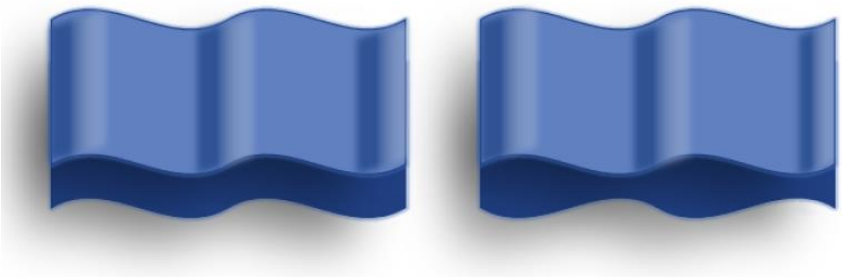

(a) sinuous wave (b) varicose wave or axisymmetric wave

Fig. 2.2 Illustration of surface instability on the liquid sheet

2.3 Research on Spray Atomization in Recent Decades (the 2000s ~)

Direct Numerical Simulation, DNS, solves Navier-Stokes equations directly without introducing any turbulence model so that numerical formulation is simple, the actual implementation is, however, costly because of the high spatial and temporal resolution to be solved. Hence a compromised model such as RANS, i.e., Reynolds Averaged Navier-Stokes Simulation, or LES, i.e., Large Eddy Simulation, has been used in place of DNS for turbulent flow simulations. RANS characterized by time-smoothed averaging is suitable for steady-state, on the other hand, less accurate in unsteady flow. On the contrary, LES characterized by spatial filtering is better suitable for temporally unsteady flow. In spite of it is called a DNS for spray atomization, it does not necessarily mean which resolves down to the droplet scales and its structure, i.e., shape and internal flow, rather it is typically based on the point-particle droplet approximation where the Stokes number is very small for the droplet, so as being assumed a sphere without any internal flow [18]. The method for tracking of phase interfaces such as Volume-of-Fluid, Level-Set, or both combined is considered at the stage of primary atomization to capture

interactions between gas and liquid, and the coupling of Lagrangian point particle with Eulerian interface is then expected to perform a more accurate prediction.

Implementation into CFD

Incompressible Navier-Stokes equations are used to solve the mixture flow field, where liquid and gas phases are dealt with as a single fluid having material properties that change across the interface. It is applied over primary atomization regions or phase interfaces, and other regions such as single phase regions or far fields are handled in a relatively coarse mesh. This method captures the interface dynamics and liquid curvatures, then it combines with the Lagrangian description of droplets where it is unable to fully resolve the small structure dynamics, developed by Herrmann [19–21].

Eulerian-Lagrangian Spray Atomization model, i.e., ELSA model, pioneered by Vallet et al. in 2001 [22] considered mean surface area per unit volume instead of mean droplet diameter in that the liquid parcels are not always spherical. They introduced the defined surface density function with Favre-averaged Navier-Stokes equations and evaluated the model function coefficients by comparing them with the DNS data. Originally intended for the high Reynolds and Weber number in turbulent flows, the transport equation for the mean mixture velocity was written with neglecting the terms of surface tension and laminar viscosity. The quantity of liquid interface or the local surface density was defined in terms of generalized function, and the transport equation for the function was solved by Lebas et al. in 2008 [23].

Alternately, a joint sub-grid probability density function of liquid volume and surface was proposed by LES implementation that simulates regions of dense and dilute.

The modeled PDF was solved by Fokker-Plank equation. This LES-PDF approach with stochastic fields allowed obtaining the instantaneous sub-grid liquid structure distributions [24]. Elsewhere, Eulerian-Lagrangian with a sub-grid modeling approach was considered. One of the simulations applied with this method was the sub-grid breakup model based on the energy balance [25]. The criterion was handled depending on the relationship between the surface tension and the sum of the turbulent kinetic energy as well as the aerodynamic effect at the interface, with the Taylor microscale applied as the critical eddy size, over the coarse grid in an attempt to reduce computational costs. This criterion determined whether to generate and release droplets near the interface, which follows the lagrangian description of point particles. In a similar manner, there were various simulations with different sub-grid modeling. Among them were the turbulent resonant atomization model by Umemura and Shinjo in 2018 [26], the sub-grid scale stress and scalar flux model by Ketterl and Klein in 2018 [27], and the sub-grid scale capillary breakup model by Kim and Moin in 2020 [28].

Experimental Visualization Techniques

Over the past decades, conventional measurement techniques, such as schlieren and shadowgraph, or photography and holography, were used to image the flow of sprays [29]. Recently, Bachalo in 2000 [30] addressed the importance of diagnostic measurements to clearly illustrate spray characteristics that are involved in complex phenomena. He criticized it for lacking completeness and quality in measured information, recognizing its failure and deficiencies in measurement capabilities. Furthermore, there has been a growing need of identifying internal features of the

optically highly dense regions in sprays, especially near the nozzle exit where it is not visible to the naked eye. So the insertion of a physical probe into the spray was an alternative way, but that can deform the original flow field. Among a number of different imaging techniques to deal with the issue, Linne in 2013 [31] reviewed the three methods; transillumination, internal illumination, and planar imaging. X-ray phase contrast imaging [32] and ballistic imaging [33], optical connectivity called OC [34], and structured laser illumination planar imaging called SLIPI [35] are those using the aforementioned techniques respectively.

The optically dense region is believed where primary atomization initiates. Since the primary breakup mechanism serves as the initial source of droplets with a specific size distribution, location, and momentum vectors, therefore, it subsequently affects the development of secondary breakup. In this regard, proper experimental observation with convincing analysis for this region is imperative to understand spray dynamics and evolution well. On the other hand, CFD models resort to the initial conditions for primary drops by making reasonable arguments, e.g., drop generation, and tune it to match with the downstream measurements, leaving the prediction capability downgraded.

2.4 Modeling of Drop Size Distribution

As having numerous drops with various ranges in size after the breakup process, the need for the expression to characterize drop size exists, so that it can be used as a parameter in the function to describe the dynamics of spray atomization. The representative drop diameter was standardized by Mugele and Evans in 1951 [36]. The commonly used in spray parametric analyses is Sauter Mean Diameter, i.e., SMD or D_{32},

which is applicable in the efficiency or mass transfer study. Other mean diameters else of SMD were designated based on the arithmetic mean or the volume mean, and so on.

Babinsky and Sojka in 2002 [37] reviewed the three available methods for modeling drop size distributions, which include the use of empirical way, discrete probability function, and lastly maximum entropy principle. For the empirical method, it was diagnosed with the incapability of fitting a wide range of actual drop size distributions. For the maximum entropy method, it pointed out that two representative diameters are needed at least for constructing the distributions although only one of two is currently possible to obtain by an instability analysis, hence, the correct prediction is incomplete. For the discrete probability function, DPF method, the fluctuating initial conditions were used as the input probability density function, input PDF, to the monodisperse spray model so that it can produce a non-deterministic distribution. It outlined some of the drawbacks such that being limited to primary atomization and difficulty in obtaining comparative experimental measurements of the quantities of interest. On the other hand, it would be a promising method in that it is usable for fluids with complex rheology or different atomization modes. Besides, advances in CFD could compensate for the existing drawbacks of the lack of necessary inputs.

Paloposki in 1994 [38] carried out a comparative study among different empirical distribution functions which include upper-limit, log-normal, Nukiyama-Tanasawa, Rosin-Rammler, log-hyperbolic, and three-parameter log-hyperbolic form. In his study, the chi-square statistical test showed Nukiyama-Tanasawa and log-hyperbolic are better fit to the experimental data, implying that mathematically rather complex and having

more unknown fitting coefficients for the distribution functions result in a more favorable fit.

Dumouchel in 2009 [39] reviewed several models based on the maximum entropy formalism proposed by different scholars. According to his paper, the first attempt using this method was by Sellens and Brzustowski in 1986 [40]. They conceived a liquid sheet breakup process in a way of statistical inference for a physical system that may be described by certain average quantities which are known. Those physical constraints were expressed mathematically and sought for the solution by maximizing the Shannon entropy distribution. The maximization problem was solved using Lagrange multipliers that give an expression for the probability distribution. The set of constraints they used in the formalism included conservation of mass, momentum, kinetic energy, and surface tension energy, in addition to the normalization condition from the definition of probability. They derived the number-based PDF over nondimensional drop size distribution, appearing similar in form to the Rosin-Rammler's type. Parallel to this work, Li and Tankin in 1987 [41] developed their own approach independently. They used volume-based PDF, and the resulting distribution form was similar to the Nukiyama-Tanasawa type.

Sivathanu and Gore in 1993 [42] prescribed DPF method in the study for the radiative transfer equation in fluctuating turbulent media to avoid solving the partial differential equations which were traditionally demanded in obtaining PDF intensity. Subsequently, the DPF method was applied in the field of drop distribution study by Sovani et al. in 1999 [43], and they demonstrated the fluctuation effect of relative velocity in gas-liquid at the nozzle exit, which lead to making changes in the width of the

drop size distribution as increases corresponding to the level of the fluctuations. Williams in 1958 [44] described a droplet distribution evolution through the statistical formalism in the transport equation that consists of the effect of droplet growth, the formation of new droplets, collisions, and aerodynamic forces. The transport equation was utilized for the phenomenological effects in the spray simulation like dense evaporating coalescent region [45].

CHAPTER 3

MATHEMATICAL FORMULATION

3.1 Equations of Conservation: Liquid Jet in a Quiescent Ambient

The formulated equations we use here are based on fundamental physics laws along with the integral approach, which has been studied in those papers by Lee [46–52]. Some of the key equations are reviewed with added explanations as follows.

Conservation of Mass

$$\rho_L u_{inj} A_{inj} = \int_{u=0}^{u_{max}} \int_{D=0}^{D_{max}} nP(D,u) \frac{\pi D^3}{6} \rho_L u A \, \mathrm{d}D \, \mathrm{d}u \approx \frac{\pi}{6} n \rho_L u_L A \sum_{i}^{N} P(D_i) D_i^3 \, \Delta D_i \quad \text{Eq. (3.1)}$$

Eq. (3.1) describes that the injected liquid mass flow rate is equated to the generated droplet mass flow rate with the representative droplet velocity, u_L, within a control volume in a steady state. The number of droplets flowing per unit time, nuA, is seen as the number flow rate. In addition, a spherical drop with a volume of $\pi D^3/6$ is postulated. The control volume is set from the plane of injection to that of primary breakup ends. As it undergoes severely disordered breakup events within the control volume, a wide range of drop sizes and velocities results, obviously implying that is unpredictable in a deterministic manner. Hence it brings to the need for probability distribution to utilize it in a mathematical formulation. The simpler expression is derived with an approximation in which a representative drop velocity, u_L, substitutes velocity

random distribution, thus reducing the expression to a single random variable *D* and its distribution $P(D)$ that are only accountable. On top of that, the discrete probability distribution $P(D_i)$, instead of the continuous probability distribution $P(D)$ as probability density function, is adapted. And the *N* number of categorical divisions for the discretization is used. The $P(D_i)$ signifies a normalized probability, meaning each probability is divided by an interval ΔD_i. Finally, the summation with finite ΔD_i is in place of the integral notation.

Conservation of Energy

$$\rho_L \frac{u_{inj}^3}{2} A_{inj} = \frac{\pi}{12} n \rho_L u_L^3 A \sum_i^N P(D_i) D_i^3 \, \Delta D_i + n u_L A \pi \sigma \sum_i^N P(D_i) D_i^2 \, \Delta D_i + \mu_L \left\langle \left(\frac{\partial u}{\partial y} \right)^2 \right\rangle (Spray\ Volume) \quad \text{Eq. (3.2)}$$

Eq. (3.2) describes how the kinetic energy from injection contributes to the formation of droplets. On the left-hand side, LHS, expresses the rate of liquid kinetic energy entering into the control volume. On the right-hand side, RHS, the first term denotes the rate of the droplet's kinetic energy. These two terms are analogous to that of the conservation of mass in such a way that, it substitutes ρ_L in Eq. (3.1) with $\rho_L u_{inj}^2/2$. The second term on the LHS is for the rate of the surface tension energy, and the third term is for the dissipation. The dissipation term is then approximated as shown in Eq. (3.3). The notation of $< \cdot >$ indicates averaging operator. K is a constant with the dimension of volume [L^3] related to the spray volume. The K is not a priori known so it demands to be calibrated in trial and error, whose value is in turn divided by injection

volume flow rate to get K' with the dimension of time [T] for being the simpler formulation as seen later in Eq. (3.7). Here K' could be thought of as the quantity associated with relaxation time. D_{32} in Eq. (3.5) is a characteristic drop diameter which is equivalent to the definition of Sauter Mean Diameter [36].

$$\mu_L \left\langle \left(\frac{\partial u}{\partial y}\right)^2 \right\rangle (Spray\ Volume) \sim \mu_L \left(\frac{u_L}{D_{32}}\right)^2 (Spray\ Volume)$$
$$= K\mu_L \left(\frac{u_L}{D_{32}}\right)^2 = K' u_{inj} A_{inj} \mu_L \left(\frac{u_L}{D_{32}}\right)^2 \quad \text{Eq. (3.3)}$$

where

$$K' = \frac{K}{u_{inj} A_{inj}} \qquad K' \sim [T] \quad K \sim [L^3] \quad \text{Eq. (3.4)}$$

$$D_{32} = \frac{\sum_i^N P(D_i) D_i^3 \, \Delta D_i}{\sum_i^N P(D_i) D_i^2 \, \Delta D_i} \quad \text{Eq. (3.5)}$$

The number density, n, is derived as Eq. (3.6) from the conservation of mass Eq. (3.1), before it is plugged into the energy equation Eq. (3.2). The final result through all these accounts is the quadratic equation for D_{32} shown in Eq. (3.7). The solution of Eq. (3.7) renders the analytic expression in terms of D_{32} presented in Eq. (3.8).

$$n = \frac{\rho_L u_{inj} A_{inj}}{\frac{\pi}{6} \rho_L u_L A \sum_i^N P(D_i) D_i^3 \, \Delta D_i} \qquad \left[\frac{1}{m^3}\right] \quad \text{Eq. (3.6)}$$

$$\left(\rho_L \frac{u_{inj}^2 - {u_L}^2}{2}\right) D_{32}^2 - 6\sigma D_{32} - K'\mu {u_L}^2 = 0 \qquad \text{Eq. (3.7)}$$

In most cases, the parameters of σ, K', μ, u_L tend to have a much small order of magnitude, i.e., 1~10^{-3}, when compared to that of (a) in Eq. (3.8). The denominator (a) quantifies the total consumed-momentum through atomization process until it reaches steady-state. Therefore it is deducible from Eq. (3.8) that, the representative drop size D_{32} is largely attributed to the consumed-momentum (a). In other words, D_{32} is inversely related to the consumed-momentum because the denominator predominates over the nominator.

D_{32} Quadratic Formula

$$D_{32} = \frac{3\sigma + \sqrt{9\sigma^2 + K'\mu {u_L}^2 \rho_L \frac{u_{inj}^2 - {u_L}^2}{2}}}{\rho_L \frac{u_{inj}^2 - {u_L}^2}{2}} \quad \text{or equivalently,}$$

$$D_{32} = \frac{3\sigma + \sqrt{9\sigma^2 + K'\mu {u_L}^2 (a)}}{(a)} \quad \text{where} \quad (a) = \rho_L \frac{u_{inj}^2 - {u_L}^2}{2} \qquad \text{Eq. (3.8)}$$

In addition, this view is also supported by the fact that in a number of spray experiments on the liquid jet in a quiescent ambient, the tendency has been typically observable in which higher injection velocity yields generating more small droplets. And this is in accordance with our derived quadratic formula, indicating that Eq. (3.8) favorably reflects physical phenomena. On the other hand, it is presumable that with

having tenuous injection velocity, according to Eq. (3.8) in this case, the surface tension term now becomes comparable to that of (a). Accordingly, this phenomenon also has been observed in several experiment with low-velocity injection in the past, as reported in terms of a capillary-driven jet. To sum up, our derived D_{32} quadratic formula characterizes the mechanism of primary atomization, and it determines the representative drop size that is consistent with the physically observed outcome.

3.2 Equations of Conservation: Liquid Jet with Added Gas Momentum

In this section, we consider the incoming gas momentum in addition to the liquid injection. Essentially, this type is involved in gas-driven spray atomization. Eq. (3.9) delineates the conservation of energy, and it is justified by supplementing two terms into Eq. (3.2). One is the incoming gas kinetic energy term on the LHS, and the other is the outgoing gas kinetic energy term on the RHS. To be specific, the new term of $\rho_g u_{in}^3 A_{in}/2$ refers to the former, and the other new term of $\rho_g u_{out}^3 A_{out}/2$ refers to the latter. The area from incoming or outgoing of gas is denoted by either A_{in} or A_{out}, and they are not necessarily to be identical with that of liquid denoted by A. For instance, the cross-flow type of spray may have different area for each of liquid and gas, whereas the co-flow type of spray has the same outgoing area. Therefore, it depends on the type of spray subjected and the control volume geometry.

To derive the expression on D_{32}, the Eq. (3.9) is dealt with in a similar way to what we have done for the liquid jet in a quiescent ambient in the previous section. Accordingly, the resulting quadratic equation for D_{32} is expressed as Eq. (3.10). Subsequently, the positive root of the quadratic equation is presented as in Eq. (3.11).

Conservation of Energy, for the Gas-Driven Spray Atomization

$$\rho_L \frac{u_{inj}^3}{2} A_{inj} + \rho_g \frac{u_{in}^3}{2} A_{in} = \frac{\pi}{12} n \rho_L u_L^3 A \sum_i^N P(D_i) D_i^3 \Delta D_i + n u_L A \pi \sigma \sum_i^N P(D_i) D_i^2 \Delta D_i + \mu_L \left\langle \left(\frac{\partial u}{\partial y}\right)^2 \right\rangle (Spray\ Volume) + \rho_g \frac{u_{out}^3}{2} A_{out} \quad \text{Eq. (3.9)}$$

$$\left(\rho_L \frac{u_{inj}^2 - {u_L}^2}{2} + \rho_g \frac{u_{in}^2 - {u_{out}}^2 \left(\frac{A_{out}}{A_{in}}\right)}{2} \left(\frac{u_{in} A_{in}}{u_{inj} A_{inj}}\right) \right) D_{32}^2 - 6\sigma D_{32} - K' \mu \left(u_{in} - u_{inj}\right)^2 = 0 \quad \text{Eq. (3.10)}$$

D_{32} Quadratic Formula, for the Gas-Driven Spray Atomization

$$D_{32} = \frac{3\sigma + \sqrt{9\sigma^2 + K' \mu \left(u_{in} - u_{inj}\right)^2 (b)}}{(b)} \quad \text{Eq. (3.11)}$$

where $(b) = \rho_L \frac{u_{inj}^2 - {u_L}^2}{2} + \rho_g \frac{u_{in}^2 - {u_{out}}^2 \left(\frac{A_{out}}{A_{in}}\right)}{2} \left(\frac{u_{in} A_{in}}{u_{inj} A_{inj}}\right)$

Note that only one of the quadratic solutions to Eq. (3.10) is regarded as valid, which is positive D_{32} as in Eq. (3.11) since we deem negative D_{32} an unphysical outcome. In conclusion, the derived D_{32} quadratic formula in gas-driven spray atomization shows the analogous mechanism to that of the liquid jet in a quiescent ambient except for the influence coming from gas kinetic energy.

3.3 Validations and Considerations on the D_{32} Quadratic Formulation

The above formulations have been shown to work quite well across a range of spray configurations; pressure-atomized [46], swirl [49], cross-flow [50], and air-blast [51]. Basically, this approach involves minimal empiricism, and it is not invoked by any unphysical assumptions but rather preferred to draw from the conservation equations of mass and energy. The usefulness of the formulations is in the following ways.

First, it captures and delineates the physics of the atomization process without delving into the complex dynamics in detail for every intermediate state. Indeed, the conservation principles can be applied between the initial and final atomization state. To be specific, the conservation of energy in Eq. (3.2) and Eq. (3.9) shows that the reduction in the kinetic energy due to the aerodynamic interactions between the liquid and gas phase appears in the surface tension energy term while also being affected by the viscous dissipation. This energy transfer balance leads to the explicit expression for the drop size as in Eq. (3.8) and Eq. (3.11). If a large portion of either the liquid- or gas-phase kinetic energy is lost, then this energy is transferred to and makes the portion of surface tension energy increased, which is associated with generating small droplets. Note that a liquid would create more surface area in total by reforming one's shape to being many small droplets for the same given volume, which status demands an additional amount of surface tension energy. This is because the molecules positioned along the surface consume more potential energy. Conversely, with substantial viscous dissipation, the energy partitioning toward the surface tension energy is reduced so making drop size increased.

Secondly, it enables us to investigate the relationship between drop size and its velocity by Eq. (3.8) and Eq. (3.11). For the liquid jet in a quiescent ambient, the result is found in Fig. 3.1. Fig. 3.1 illustrates the dynamic relation for drop size with velocity in comparison with the laboratory data by Bellerova et al. in 2019 [53]. The data are from the laboratory experiment that was conducted with a ¼ inch spray nozzle with water pressurized up to 3 bar before issuing into a quiescent atmosphere. The water injection velocity from the nozzle is approximated as 24 m/s. In total 3858 droplets were analyzed and plotted as the scattergram. Each point on the scattergram of Fig. 3.1 represents a single data on drop size with its velocity. A theoretical line using Eq. (3.8) is also drawn for the comparison. Thereby, this drop size-velocity relation is verified as favorably following alongside a scattergram in the measured drop size D and its velocity u_p.

The "scatter" in the simultaneously measured drop size-velocity pairs is typical in both phase-Doppler and imaging diagnostics due to fluctuations coming from various factors, e.g., different local viscous dissipation or measurement uncertainties. The theoretic curve by Eq. (3.8) is seen as like representing an average line from the scattering data set. Therefore, our theoretical relationship has been demonstrated as reflecting well the result from the experimental data, through the expression of the drop size, D_{32}, versus its velocity, u_L, in the D_{32} quadratic formula Eq. (3.8) for the liquid jet in a quiescent ambient gas.

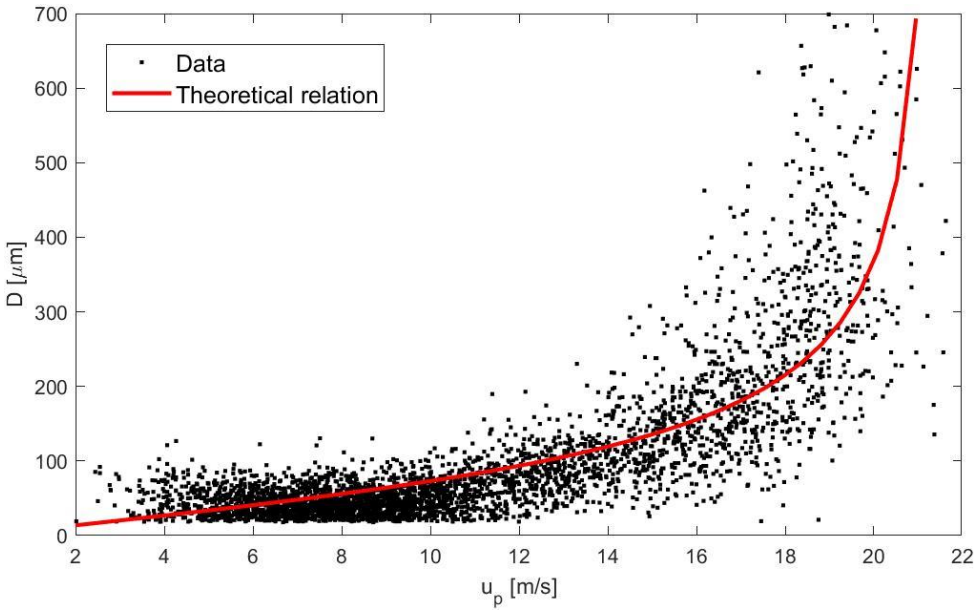

Fig. 3.1 Dynamic relation between the drop size and its velocity, for the liquid jet in a quiescent ambient gas. u_{inj} = 24 m/s. Theoretical relation as line by Eq. (3.8), data as symbol by Bellerova et al. [53]

In Fig. 3.2 the dynamic relationship for the liquid jet with added gas momentum is shown. The theoretical relation is drawn by the D_{32} quadratic formula of Eq. (3.11), whose expression of drop size D_{32}, versus its velocity u_{out}, is compared to the experimental data from the air-mist spray. This experiment was implemented by a ⅜ inch spray nozzle, by which liquid is pre-mixed with pressurized air before it is discharged as mist. The pressurized air was up to 1.5 bar. The airflow rate for a nozzle was 30,832 ℓ/h, and the injected water pressure was 1.98 bar. This approximates the injection velocity of 20m/s for water, and 120m/s for air from the air-mist nozzle.

(a)

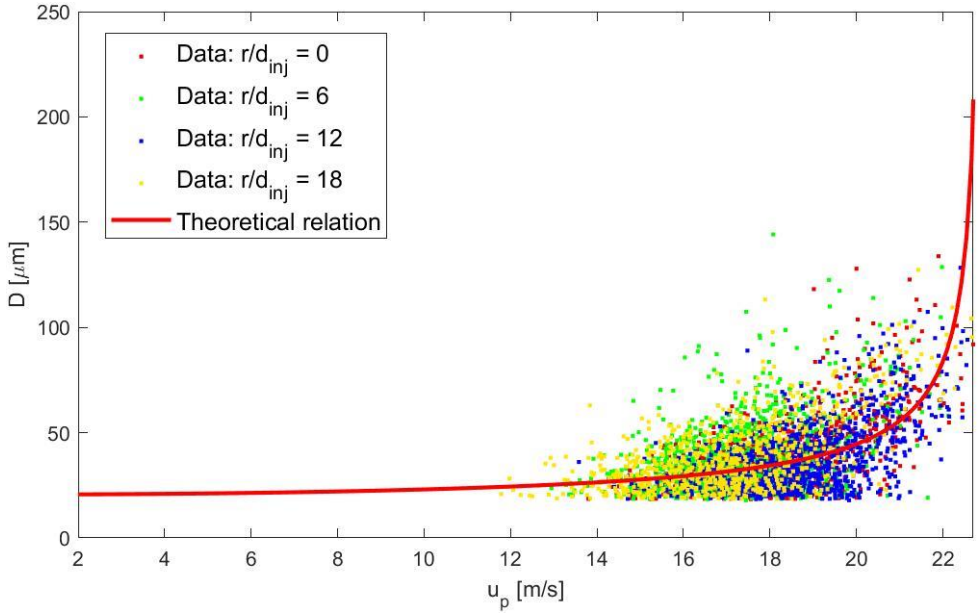

(b)

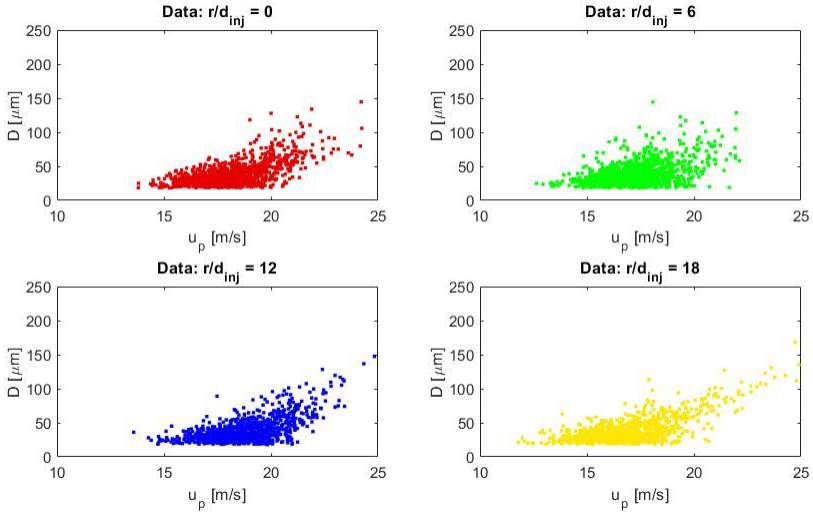

Fig. 3.2 Dynamic relation between the drop size and its velocity, for the liquid jet with added gas momentum. u_{inj} = 20 m/s, and u_{in} = 120 m/s. (a) Theoretical relation as line by Eq. (3.11), data as symbol by Bellerova et al. [53]; (b) sampling data at different radial distance r/d_{inj} in the separate plot prior to combining

Owing to the nature of mist-type spray that is vulnerable to convective velocities, the collected droplet data are broadly scattered as seen in Fig. 3.2(a), having an elusive tendency in appearance at the first glance. A necessity for treatment in the raw data arose

to see a more distinct tendency between drop size and its velocity, hence it is ordered in such a way; the separate data observed by a different position takes the post-processing, in which the median drop size with its velocity is sampled for every 30 droplets after the raw data are sorted in ascending order for the drop size. This treatment would reduce aberrant data by sifting out the outliers, while it draws an average estimate since frequent one is more likely to be sampled repetitively. The axial distance from the nozzle to the measurement region is 250mm, and the radial distance from the nozzle axis varies up to 180mm. The number of measured droplets is 35043, 33858, 28283, and 23136 for 0, 60, 120, and 180mm, respectively. The number of sampling data to plot after post-processing is 4013.

There are some distinguishable features in Fig. 3.2(a) when it is compared to Fig. 3.1. The scattergram from the gas-driven spray atomization is found to be distributed within more confined ranges as seen in Fig. 3.2(a) than that of Fig. 3.1. The data are so scattered and hard to find a curve-like trend, but rather descriptively triangle-like as seen in Fig. 3.2(b). And they are mostly in small drop sizes. This can be interpreted such that additional energy attributed to gas momentum makes surface tension energy increase to some extent, so correspondingly resulting in more shattered droplets with smaller sizes. To be specific, Fig. 3.2 (a) appears the drop size distribution mainly under 100μm whereas Fig. 3.1 reaches mainly up to 400μm. Even if we point out the different liquid injection velocities, i.e., 20m/s and 24m/s, this gap could not be regarded considerably to cause such a substantial drop size difference.

On the other hand, the resulting drop velocity distributions are significantly different. Fig. 3.2 starts from 12m/s and spreads up to 25m/s with an injection velocity of

20m/s, whereas Fig. 3.1 stretches down to 2m/s and reaches up to 22m/s with an injection velocity of 24m/s. Therefore, it is reasonable to infer that gas-driven spray is susceptible to the convective velocity induced by gas momentum, from the fact that the upper limit of droplet velocities exceeds the liquid injection velocity. It is also corroborated by the triangle-shaped scattering in that the smaller droplets are more subjected to the convective velocity, thus making the distribution spread along the abscissa to the right for the relatively small droplets. For example, in Fig. 3.1 that without having convective velocity, dense scattering is found for small drop sizes with relatively low velocity. And if this dense scattering is driven by the presence of convective velocity, some of them would be measured at high velocity too, so making slanted-triangle-distribution like Fig. 3.2(b). Fig. 3.3 is shown for the schematic experimental setup.

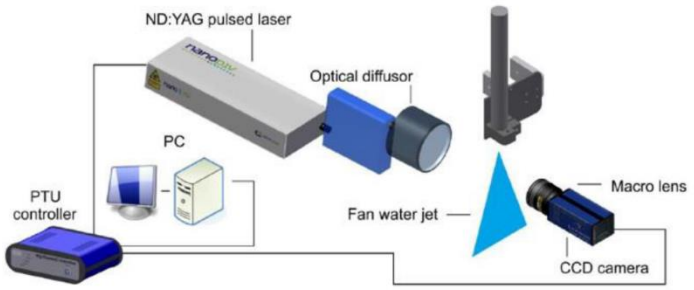

Fig. 3.3 Schematic of the experimental setup, courtesy of Bellerova et al. [53]

In both Fig. 3.1 and Fig. 3.2, there are scatter in the data while the theoretical result is plotted as a line. The reason for the scatter in the data is mainly due to the fact that these sprays are turbulent so a range of liquid velocities may exist with turbulent fluctuations. For the theory, the average liquid velocity is input, which explains why the

theoretical result is plotted as a line. If we use a velocity distribution, like a probability density function instead of the average input, then a range of drop size would be obtained, frequently matching the scatter in measured D_{32}. And the generation of drop size distribution from velocity distribution is demonstrated in chapter 4.

Lastly, Eq. (3.8) and Eq. (3.11) can be used as the primary atomization module in computational simulations of spray flows. Existing methods for continuous liquid flow, such as Volume-of-Fluid or Level-Set, work quite well prior to the small-scale droplet formation in which spatial and temporal resolutions are high. Also, once drops are formed and their initial size and velocity are known, then Eulerian-Lagrangian tracking algorithms are quite functional in computing the droplet trajectories under most spray conditions. In dense sprays, the Lagrangian tracking can be augmented with drop collision and coalescence models. Therefore, the current formulation can effectively link the two computational modules to complete a computational protocol for spray flow simulations [54,55].

Comparison with Other Existing Model or Correlation for D_{32}

In Fig. 3.4, the KH instability model [56] of primary atomization for the prediction of drop size has been compared with the results of calculation using our D_{32} equation, in pressure-atomized swirl sprays. Additionally, a correlation suggested for the spray modeling [57] is also compared in the figure. The comparison among the three curves is made while using the common parameters as in the calculation for the correlation, which are found in the reference paper [57]. Besides, we add experimental data of global mean drop size spectra from varying the atomizer geometry and injection

properties [58]. The agreement with the experimental data varies depending on Weber number ranges. For the model, however, there are tuning parameters at various places, so that any reasonable set of data can be reproduced. As noted in the introduction, and since experimental observations clearly indicate that the fluid physics of the primary atomization do not follow the phenomenology embedded in such models of KH-RT hybrid model or TAB model, these models should be considered as engineering estimations of the drop size.

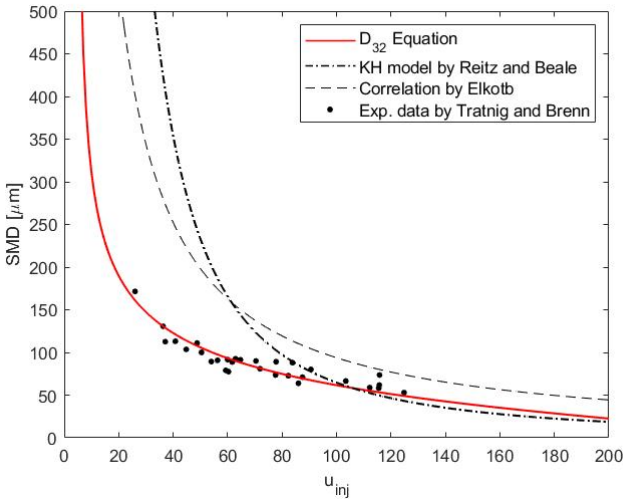

Fig. 3.4 A comparison of the drop size calculated from other existing spray atomization model [56] or correlation [57], with the same diesel injection parameters. Experimental data [58] is global drop size spectra, with various pressure-swirl atomizers and parameters

CHAPTER 4

MOMENTUM ANALYSES

4.1 The Use of Momentum Analyses

From the momentum analysis between liquid and gas, a formulation is constructed to determine the conversion between liquid and gas velocities during spray atomization [52]. With the aid of this formulation for momentum exchanges between them, our description of the relation between drop size and velocity is reinforced. Since our D_{32} quadratic equation is prescribed based on the conservation equations for mass and energy, adding the momentum analyses to it serves to deliberate our considerations in diagnosing the spray atomization process. Therefore, the effort to advance in presenting the correlated relation between drop size and velocity makes it possible, putting our interpretation on a sound basis.

In this approach, the aerodynamic drag is approximately parameterized by the drag coefficient and relative velocities with dimensional scaling. This allows us to calculate the spray drop size and its distributions from the injection parameters. The formulation also gives a dynamic perspective in spray atomization, in which the liquid momentum undergoes deceleration due to drag, and the drop size is the result of attendant energy transfer from the liquid kinetic to the surface tension energy; the reduced kinetic energy appears in terms of the increased surface tension energy for the resultant drops, so getting slow with small sizes after all. Therefore, the consideration of momentum change adds a key component to the analysis of spray atomization leading to some useful relationships between the drop size and velocities. In this work, the results in the use of momentum analyses are presented for the determination of drop size and distributions,

that are found in various spray injection geometries. By means of it, the momentum effects on the drop size and its distributions during spray atomization are well described.

4.2 Formulation of Momentum Equations

The relations of momentum conservation for the liquid- and gas-phase are written as in the following. Here, pressure and surface force leading to the drag are summarized into the drag coefficient, C_D. And since we focus on the momentum-driven sprays, the gravitational effect is neglected.

Case 1: Liquid Injection into an Initially Quiescent Gas Surrounding

Liquid
$$u_L \frac{du_L}{dx} = -\frac{C_D}{2}\frac{\rho_g}{\rho_L}\frac{A_D}{V_s}\left(u_L - u_g\right)^2 \qquad \text{Eq. (4.1)}$$

Gas
$$\rho_g u_g^2 A_p = \frac{C_D}{2}\rho_g A_D \left(u_L - u_g\right)^2 \qquad \text{Eq. (4.2)}$$

In the liquid momentum equation of Case 1, the acceleration term du_L/dt was converted to the spatial derivative form using $dx/dt = u_L$, and the resulting is seen on the LHS. Then, the deceleration of the liquid is due to the drag force on the RHS, as represented by the drag coefficient C_D, which would depend on the shape of the liquid column or sheet. It is found that even in the full atomization regime, the liquid core is observed with producing droplets in the periphery. For this reason, the drag coefficient, spray area, and volume are used along with the liquid momentum equation. The gas momentum equation from Eq. (4.2) is used in conjunction to determine u_g and u_L in Eq.

(4.1). Spatial evolution of u_L and u_g can be tracked by concurrently integrating Eq. (4.1) and Eq. (4.2) in the *x*-direction.

The formulations provide a dynamical perspective in spray atomization such that, once the liquid is injected, it suffers from drag which has the liquid decelerated by momentum exchanges with the surrounding gas. Subsequently, this reduction in momentum leads to an attendant decrease in the liquid kinetic energy. Since the energy conservation is obeyed, it is reasonable to assume that the decreased kinetic energy must appear in the alternate form such as the surface tension energy and viscous dissipation. Essentially, those perspectives are already reflected in the energy balance formulations as introduced in the previous contexts. The mass conservation furnishes us with the droplet number density *n*. Within this analytical framework, it brings up the four equations to solve the four unknowns; D_{32}, u_L, u_g, and *n*.

Next, we introduce the momentum balance for the gas-driven atomization processes in two cases of different incoming gas configurations; co-flowing of Case 2, and cross-flowing of Case 3. They are derived in Eq.(4.3) and Eq. (4.4) for the former, Eq. (4.5) and Eq. (4.6) for the latter case. For simplicity, a locally representative mean value $u_{L,x}$ is used for the entire liquid column or sheet. The *x*-direction represents the gas phase streamwise direction, and it is parallel to the liquid jet in co-flowing of gas or perpendicular to the liquid jet in cross-flowing of gas. For these gas-driven spray atomization cases, their momentum equations are written in a similar manner to the previous one, as follows.

Case 2: Liquid Injection with Added Gas Momentum of Co-Flowing of Gas

Liquid $$\rho_L u_{inj} A_{inj}\left(u_{L,x} - u_{inj}\right) = \frac{C_D}{2}\rho_g A_D\left(u_{in} - u_{L,x}\right)^2 \quad \text{Eq.(4.3)}$$

Gas $$\rho_g u_{in}^2 A_{in} = \rho_g u_{in} A_{in} u_{out} + \frac{C_D}{2}\rho_g A_D\left(u_{in} - u_{L,x}\right)^2 \quad \text{Eq. (4.4)}$$

The gas transmits its momentum to the liquid. Therefore the gas loses one's kinetic energy, which goes into the surface tension energy making the liquid droplets. In this regard, it indicates that the amount of momentum change between the two phases has correlated with one another, and that would be responsible for the estimation of the drop size and its distribution too. Indeed, the D_{32} quadratic formula for the gas-driven type of spray of Eq. (3.11) explicitly requires the expression of gas velocity ratio, u_{out} / u_{in}, along with u_L / u_{inj}.

Case 3: Liquid Injection with Added Gas Momentum of Cross-Flowing of Gas

Liquid $$\rho_L u_{inj} A_{inj} u_{L,x} = \frac{C_D}{2}\rho_g A_D\left(u_{in} - u_{L,x}\right)^2 \quad \text{Eq. (4.5)}$$

Gas $$\rho_g u_{in}^2 A_{in} = \rho_g u_{in} A_{in} u_{out} + \rho_L u_{inj} A_{inj} u_{L,x} \quad \text{Eq. (4.6)}$$

For liquid jet in cross-flowing gas, the configuration in which the initial *x* component of liquid momentum is zero, i.e., u_{inj} = 0, makes the momentum balance relations more simple form as seen in Eq. (4.5) and Eq. (4.6). On top of that, the gas

velocity ratio u_{out}/u_{in} is calculated from Eq. (4.6), and the arranged form are shown in Eq. (4.7). It includes the momentum ratio q, as defined in Eq. (4.8).

$$\frac{u_{out}}{u_{in}} = 1 - q\frac{A_{inj}}{A_{in}}\frac{u_{L,x}}{u_{inj}} \quad \text{Eq. (4.7)}$$

where momentum ratio,

$$q = \frac{\rho_L u_{inj}^2}{\rho_g u_{in}^2} \quad \text{Eq. (4.8)}$$

Taking all the delineated momentum balances, the following useful analyses with validations are shown to be possible, giving insights into the dynamic relations for spray atomization. More details on the derivation of the momentum equations are guided to APPENDIX A.

4.3 Validations on Momentum Equations

It begins with a simple case of pressurized-straight spray by spatially integrating Eq. (4.1) and Eq. (4.2); for the detailed spatial integration scheme, it would be referred to APPENDIX A. The resulting liquid- and gas-phase velocities are plotted by solid and dash lines respectively in Fig. 4.1. In addition to that, the plots with various density ratios of ρ_g/ρ_L are included alongside in pairs, to investigate the role of the density effect; for the case of Fig. 4.1, the liquid density is fixed as water while the gas density is varied with having an ambient gas be the reference one, ρ_o. The top curves are the u_L/u_{inj}, which show a continuous decrease due to aerodynamic drag. Meanwhile, the bottom curves are

u_g/u_{inj}, which show a growing momentum on the contrary. Gas density leads to higher drag, thus more deceleration in the liquid velocity at larger gas densities. A simple drag coefficient for cylindrical surfaces may be used as the baseline, and any large surface disturbances residing with increased drag should be accounted for by modifying the drag coefficient. Alternatively, it can turn to computational simulations for the determination of the momentum field; Lee et al., 2021, [54]. The gas velocities are initially zero and change to increase at a higher rate with larger density ratios. Consequently, the density effect is to increase the liquid momentum loss through the drag term as shown in Fig. 4.1.

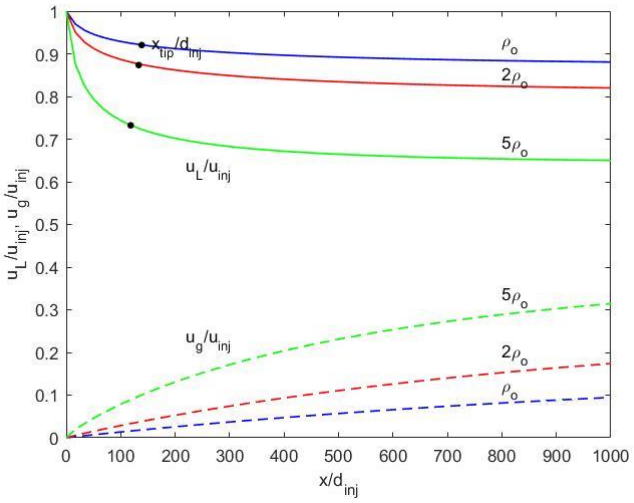

Fig. 4.1 Spatial development of the liquid and gas velocities obtained by integration of Eq. (4.1) and Eq. (4.2). The x_{tip}/d_{inj} are referred to Shimizu et al. [59] as the breakup-length. The reference gas density ρ_o = 1.225 kg/m^3, ρ_L = 1000 kg/m^3, u_{inj} = 120m/s, and d_{inj} = 0.3mm

In addition, from the experimental observations in varying ambient densities from Shimizu et al., 1984 [59], it has been reported that the breakup-length happens to decrease with an increase in ambient density. Therefore, the final result is a combination

of reduced liquid velocity and breakup-length both when the ambient density is increased. This kind of plot serves as an initial estimate for the liquid velocities at primary atomization used in Eq. (3.8) to compute D_{32} by taking the value of u_L/u_{inj} at the position of breakup-length from experimental observations. About the position at breakup-length, the case studied in Fig. 4.1 is $x/d_{inj} \sim 130$ for the reference ambient density condition ρ_0, however, it may vary case by case depending on which experimental configurations are used besides the weber number. In general, the estimation of $x/d_{inj} \sim 100$ can be used for pressurized-straight sprays and it would be shortened for swirl sprays.

For swirl sprays, the same procedures are taken to estimate the u_L/u_{inj} from the integration of Eq. (4.1) and Eq. (4.2), in which C_D is expected to be relatively high with its breakup-length being relatively short due to the swirl spray configurations. Taking a step further, the D_{32} estimation by Eq. (3.8) is applied, and the results are compared with a correlation by Lefebvre [29] as shown in Fig. 4.2 with solid and dash lines respectively. The correlation referenced is, $SMD \sim \sigma^{0.25} \mu_L^{0.25} \rho_L^{0.125} d_o^{0.5} \rho_g^{-0.25} \Delta P_L^{-0.375}$. By arranging it with $\Delta P_L \sim \rho_L u_{inj}^2$, the change of SMD with respect to the liquid injection velocity u_{inj} can be derived; other parameters that are used in this comparison with Fig. 4.2 have been set the same as that of Fig. 4.1.

Fig. 4.2 shows the results of drop size change with respect to the liquid injection velocity, whose reciprocal relation is expected. As studied in the analyses of D_{32} formulations in the previous context, it can be interpreted by the energy equation in which increasing injection velocity contributes to the increase in surface tension energy, hence yielding to the shattering of liquid into even more small droplets. Consequently, an

increase in injection velocity leads to a decrease in average drop size, i.e., D_{32} as the average drop size seen in Fig. 4.2.

On top of that, the gas density effect is examined while increasing it up to 2ρ and 5ρ. And the results are incorporated into the D_{32} estimation as shown in Fig. 4.2, where the effect from density and injection velocity is reasonably reproduced by Eq. (3.8). The corresponding correlation curves by Lefebvre [29] are alongside as well. It shows the decrease in drop size with respect to the higher density. Moreover, it exhibits a rapid decrease with the steep slope by higher density in Fig. 4.2. For the nearly constant atomization length scale, i.e., to yield the same drop size after breakup driven by the same injection velocity, this deceleration effect with increasing density, i.e., by subjecting to higher drag, can be substantial, as in some of the experimental correlations for drop size in swirl sprays from Lefebvre [29]. This is one of the physical mechanisms contributing to smaller drop sizes in swirl sprays where the liquid deceleration is more pronounced than in simple injection geometries.

Speaking of the density effect, in many spray applications like fuel injectors in a combustion engine, high pressure and temperature conditions exist, and there have been numerous experimental studies on the effects of pressure and temperature on drop size. The current analysis takes into account that the pressure and temperature effects are primarily through the density, which affects the aerodynamic drag and therefore kinetic energy content of the liquid phase. Thus, pressure and temperature effects during spray atomization can be summarized into the density effect under the ideal gas equation of state, i.e., $\rho \sim p/T$.

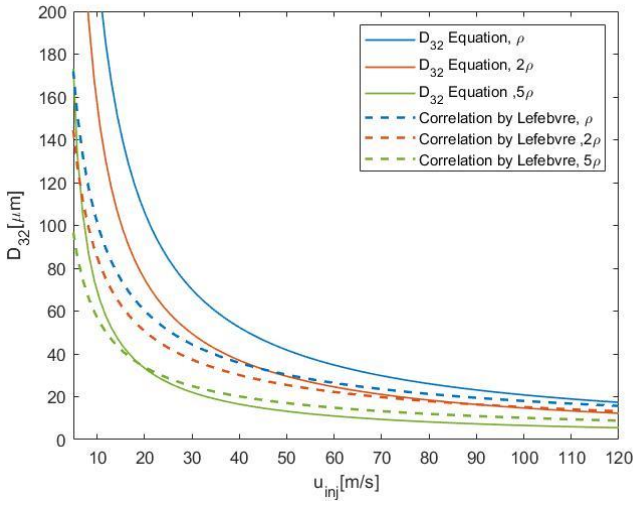

Fig. 4.2 Density effects on the drop size in swirl sprays. The correlations are referred to Lefebvre [29]

The following content is about an application for the momentum analysis for the gas-driven type of atomization in cross-flows. In the shock-induced breakup experiment conducted by Chen et al. [60], they measured the drop size and its velocity as well. The shock induces a rapid gas motion that is characterized by free from gradual changes for the injection condition so that it can provide a step change in convective velocity. This paper finds a correlation between the observed drop size and velocity in non-dimensional form by normalizing with relevant parameters, i.e., $D/D_o = f(u_p/u_o)$. In seeking to compare the correlation by Chen et al. [60] with the D_{32} equation of which momentum relation for cross-flow is incorporated, Eq. (4.7) and Eq. (4.8) in addition to Eq. (3.11) are applied. Since the experiment used elevated pressure, the gas density aft of the shock front is used in those equations.

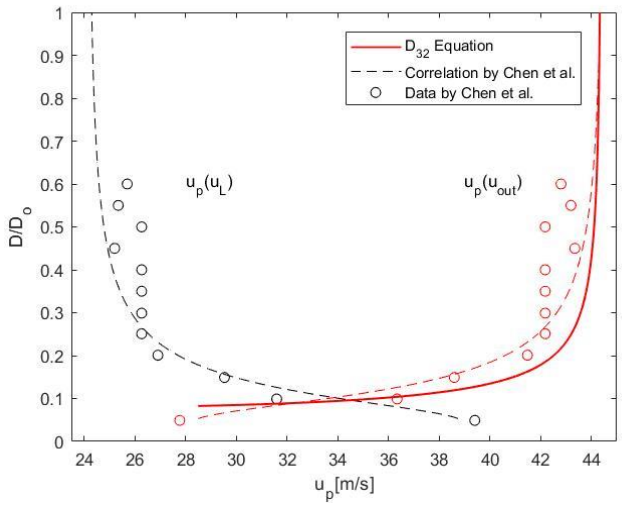

Fig. 4.3 Dynamical relationship between the drop size and its velocity in solid line. The correlation in dash line and experimental data in symbol from Chen et al., 2018 [60]; u_p is converted from u_p (u_L) to u_p (u_{out}), to compare with the D_{32} equation of Eq. (3.11). The u_p is drop velocity and D/D_o is normalized drop size.

Fig. 4.3 is the results of the comparison, showing reasonable agreement. The measured data and its correlation curve are expressed by symbol and dash line in black color both. These in red color are the conversion for those of measured droplet velocities and correlation to being expressed as convective velocities, i.e., u_{out} as the u_p by using Eq. (4.7) and Eq. (4.8). The reason for the conversion has previously explained in the process of analyzing Fig. 3.2, which comes from the dynamical relation for cross-flows in the application of D_{32} equation. As mentioned in the previous chapter that droplets in cross-flows are highly susceptible to the gas momentum so that the resulting droplet velocity u_p can be represented by its convective gas velocity u_{out}; this approach is used in illustrating dynamical relation for the D_{32} equation in cross-flows of gas-driven atomization depicted as Fig. 3.2. Lastly, the red solid line is from the calculation by D_{32} equation of Eq. (3.11) with using the given spray parameters. Eventually, Fig. 4.3 demonstrates that the

converted velocities and correlation from the measured data, which is in red symbol and red dash line, are in accordance with the results of using the D_{32} equation in the red solid line. The experiment used air and water at the velocity of 71m/s and 1.3m/s respectively. The measured diameter for the water column is 0.94mm in the experiment, so it is approximated to d_{inj} in the way of applying the D_{32} equation. Else parameters can be found in the paper [60]. The experimental measurement downstream position is 50mm, and We = 76. The used correlation by Chen et al. [60] is, $u_p/u_o = C_1 - C_2 \exp\{-C_3/(D/D_o)^2\}$ with $C_1 = 0.55$, $C_2 = 0.21$, and $C_3 = 0.011$. The drop velocity is normalized by u_o, which corresponds to the incoming gas velocity, u_{in} in the D_{32} equation. The drop size is normalized by D_o, which corresponds to the water column diameter, approximated to d_{inj} in the D_{32} equation.

4.4 Methods for Drop Size Distributions

The diagnostic techniques in spray experiments enable us to measure both drop size and its velocity. For example, in the use of Phase Doppler Particle Analyzers with Particle Imaging Analyzers, data from these are acquired and then reported as a form of discrete distribution, e.g., histogram. In the followings, the comparisons of distribution are presented, one from the experimentally detected data and the other from the calculation with the D_{32} equation. Accordingly, a suggestion for the way of constructing drop size distribution by using the D_{32} equations is proposed.

Fig. 4.4, Fig. 4.5, and Fig. 4.6 show discrete probability distributions for drop velocity u_p, and drop size D. Note that it is a normalized histogram, in which each probability per bin is divided by the corresponding bin width, and technically it is

different from a continuous distribution function that is commonly denoted by Pdf, although the notation in graphs here uses without distinction.

Fig. 4.4 is for the pressurized-straight liquid jet without the aid of gas momentum. The experimentally collected data are from Bellerova et al. [53], and implemented injection parameters are previously stated in the explanation of Fig. 3.1. The scattering data points of Fig. 3.1 are allocated within the finite number of divisions to make the histogram as seen Fig. 4.4. The y-axis on the right side is for the scale of cumulative distribution function that is denoted by Cdf in the plot, whose appearance is as dash line. Fig. 4.4(a) shows the probability distribution of drop velocity Pdf(u_p), and Fig. 4.4(b) shows that of drop size Pdf(D), both as a histogram. With the aim of comparison to the derived drop size distribution, the mid values at every each bin are chosen as u_L to input Eq. (3.8), which are marked in the red circle as Fig. 4.4(a). Recalling that the D_{32} equation facilitates the calculation for the drop size explicitly from the liquid velocity u_L, the corresponding drop sizes D for the chosen values as u_L are derived in Fig. 4.4(b). In the calculation, the values of each probability are set as the same as those from the drop velocity distribution, i.e., Probability (D) = Probability (u_L). The normalization to construct a discrete probability distribution Pdf(D), for which the derived results by D_{32} equations are used, is carried out. Note that a different normalizing factor exists among the derived values of D, since their allocations are not uniform in contrast to that of the data histogram, i.e., each interval of D as bin size is not uniformly distributed in abscissa. The resulting derived Pdf(D) is in red solid line as Fig. 4.4(b), and it appears in good agreement with the histogram of data.

(a)

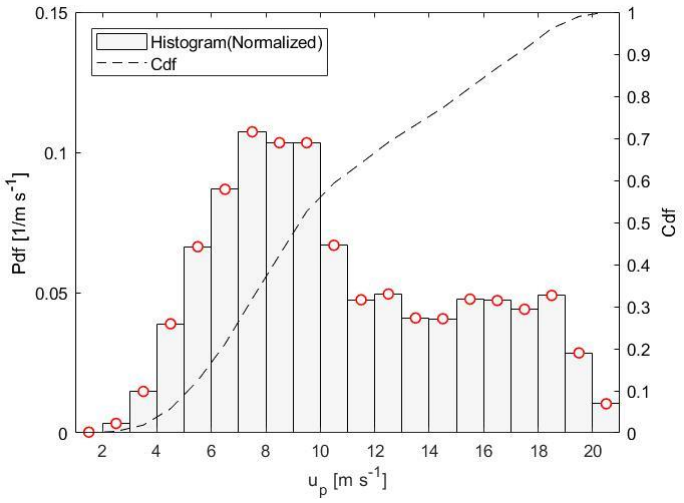

(b)

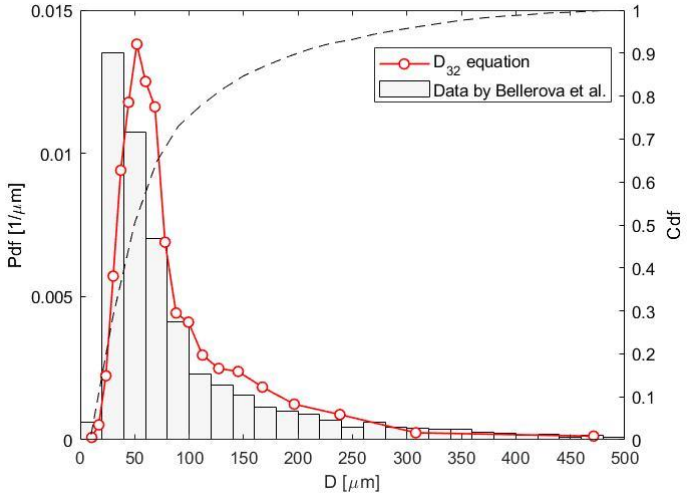

Fig. 4.4 Comparison of discrete probability for the pressurized-straight liquid jet. Experimental data by Bellerova et al. [53]. (a) The number of divisions within the range of 1 to 21m/s is 20 with a bin width of 1m/s for the histogram of drop velocity u_p; (b) The number of divisions within the range of 0 to 500 μm is 25 with a bin width of 20μm for the histogram of drop size D

In a similar manner, Fig. 4.5 is for liquid jets in cross-flows of gas, whose data are aligned with corresponding bins to construct histograms from the scattering points of Fig. 3.2. The same procedure is applied to compare the resulting discrete probability distributions of drop size Pdf(D); The u_L are chosen in Fig. 4.5(a) to derive their drop

sizes from D_{32} equation of Eq. (3.11), then match their discrete probability of D with that of u_L, followed by normalization each by the discrete ranges before constructing the derived distribution as seen in Fig. 4.5(b).

(a)

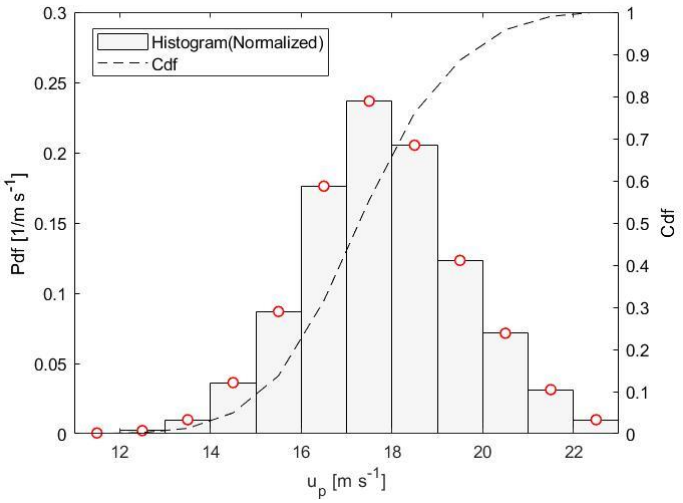

(b)

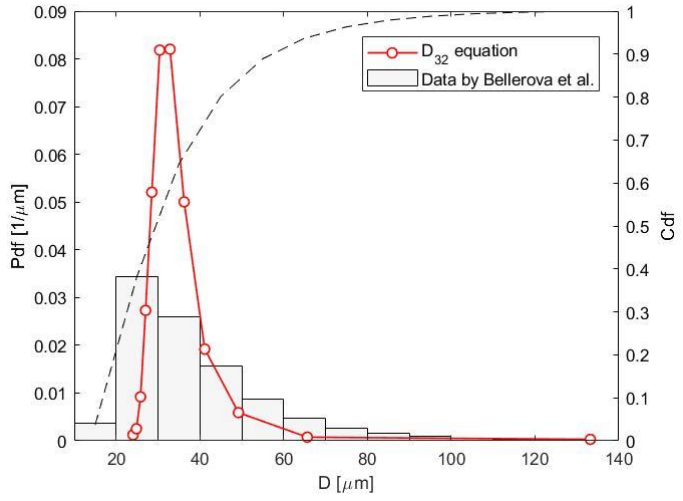

Fig. 4.5 Comparison of discrete probability for the liquid jet in cross-flows of gas. Experimental data by Bellerova et al. [53]. (a) The number of divisions within the range of 11 to 23m/s is 12 with a bin width of 1m/s for the histogram of drop velocity u_p; (b) The number of divisions within the range of 10 to 140 μm is 13 with a bin width of 10μm for the histogram of drop size D

It is noticeable from the comparison in Fig. 4.5(b) that the derived Pdf shows a sharper and higher peak towards the mean value than the histogram, whereas the effective range of D or equivalently the abscissa range, is not significantly different from that of the histogram, indicating a relatively lower standard deviation for the derived Pdf. ; the abscissa is set to span between valid values at both limits, i.e., Pdf > 0 for the minimum and maximum of D from the histogram, although some of the height in the plot seems hardly identifiable wherein a very low Pdf exists. As we will see in Fig. 4.6(b) that the same features are found for the liquid jets in coaxial-flows of gas.

Fig. 4.6 is for the liquid jets in coaxial-flows of gas, applying the same procedures to obtain the derived discrete probability distribution Pdf(D) as Fig. 4.6(b), from the sparse samples of u_L marked in red circles at the histogram as Fig. 4.6(a), and then use the Pdf(u_L) into the D_{32} equation. The common features distinguish in the distribution of Fig. 4.6(b) as well as Fig. 4.5(b); the distribution range over spreading out is not significantly deviated from the one with histogram whereas the standard deviation gets much lower than that, showing intensively concentrated distribution towards mean value like Fig. 4.5(b). This tendency may imply that the aid of gas momentum causes devastating secondary atomization including coalescence, collision, ruptures, and so on. Unlike primary atomization in which the injection condition is the main cause to influence, e.g., weber number, so that it can be controllable, secondary atomization, however, occurs in circumambience where unpredictable dynamic interactions are prevalent between drops, ligaments, and pieces of torn sheets. Therefore, tracking individuals could be hardly sensible, but rather it may be pertinent to see that secondary atomization is regarded as an increase in randomness in the process of primary

atomization. This mitigates against heightened mean value so that it makes a gradual convergent distribution with a higher standard deviation; the higher standard deviation indicates the increased amount of variation of values for a given confidence interval.

(a)

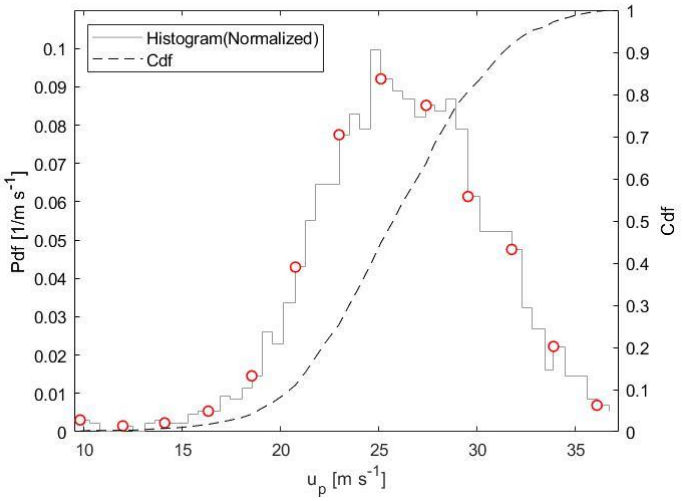

(b)

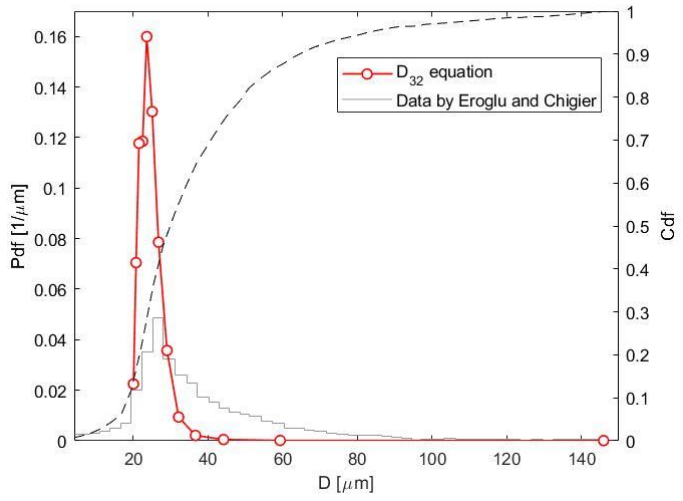

Fig. 4.6 Comparison of discrete probability for the liquid jet in coaxial-flows of gas. Experimental data by Eroglu and Chigier [61]. (a) The number of divisions within the range of 9.5 to 37.2m/s is 50 for the histogram of drop velocity u_p; 13 samples out of among are chosen sparsely as Pdf(uL) to apply to the D_{32} equation; (b) The number of divisions within the range of 4.3 to 150μm is 50 for the histogram of drop size D

The increased randomness is one of the well-known characteristics of turbulence. The turbulence mixing, explained by stretching the range of length scales toward smaller ones for kinetic energy transfer, is broadly accepted in the field of study. Considering that our equations correlate drop size with drop velocity explicitly, it would be possible to draw the velocity distribution from the final drop size distribution so that the secondary atomization can be related in view of the turbulence effect with the velocity variations. Since we study within the scope of primary atomization only, the investigation of secondary atomization remains future work.

In effect, the way of selecting u_L among the range of velocity in the histogram, in which only a few discrete values are chosen with a uniform interval, could be quite arbitrary. Since the derived drop size distribution depends on the selection of u_L, the resultant one is liable to be arbitrary too. Furthermore, the detection and collection of a large number of small drops in experimental measurements are challenging in obtaining a data set with a satisfactory level of accuracy, hence individual values for each bin in the histogram also have the same issue. For these reasons, building the distribution with only a few representing values, i.e., from sparsely sampled u_L, could be inadequate. Therefore, it is a worthwhile attempt to complement the method with a subsidiary device for constructing better practical drop size distribution.

In the followings, a different approach is tried with the same experimental data used above. Specifically, a continuous normal distribution is introduced with an intention of the reduction in risk-taking on the discrete sampling from the velocity histogram. First, both mean and variance are estimated from the set of velocity data to make a normal distribution. Secondly, we regard the whole normal distribution of u within the truncated

range as the probability distribution of u_L; the truncated range of u is limited between the minimum and maximum of u from the data set. Third, D_{32} equations are applied to the range of u_L, then the probability distribution of D is derived by matching to the corresponding distribution of u_L, i.e., Normal distribution(u_L) = Probability(D). Lastly, normalization by area is carried out to complete building the derived probability density function of D, Pdf(D).

Fig. 4.7, Fig. 4.8, and Fig. 4.9 are the results of using the normal distribution for the case of the pressurized-straight liquid jet, the jet in cross-flows, and the jet in coaxial-flows respectively. In Fig. 4.7(a), the continuous normal distribution of u is compared with the discrete histogram whose normalization is fulfilled. In Fig. 4.7(b), the derived drop size distribution Pdf(D) is shown after calculation by the D_{32} equation of Eq. (3.8) for the u_L with the same range of normal distribution of u. In addition, the normal distribution of D from the experimental data is estimated as well, along with the histogram, illustrated all together for the comparison among them in Fig. 4.7(b).

Fig. 4.7(b) shows that the derived Pdf(D) with the D_{32} equation in red line, is more similar in shape than the estimated normal distribution from data in black line, albeit some deviating from the histogram. As for the statement of similar in shape, it intends the extent of closeness for the peak and variance to the histogram's ones; for the variance, the full range of abscissa does not significantly different among them. Given that, the peak and variance of the derived Pdf(D) with the D_{32} equation are more in favor.

(a)

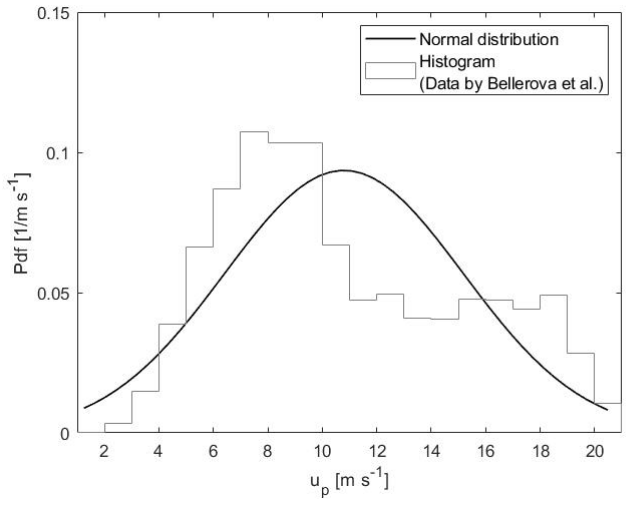

(b)

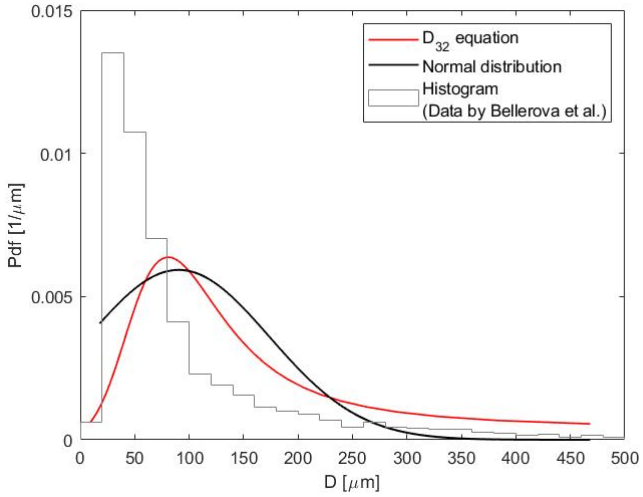

Fig. 4.7 Comparison of continuous probability for pressurized-straight spray. Experimental data by Bellerova et al. [53]. (a) The normal distribution of u from the dataset of drop velocity u_p; (b) The probability density function of D using the normal distribution of u and D_{32} equation with red line, and the other one using normal distribution from the dataset of drop size D with black line

However, it is worth noting that in the case of pressurized-straight jet, making use of normal distribution gives a worse result as far as deviating from the histogram, when compared to using the former method; it comes to be obvious in comparison between Fig. 4.4(b) and Fig. 4.7(b). The different outcome between them could be interpreted such

that, the secondary atomization effect is relatively weak when without gas momentum so that using data directly with sparsely sampled u_L represent already well, as sufficiently characterizing in deriving their drop size distribution. Conversely, this implies that with added gas momentum, making use of normal distribution would give a more favorable result as we will find in both Fig. 4.8(b) and Fig. 4.9(b).

Fig. 4.8 is the result by using the normal distribution of u for the liquid jet in cross-flows of gas. In Fig. 4.8(b) the resulting derived Pdf(D) shows more skewed as resembling the histogram, whereas the normal distribution of D is dampened in shape. In the comparison of the derived Pdf(D) between Fig. 4.5(b) and Fig. 4.8(b), the make use of normal distribution yields a more satisfactory result. To be specific, while Fig. 4.5(b) shows too sharp at the peak to be persuasive, Fig. 4.8(b) shows a moderate peak with gradual smoothing out leading to a favorable agreement with the histogram.

Fig. 4.9 is the result by using the normal distribution of u for the liquid jet in coaxial-flows of gas. In Fig. 4.9(b) the common aspects are found we have seen in Fig. 4.8(b); skewness for the derived Pdf(D), and dampened for the normal distribution of D. From the comparison between Fig. 4.6(b) and Fig. 4.9(b) as well finds the normal distribution of u for Pdf(D) with a modest peak better in resemblance to the histogram.

Consequently, for the liquid jet with added gas momentum as in both Fig. 4.8 and Fig. 4.9, the drop size distribution using the D_{32} equation with the normal distribution of u led to a benign outcome. To explain, we have compared four drop size distributions from different methods, histogram by D dataset, derived Pdf(D) by sampled u_L, derived Pdf(D) by the normal distribution of u dataset, and normal distribution by D dataset. And we have compared each peak; for variance, the effective range of D is limited similarly

for all of them, so the comparison of variance is associated with that of peak height ultimately. The peak height has shown in this order; Pdf(D) by sampled u_L > Pdf(D) by the normal distribution of u > histogram of D > normal distribution of D.

(a)

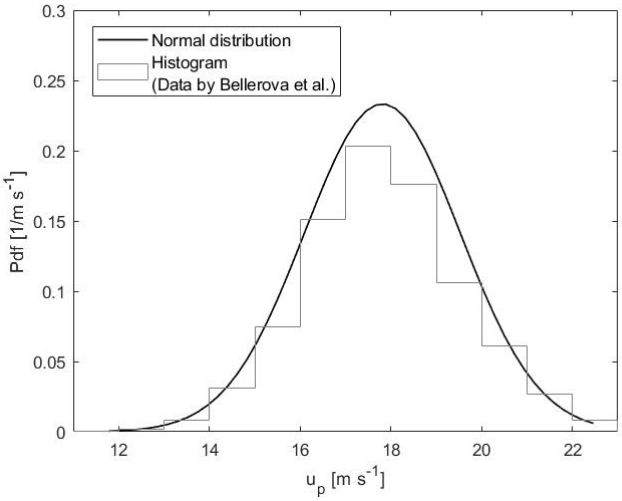

(b)

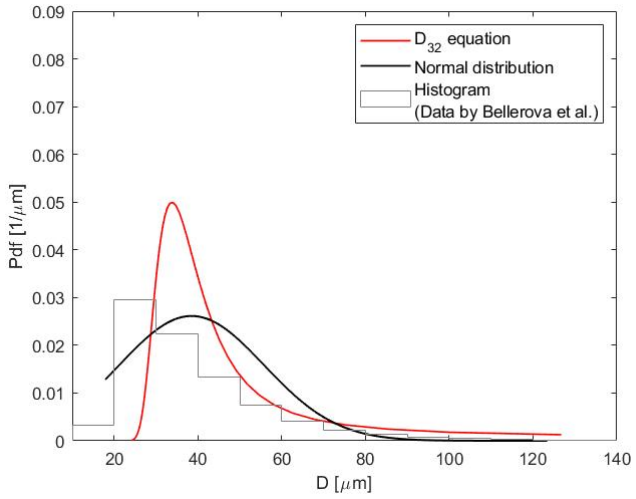

Fig. 4.8 Comparison of continuous probability for liquid jets in cross-flows of gas. Experimental data by Bellerova et al. [53]. (a) The normal distribution of u from the dataset of drop velocity u_p; (b) The probability density function of D using the normal distribution of u and D_{32} equation with red line, and the other one using normal distribution from the dataset of drop size D with black line

(a)

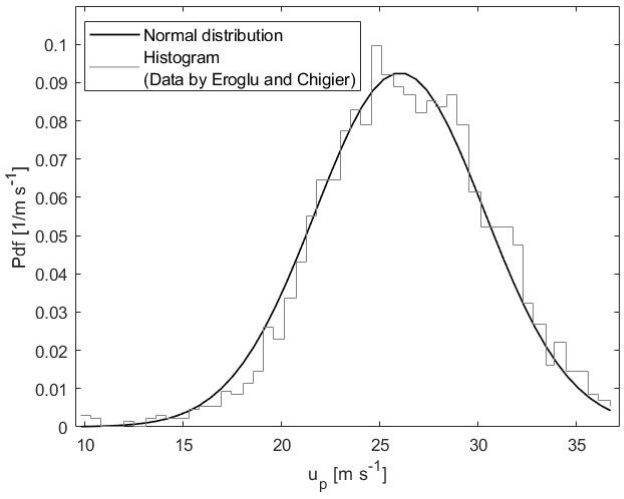

(b)

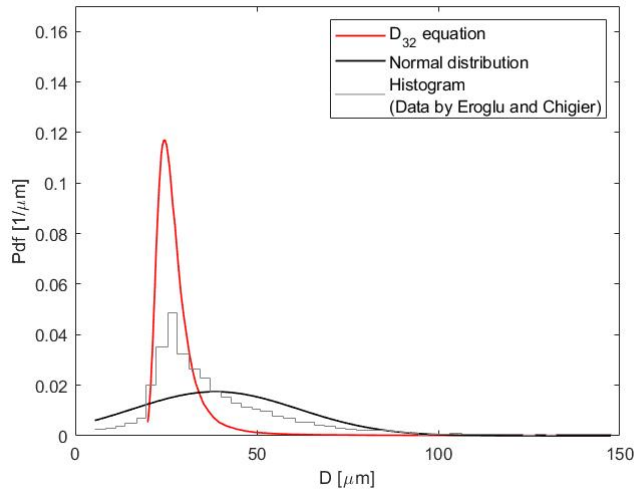

Fig. 4.9 Comparison of continuous probability for liquid jets in coaxial-flows of gas. Experimental data by Eroglu and Chigier [61]; (a) The normal distribution of u from the dataset of drop velocity u_p; (b) The probability density function of D using the normal distribution of u and D_{32} equation with red line, and the other one using normal distribution from the dataset of drop size D with black line

We have studied two different methods in the formation of drop size distribution. Note that one makes a discrete probability distribution, while the other makes a continuous probability distribution that is a probability density function. The former method tolerates the possible inaccuracy triggered by choosing discrete u_L arbitrarily. The

latter one rectifies the shortcoming by taking a continuous u_L, so that it can secure a level of acceptance as taking more broad and generalized possible outcomes. Especially, this aspect takes advantage of embracing possible variations that are involved in unmeasurable effects, e.g., secondary breakup or coalescence. Indeed, in aid of gas momentum, the derived Pdf(D) by the latter method manifests in favor of the data rather than one by the former method; we postulated that gas momentum draws drastic secondary atomization so that drop size distribution entails the impact of untraceable dynamic interactions among a myriad of drops.

The construction of drop size distribution with D_{32} equations benefits from the instance where momentum data are available since it converts from the liquid momentum data to the drop size distribution. This aspect is useful because in most measurements and computational simulations the velocities are easier to measure or compute than the drop size. For example, Volume-of-Fluid simulation makes it convenient to obtain the velocities in the liquid column or sheet prior to the breakup, to calculate the initial drop sizes by D_{32} equations.

4.5 Chapter Summary

In the previous chapter, we used the integral form of the conservation equations of mass and energy to formulate a general expression for the drop size in various spray injection geometries. Adding the current momentum analysis completes this formulation, which also brings forth a broad dynamical perspective of spray atomization; liquid momentum is altered through interaction with the gas by drag, and this momentum exchange incurs the corresponding change in the kinetic energy of the liquid and the gas.

This deduction in the liquid kinetic energy must appear in another form, which is the surface tension energy. Thus, the larger reduction in the liquid momentum and therefore its kinetic energy, the smaller the drop size will be.

The current full formulation puts this perspective in a relatively simple mathematical form, and the resulting D_{32} equation yields the drop size and its distribution as well, showing in close agreement with experimental data across various injection configurations. From the comparison with experimental data, we have found the conversion of the liquid drop to gas velocity is needed to correlate the drop size to momentum data, in gas-driven atomization processes such as liquid jets in cross- or coaxial-flows of gas. This momentum analysis can be done for a global control volume, in differential formulation involving computational fluid dynamics, or directly from the measured velocity dataset.

In conclusion, the momentum analysis is verified as generalizable across a range of spray injection geometries, thus drop size and its distribution can be obtained without complex computations or modeling.

CHAPTER 5

COMPUTATIONAL PROTOCOL FOR SPRAY FLOWS, INCLUDING PRIMARY ATOMIZATION

5.1 Basic Spray Geometries

Background

In this chapter, we explore how the above mathematical formulation of primary atomization may be utilized in a computational fluid dynamics, CFD framework. To be specific, we investigate the basic spray geometries; pressurized-liquid jets without and with swirl, and liquid injected into a cross-flow of air. The configuration of straight liquid jets with no swirl is used in Diesel and automotive fuel delivery, while swirl injectors are used in compact combustors as in gas-turbine engines. Liquid jets in cross-flows are used in aircraft fuel injection and industrial gas turbines. Thus, the basic spray geometries vary depending on their use and are important to befit their purpose.

Existing CFD algorithms for the continuous liquid and dispersed phases are quite effective if initial and boundary conditions are fully specified. Volume-of-Fluid or Level-Set methods reproduce the liquid motion and deformation quite well at flow length scales. However, small-scale liquid shearing leading to droplet formation occurs at length scales mostly below the spatial resolution of large-eddy or turbulence model simulations. Also, existing primary atomization modules require time-dependent tracking of the liquid-gas interface even for steady-state injection processes [25,26], straining the computational resources. Therefore, even in advanced high-resolution computer simulations, a more practical form of primary atomization module is required for the drop formation.

By the way, if the droplet initial size and velocities can be specified from some local initial conditions, then algorithms such as particle-in-cell or Eulerian-Lagrangian methods work quite well in tracking the droplet trajectories. Mass and energy transfer modules can also be added with good accuracy, to study evaporation and combustion processes in sprays; though additional tasks in the computation of the droplet formation processes or specifications of drop size, would require.

Eventually, the key component is the primary atomization module to link the pre- and post-atomization simulations. In this light, our primary atomization theory can be applied within the CFD modules, making the primary atomization module in spray flow simulation effective, which has proven to work quite well [54,55].

Method

The analytical results described in the previous chapters 3 and 4 have several strengths when used in the primary atomization module during the computational simulations of spray flows. First, our theory is based on the fundamental fluid physics of mass and energy conservation. Secondly, it has been generalized and validated across all the major injection geometries [46–52]. The fact that it requires liquid velocity as input to D_{32} equations, Eq. (3.8) or Eq. (3.11), points to the ideal integration of the equations with existing computational algorithms that we can obtain numerically solved velocity or momentum data.

Especially, time-averaged velocities are needed as inputs in D_{32} equations, so that steady-state simulations are sufficient for the pre-atomization with VoF. For transient injection processes, unsteady VoF can be run. However, here we only consider steady-

state spray flows. In this way, we run pre-atomization liquid-phase simulations using the VoF method in CFD, to compute a continuous liquid velocity development from an injector exit to atomization planes.

The location at the atomization plane is specified using a suitable physical criterion as described below. Then, the liquid velocities from VoF are input to D_{32} equations to specify the local droplet size. Subsequently, the dispersed simulation can be initiated using this droplet size along with the local liquid velocity for the post-atomization process. The Steps are outlined as follows.

1. Run liquid-phase simulation with VoF to obtain liquid volume fraction and local velocity for the pre-atomization liquid flow field
2. Apply the atomization criterion; described below
3. Use the local liquid velocity in D_{32} equations to derive the local initial drop size
4. Run Lagrangian discrete particle simulation DPM to track the droplets, using the above initial drop size from Step 3 and velocity from Step 1

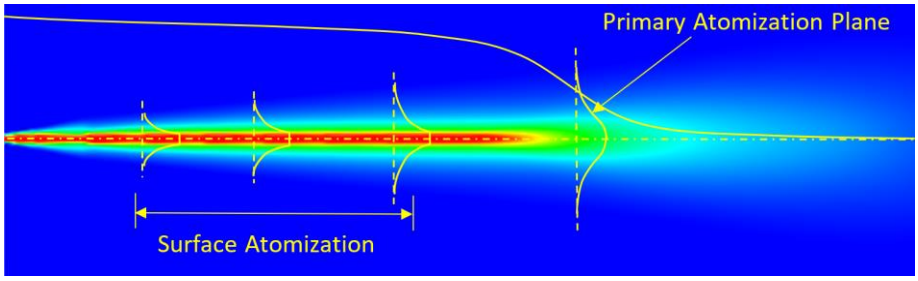

Fig. 5.1 A schematic of the computational protocol for straight liquid jets. The continuous liquid phase is computed, then local D_{32} of Eq. (3.8) and liquid velocity are used to initiate the discrete phase simulation at the surface and the primary atomization plane

Fig. 5.1 shows the schematic of the above procedure, where the liquid volume fraction and velocities from the VoF simulation are used in Steps 2 and 3. Then, Discrete-Phase Model, i.e., DPM, can be run. Both the VoF and DPM are run on ANSYS-Fluent for the current work. Most CFD softwares have VoF and DPM functionalities, and we add Steps 2 and 3 into this sequence. To account for turbulence, the realizable k-ε model is used. Only the mean velocities are needed so that steady-state simulations are sufficient, requiring minimal computational resources.

(a)

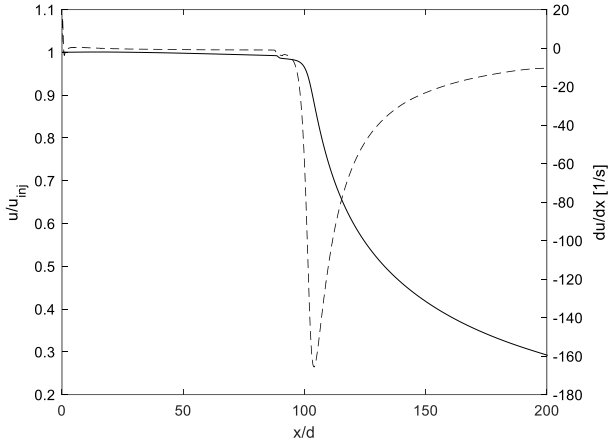

(b)

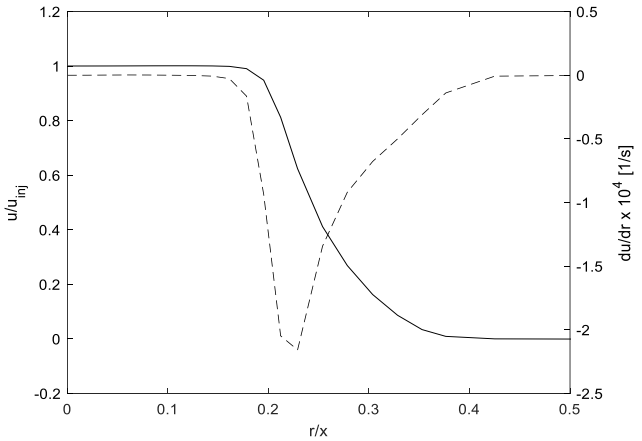

Fig. 5.2 (a) Axial centerline profiles of the velocity and its gradient; (b) Radial profiles of the velocity and its gradient. These velocities and gradients are used for (a) the primary atomization at the spray tip, and (b) surface atomization along the periphery of the liquid column

The liquid velocity profiles in the radial distance, i.e., cross-stream direction, are used for the “surface atomization”, where along the periphery of the liquid column. For example, Fig. 5.2(b) shows both the liquid velocity and its gradients. The atomization criterion is the velocity gradient exceeding ½ of the maximum; the absolute value of the negative gradient, as shown in Fig. 5.2(b). Due to shear stress, the velocity decreases from the centerline value toward the periphery, and the velocity gradient has a negative minimum, i.e., absolute maximum, near r/x of 0.25. Within 50% of this absolute maximum, the liquid is considered atomized. And local liquid velocity is input into Eq. (3.8) for the local initial drop size. Three to six surface atomization locations were selected along the x-direction, in order to ensure continuity in the discrete-phase, but the final number and exact locations did not affect the results to any noticeable degree. At each axial surface atomization with these x-locations, 5 annular zones were used to input varying liquid velocities and corresponding D_{32}, according to Eq. (3.8).

For the “primary atomization”, where all the remaining liquid is converted to discrete droplets, the axial velocity gradient is used seen in Fig. 5.2(a). And the location of the maximum gradient, i.e., the absolute value of the negative gradient, is used as the primary atomization plane. This follows from experimental and computational observations where the liquid core undergoes a relatively abrupt disintegration leading to the formation of a majority of atomized droplets. Surface atomization is observed up to this point, but simply due to the relatively small droplets, the “primary atomization” constitutes the major bulk of the atomized droplets.

For swirl injection, a similar procedure is followed, except that the atomization is assumed to occur across the liquid sheet at several axial locations of 1, 2, 3, and 5mm

along the centerline, i.e., no surface atomization was separately input, unlike the straight liquid jet. This as well follows from experimental observations where swirl injection leads to nearly immediate breakup and production of droplets across the liquid sheet.

A uniform Cartesian axisymmetric mesh with a cell height of 0.475mm in the VoF simulations is used for the liquid column calculation. The mean liquid trajectory is symmetric about the centerline of the jet, allowing a two-dimensional axisymmetric solver to be valid. The computational domain is 2m long and 0.25m tall. Water at the injection velocity of 56.7 m/s is sent into a quiescent, air-filled domain from an inlet with a diameter of 9.5mm. The inlet turbulence intensity is set to 3% and uses the hydraulic diameter of the injector as 9.5mm to accurately model the turbulent kinetic energy and dissipation rate at the inlet. The realizable k-epsilon viscous model is used to model turbulence as the injector inlet which has a typical Reynolds number of 10^5, thus the flow is fully turbulent. Additionally, the average liquid trajectory and velocity are desired in this work, which is provided through the k-epsilon two-equations model along with RANS viscous model equations during DPM. Implicit, dispersed interface modeling is enabled to capture the liquid-gas interface. The field is solved in a steady-state solver until convergence. A coupled method with a second-order discretization solution scheme solves the flow, in which coupled velocity and pressure are to be determined for the liquid velocity distribution while it enforces the continuity equation.

In the discrete phase computations, annular or circular area injection mode is used with the local drop size of D_{32} specified as described above. Unsteady particle tracking is used with a time step of 10^{-7} seconds. Particle rotation, discrete random walk,

and the Saffman lifts are all included during the particle tracking, to simulate realistic dispersion of the particles.

The number flow rate, i.e., $\dot{n}_i = \dot{m}_i/ (\pi/6)D_i^3\rho_L$, the local mass flow rate based on the liquid velocity, i.e., $\dot{m}_i = \rho_L(u_L)_i A_i$, is used for the annular area in surface atomization, as well as the circular area in primary atomization, that involved in the breakup process. Although the drop size distribution can be input, however for the current study, local D_{32} is input in this discrete-phase simulation, since variations in the local liquid velocity lead to a natural spread in the distribution of the final drop size. Fundamentally, diverse velocity field yields varied in drop size according to Eq. (3.8). For example, large u_L/u_{inj} corresponds to large D_{32}, and vice versa, hence resulting in various drop sizes in local. And, their subsequent drop trajectories allow for the "mixing" of these particle sizes, making the variations in the sampled D_{32}.

Results and Discussions for Pressure-Atomized Sprays without and with Swirl

To summarize the protocol introduced briefly, we run the steady-state simulation of the continuous liquid core using VoF, then use the velocity profiles to input into Eq. (3.8) to obtain the local drop size D_{32}, and finally, droplets with the D_{32} are released at the local liquid velocities in Lagrangian tracking of droplets DPM.

The computational results obtained from the above protocol are compared with various experimental results for pressure-atomized sprays without swirl [62–64] and with swirl [65]. Among those data, the velocity and droplet size near the liquid surface by Ruff et al. [62] is used for the validation as seen in Fig. 5.3(a) and Fig. 5.3(b) respectively. The data finds that the drop velocities and SMD are high near the liquid column surface, then

both decrease in the radial direction. As it turns out this observation is well reflecting our results of the computational simulation and derived drop sizes. To describe from the simulation with a continuous liquid jet, the centerline velocity is highest and then decreases toward the periphery. This indicates that large liquid velocities close to the surface would produce or be associated with large droplets according to Eq. (3.8) and Fig. 3.1. Conversely, low liquid velocities are correlated with small droplets. Therefore, it displays analogous characteristics to the experimental observation.

When the droplet velocities were tracked in the Lagrangian simulation, in which the particle reflects the droplet dynamics through changing velocities along its trajectory, it showed that the initial liquid velocity was getting retarded by the drag with the surrounding gas. This observation was also carried out to ensure our procedure integrity, but, since it is not an essential but rather a subsidiary measure, we place that observation here with only such supplementary explanation but skip details.

In Fig. 5.3(b) the droplet behavior is fairly well simulated in the current method. However, some deviation between both velocity profiles is shown in Fig. 5.3(a), implying the existence of perturbations in practice relative to the average by various causes. For example, the drop velocity from measurement is overestimated in Fig. 5.3(a). Computationally, the turbulent fluctuations can introduce variations in the drop size and velocity, that may lead to better accordance with those of measurement. Although this can easily be taken into account, it has not been added to the current computational module. Moreover, the measurement by Ruff et al. [62] was made using double-pulsed holography so that sampling and data analyses inherently contain some extent of errors.

Still, the agreement between the simulation and data is encouraging, as the SMD is in quite good agreement given the low computational cost with grid requirements.

(a)

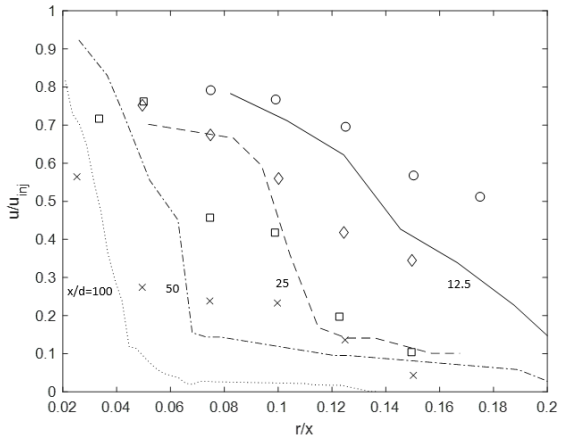

(b)

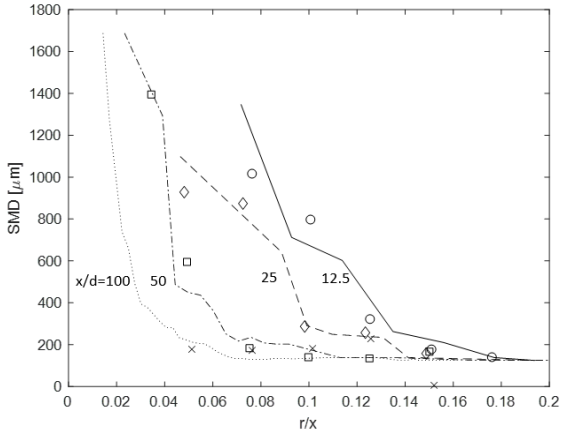

Fig. 5.3 Comparison of the computed drop velocities (a), and drop sizes (b), with measurements by Ruff et al. [62] for pressure-atomized water spray without swirl. The u/u_{inj} and SMD are plotted as a function of r/x, which is the radial similarity variable at various x/d locations

The spray shape is visualized by the contour plot of the drop number density as shown in Fig. 5.4. The transition from continuous liquid core to dispersed droplets is abrupt at x/d ~ 100. The reason for that is, the atomization criterion corresponding to the

maximum negative centerline velocity gradient has been applied at this point. In addition, it shows that the droplet number density following this atomization criterion of liquid core break-up is an order of magnitude higher than surface-atomized droplets in the periphery of the liquid jet. This contour appears coincident with our previous statements that the majority of droplets in experimental observations are occupied by the bulk droplets coming from the primary breakup.

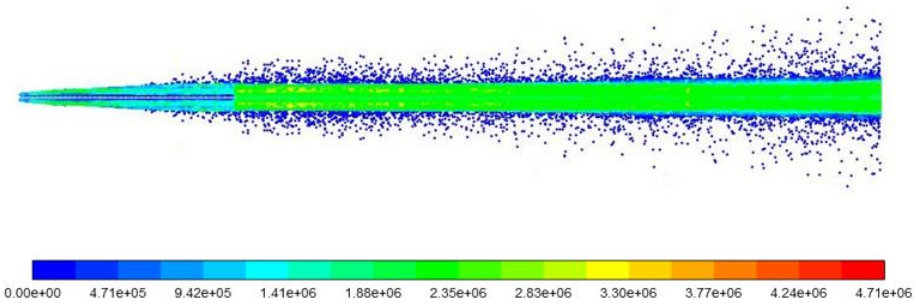

Fig. 5.4 Contour plot of the drop number density for pressure-atomized sprays without swirl. The inner part of the spray has a nearly constant drop number density beyond $x/d_{inj} \sim 100$, indicating at the end of the liquid core, both physically and computationally

In addition to Ruff et al. [62]'s experiment with water spray, two more comparisons for pressure-atomized diesel jets are made. In this study, our simulation is referred to the experiments by Martinez et al. [63], and Lee and Park [64]. These data sets for diesel injection are compared with the simulation results, as followed the same procedure outlined in the previous context. With the same geometry for pressure-atomized straight jet, else parameters were handled to be matched with the referred experimental conditions, e.g., modified injector diameter, fluid properties, and injection

operation. And their results in comparison are quite favorable as shown in Fig. 5.5 and Fig. 5.6.

Overall, from the comparison studies with the three independent experimental observations for pressure-atomized jets in different parameters, our approach is demonstrated as a versatile tool to handle various spray flow simulations efficiently. It showed acceptable performance in visualization as well as convincing results, supporting our theory and its application into CFD.

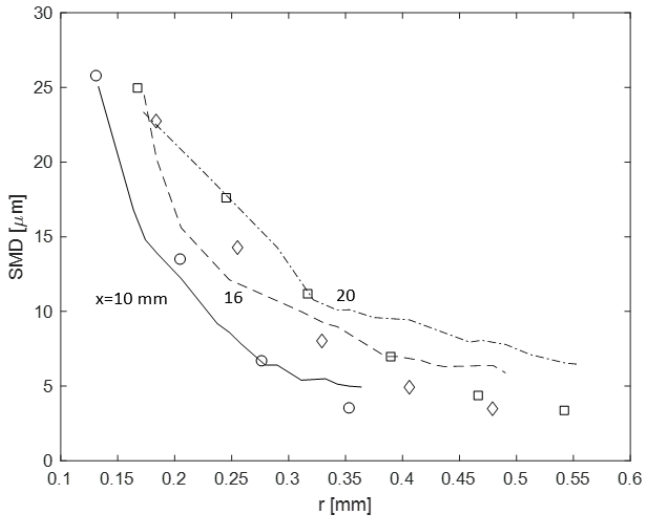

Fig. 5.5 Comparison of the computed SMD with measurements by Martinez et al. [63], for diesel spray with an injection diameter of 186μm and injection pressure of 50MPa. The SMD is plotted as a function of r, at various x locations

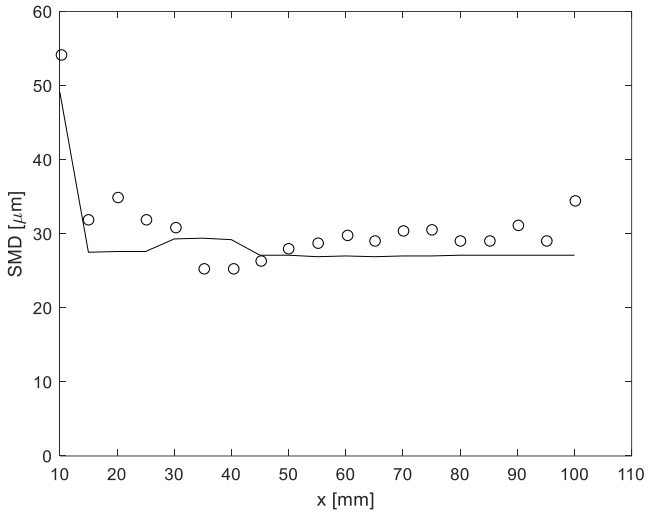

Fig. 5.6 Comparison of the computed and measured centerline SMD with measurements by Lee and Park [64], for diesel spray with an injection diameter of 0.3mm and injection pressure of 80MPa

For swirl injection, a tangential velocity component is accounted at the injector exit in addition to axial velocity. It makes a bell-shaped liquid sheet as we will find in the continuous liquid VoF of Fig. 5.7(a). Due to the thin sheet shape against the swirling motion, it undergoes severe shearing in multi-directional and ends up in rapid break up. Furthermore, the drag coefficient of the sheet shape is expected to be large, leading to a rapid reduction in liquid velocity. Indeed from the VoF simulation, we find the liquid sheet rapidly slowing down. Hence, the induced large drag in addition to the swirling motion would cause atomization near the injector exit.

The atomization criterion for swirl sprays is set at the point of maximum negative velocity gradient in the same manner as for the pressure-atomized sprays. The 5 locations at x = 0.47, 1, 2, 3, and 5mm are selected, where much close to the injector compared to that for pressure-atomized sprays. This accords with the earlier explanation of rapid break

up near injector exit. After making a decision on the atomization plane, the remaining procedures follow the same computational protocol; the velocity profiles on several atomization planes are extracted from the resulting VoF simulation of continuous liquid in order to calculate the initial drop size by the D_{32} equation in Eq. (3.8).

Having furnished the initial drop size and its velocity in DPM simulation, it visualizes the track of discrete droplets as shown in Fig. 5.7(b). The number flow rate for the droplets is prorated by the liquid centerline velocity at each injection point, so that the total number flow rate multiplied by the liquid density and droplet volume equals the injected mass flow rate.

Fig. 5.7(b) displays the spray shape by using the drop number density. The lobes in the periphery of the spray are due to two factors; first, there is a similar lobe in the liquid velocity simulation in Fig. 5.7(a) so that the droplet mean motion may follow that path, and secondly, discrete injection locations may lead to such lobes, which can be remedied by increasing the number of injection planes.

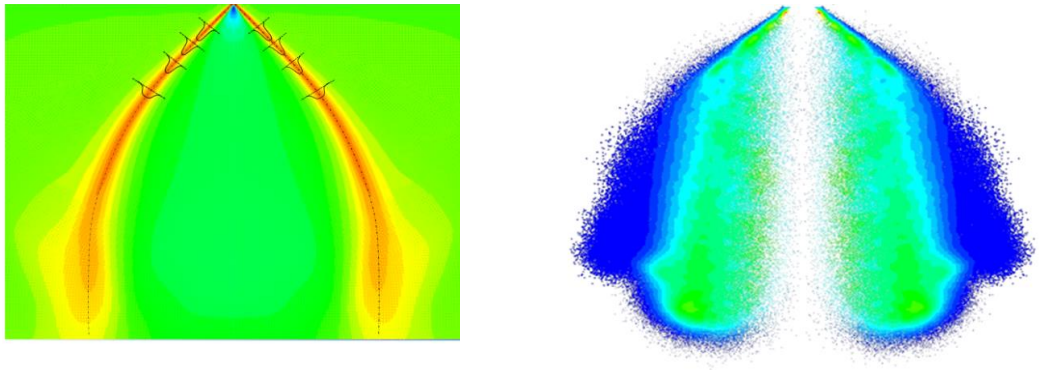

(a) Velocity field in VoF

(b) Drop number density via particle tracking in DPM

Fig. 5.7 Simulation for swirl sprays. The velocity profiles at several atomization planes are extracted along the liquid sheet, to initiate the DPM as schematically shown in (a); locations are approximated for the illustration purpose

After the above simulations for the swirl sprays, the obtained velocity profile and calculated drop size at specific locations of x = 8 ~ 20mm are plotted in order to compare with the experimental data from Marchione et al. [65], as in both Fig. 5.8 and Fig. 5.9. The drop size is quite well reproduced as shown in Fig. 5.8(b) and Fig. 5.9(b). But the profiles, which are in the radial distributions of the droplets, are further out in the radial direction than the measurements up to x = 14 mm. This may have to do with the initial velocity vector, and since the liquid sheet is curved in swirl sprays, any deviations in the initial velocity vector will lead to spreading in the drop size profiles. Beyond x = 14 mm, the trajectories of the droplets agree reasonably well, and this is due to the re-alignment of the velocity vectors for the droplets injected at the furthest point of x = 7mm. This points to the need for fine-tuning the injection location to apply Eq. (3.8) in this type of simulation.

For the droplet velocity, there is a decent agreement for the peak velocity magnitude and locations, although similar deviations in the width of the velocity profiles are observed. Also, in the simulations very low droplet velocities appear in the periphery of the spray that are both ends of width in profile, whereas the minimum measured drop velocities are 5 to 6 m/s in Fig. 5.8(a) and Fig. 5.9(a). For the calculated SMD profile, it finds that lowered liquid velocity results in decreased droplet size, and that is an expected feature from Eq. (3.8) and Fig. 3.1.

(a)

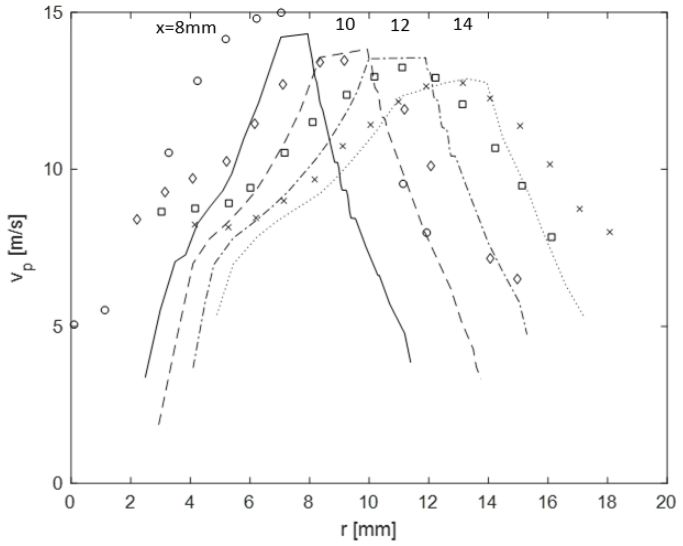

(b)

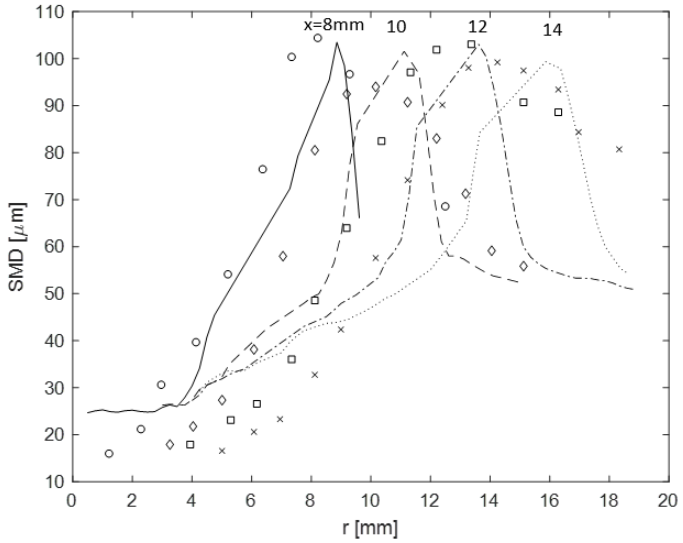

Fig. 5.8 Comparison of computed and measured (a) drop velocities, and (b) SMD, for swirl sprays. They are plotted as a function of r, at various axial distances of x = 8 ~ 14mm. A nozzle diameter of 0.46mm and kerosene Jet A-1 fuel with 7bar are used. The data are from Marchione et al. [65]

(a)

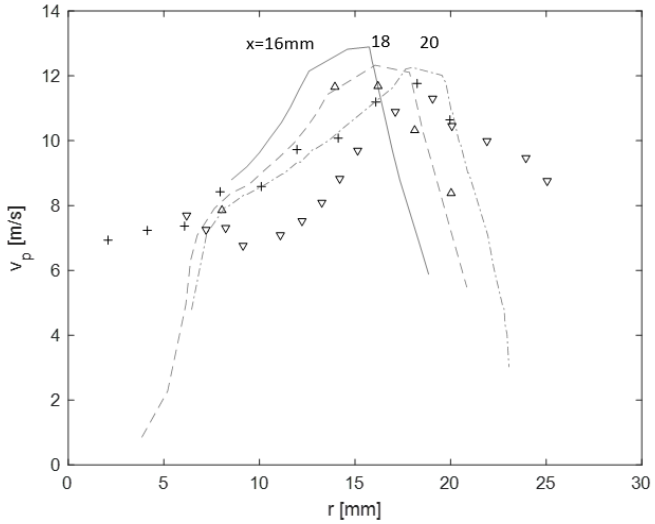

(b)

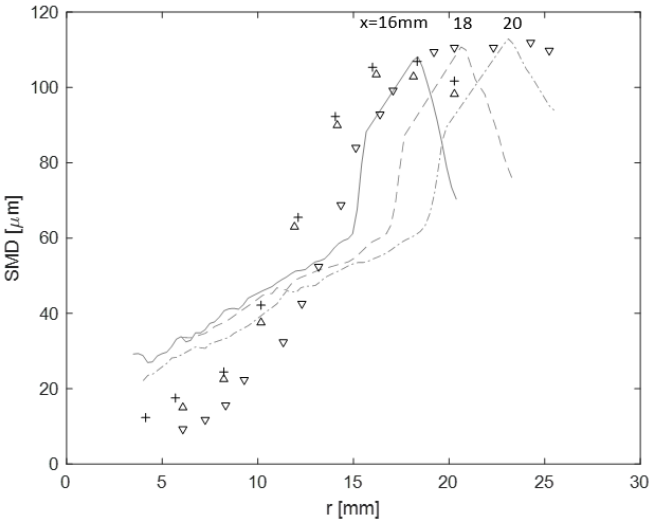

Fig. 5.9 Comparison of computed and measured (a) drop velocities, and (b) SMD, for swirl sprays. They are plotted as a function of r, at various axial distances of x = 16 ~ 20mm. A nozzle diameter of 0.46mm and kerosene Jet A-1 fuel with 7bar are used. The data are from Marchione et al. [65]

Distribution of global drop size can be made by sampling drops from the simulation at x = 20 mm across the spray plane, as shown in Fig. 5.10. Although the drop size distribution, which is made out of such sampling, could not be directly compared

because they were not available from the measurements of reference paper [65], the made distribution shows a typical log-normal shape, which is a commonly found in the distribution of spray droplets from various cases.

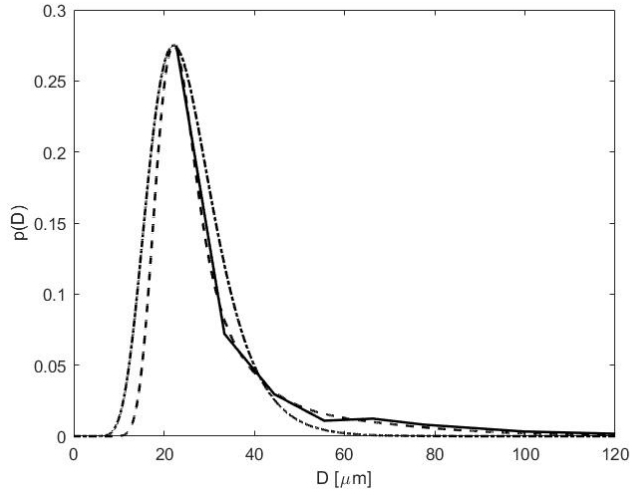

Fig. 5.10 Global drop size distribution p(D) is obtained at x = 20 mm for swirl spray. The solid line is of the sampled droplets from the simulation, while the other lines are lognormal (-··-) and curve (− −) fit to the raw p(D)

Results and Discussions for Liquid Jets in Cross-Flows

For liquid jets in cross-flows, Fig. 5.11 displays its side and front view of the appearance from a three-dimensional simulation after following the same computational steps. Having the three-dimensional structure enables us to capture the multi-angle images in cross-sectional, which is useful in investigating its various aspects in dispersed trajectory. Specifically in our study, the spatial distributions of the droplets in different planes are instructive to distinguish the local spreading degree as displayed in Fig. 5.11. In Fig. 5.11(a), an overall look is quite similar to those of experimentally observed

images [66–68], under similar momentum ratios. To describe, the droplets are concentrated slightly fore from the mid-region of the liquid column, with a little upward direction.

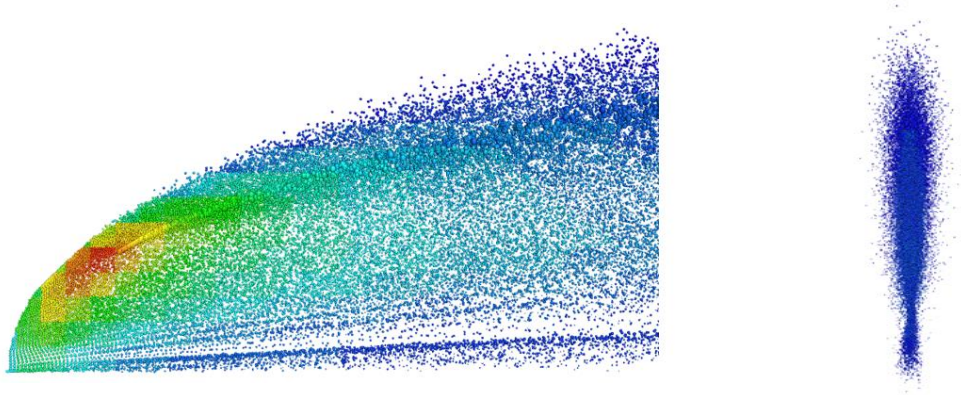

(a) Side view (b) Front view

Fig. 5.11 Simulation for liquid spray in cross-flows. The contours are the drop number density via particle tracking in DPM

The drop size and velocity from computation with the simulation are compared with data from Mashayek's experiment [69]. According to this reference, a high-speed airflow of 40.8 m/s which is perpendicular to a water jet of 9.6m/s was used with a momentum ratio of q =12.3 and a high Weber number of 57.2. The diameter of the water injector was 0.5mm. Based on that setup, our flow simulation was run by Reynolds averaged steady-state turbulence models at a relatively coarse grid spacing of 0.5mm. The computation results are shown in comparison with the experimental measurements, from both Fig. 5.12 and Fig. 5.13.

In the drop velocity profiles of Fig. 5.12(a) and Fig. 5.13(a), the simulation result appears with a more fluctuating plot in the gas velocity along y/d at the same x/d

locations, while the experimentally measured drop momentum is less prone to alternate due to its much high inertia. The computed drop velocities are lower, ranging from 10 to 15% below the experimental data. Recalling that the initial drop velocity came from the liquid column trajectories prior to any atomization, the gas velocities will tend to be lower in comparison to the actual spray which breaks up into smaller ligaments and droplets, thus less obstructing the gas flow. Although the accuracy in the drop velocity could be improved by compensating for this difference, we used a straightforward way and input the sampled velocity to specify the initial drop velocities, as described in the previous section.

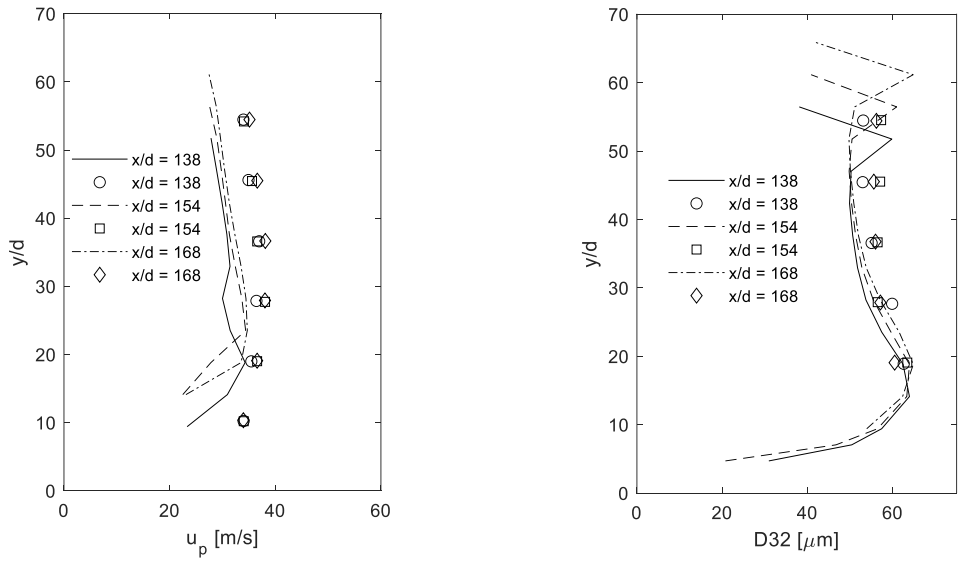

(a) (b)

Fig. 5.12 Comparison of the computed (a) drop velocity, and (b) D_{32} profile, with experimental data from Mashayek [69] for liquid spray in cross-flows. The airflow in x-direction and water injection at y/d = 0. The x/d = 138 ~ 168, d = 0.5mm, data as symbol

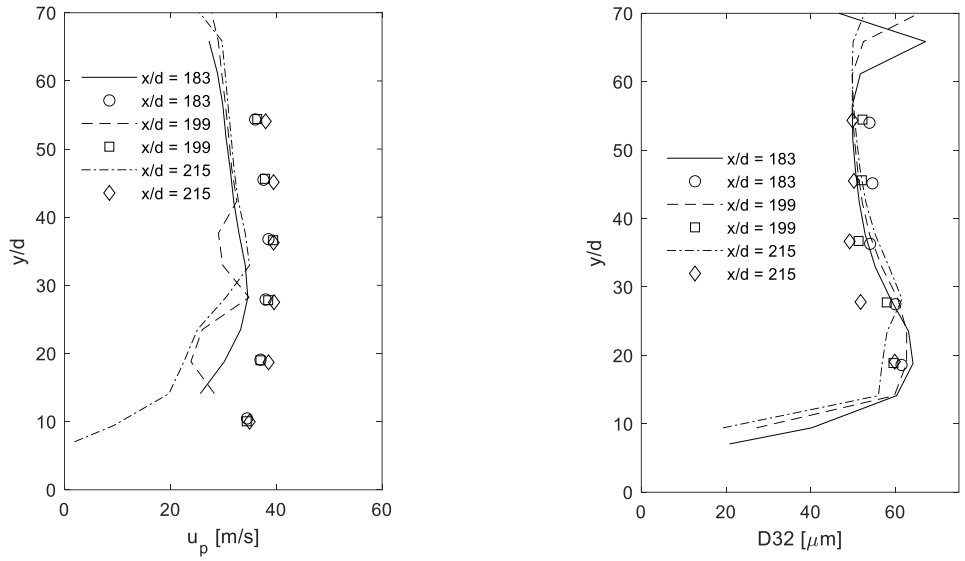

(a) (b)

Fig. 5.13 Comparison of the computed (a) drop velocity, and (b) D_{32} profile, with experimental data from Mashayek [69] for liquid spray in cross-flows. The airflow in x-direction and water injection at y/d = 0. The x/d = 183 ~ 215, d = 0.5mm, data as symbol

The comparison of results in drop size between the simulation and experimental measurement is quite favorable as seen in Fig. 5.12(b) and Fig. 5.13(b). The large drop sizes are found in low height, and drops with decreased sizes are toward the mid-height for most measurement positions of x/d = 138 ~ 215; the height here means that the distance from the liquid injection at y/d = 0. In high heights where the data are reported along the streamwise direction of airflow, the drop sizes do not vary appreciably across the measurement positions in x/d nor y/d, while staying mostly between 50 ~ 60 μm.

In addition to the examination of the spatial profiles for the drop size and velocities with Mashayek's data [69], we further investigate the spray characteristics, including volumetric flux and drop size distribution. For this comparison study, the

experimental measurement by Song et al. [67] is used. The computational procedure is identical, except that the liquid injection and gas inlet velocity need to be differently initialized subjecting to the specific experimental conditions, e.g., momentum ratio of 10 with an air pressure of 6.89 bar. Jet A-1 fuel is used with a liquid injection diameter of 0.508mm which is almost the same size as the one used in the preceding comparison study. Likewise, the airflow is in the x-direction and the fuel injection is at y/d = 0, which are also in the same configuration. The data measurement is made at the position of x/d = 50.

In Fig. 5.14 volumetric flow rate comparison is shown for two different gas weber numbers of 250 and 1000. Because of the signal drop-off during phase-Doppler interferometry measurements, both the raw and normalized data are plotted separately as symbol and dash line, respectively. The normalized volumetric flow rate is obtained by multiplying the raw data by a constant, so that the integrated value is brought equal to the injected mass flow rate.

The agreement with the experimental data is quite reasonable in that the liquid flux is concentrated in the upper part of the flow, implying that the extent of stripping out of the liquid column is considerable near the column fraction height. As being subjected to the stronger weber number, i.e., $We_g = 1000$, the stripping out in the region where below the fraction height occurs in an uncontrolled manner, showing the more rugged volume flux profile found in Fig. 5.14(b).

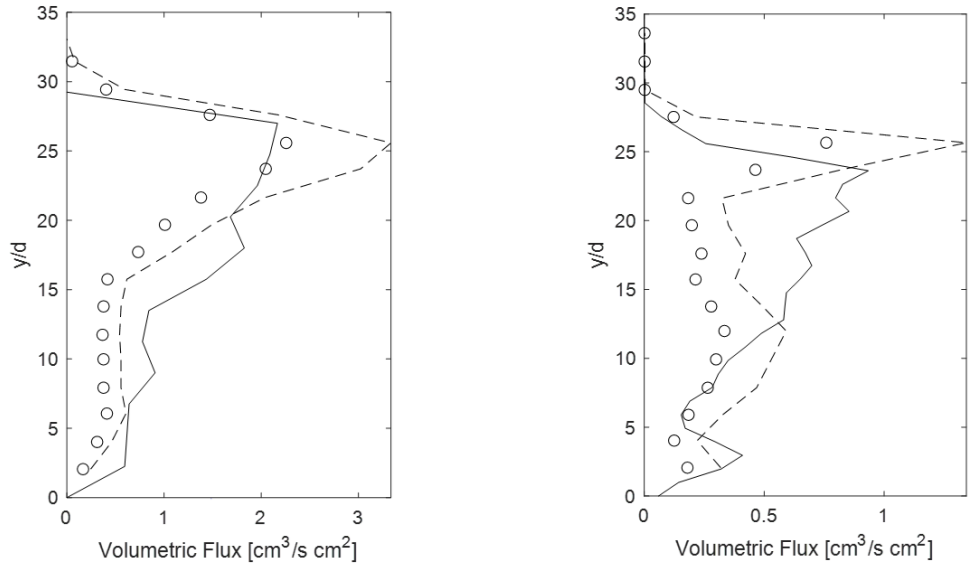

(a) $We_g = 250$ (b) $We_g = 1000$

Fig. 5.14 Comparison of the computed and measured volumetric flux for liquid spray in cross-flows, at x/d = 50. The measured data by Song et al. [67] as symbol for raw data and dash line for normalized data, d = 0.508mm

In Fig. 5.15, global drop size distributions are made for each weber number. It is made with the sampled drops from the computational results across the flow section at $x/d_{inj} = 50$, where the same position as the experiment. The drop size distributions are evaluated for weber numbers of 250 and 1000, and compared with the results by Song et al. [67]. As noted in the previous context, making use of velocity fluctuations into Eq. (3.11) enables the drop sizes to result in varied outcomes from the mean estimate, hence the distribution profile of the initial drop size is obtained. In effect, this idea is coherent since we run simulations with a time-averaged steady-state solver, indicating that the computed mean velocity field is also accountable for such velocity fluctuations. The performance in this way is well verified through the comparison with data in Fig. 5.15, as they appear to be usable in the construction of drop size distribution.

(a) We_g = 250

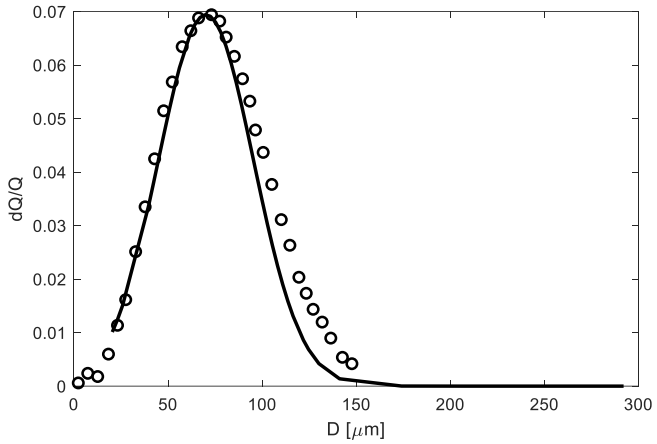

(b) We_g = 1000

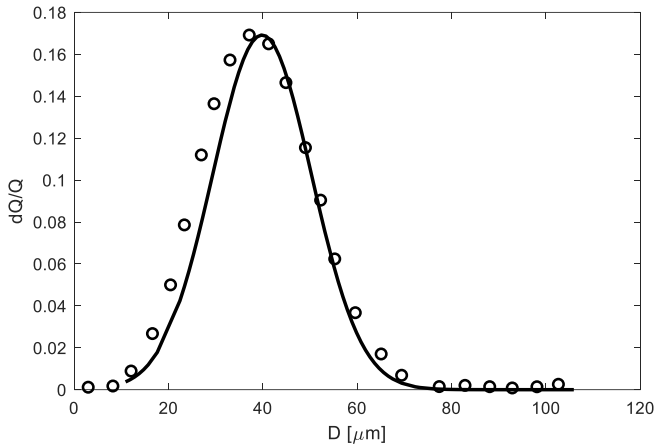

Fig. 5.15 Global drop size distribution for liquid spray in cross-flows, at x/d = 50. The measured data by Song et al. [67] as symbol

Conclusion

Finally, the comparison studies support the validation of D_{32} equations of Eq. (3.8) and Eq. (3.11) as an effective expression for the drop size along with the computational protocols presented. The current agreement and level of accuracy for the drop size are expected as long as reasonably accurate velocities are input.

5.2 Liquid Jets Atomized by High-Speed Gas Flows

Background

Flat spray air-assist nozzles are important in many industrial processes including spray cooling, agricultural sprays, and medical processes. One of the key components in simulating spray cooling flows is the determination of initial drop size during primary atomization. For this reason, much work has been done experimentally and computationally to determine the droplet sizes, including velocities, impact pressure, and surface heat transfer coefficients generated by these nozzles [70–74]. And for these applications, extensive computational studies of air-assist flat sprays have been performed with much focus on the visualization of liquid break-up processes [70–74].

By the way, to fully resolve the phenomenon, the computational requirements can be challenging against necessitating operation conditions, i.e., high Reynolds and Weber numbers. While a high-resolution computation is useful for observing the fundamental break-up processes, it may not practical to apply with routine design iterations. To circumvent unreasonable computational costs, turbulence models based on Reynolds-averaged Navier-Stokes equations or large eddy simulations can be utilized. However, since the length scales required for droplet formation are below the spatial resolution of such computations, a primary atomization model is crucial.

Multiple primary atomization models have been generated and implemented in various spray geometries [25,56,75]. Upon determination of the initial drop sizes through these methods, dispersed-phase simulations can be used to track the droplet motion while accounting for momentum exchanges with the surrounding gas. Likewise, interphase

mass and energy transport also can be added to account for evaporation and combustion. These simulations often are Eulerian-Lagrangian types of algorithms.

In general, with the Eulerian-Lagrangian algorithms, the computation of spray flows can be classified into 1) continuous liquid phase simulation 2) primary atomization module 3) dispersed phase particle tracking. The time-averaged turbulence modeling is applicable for the liquid phase portion of the algorithm with sufficient accuracy. The Eulerian-Lagrangian particle tracking droplet motion and turbulent dispersion models in commercial computational software, such as ANSYS Fluent, have also been deemed sufficiently accurate for this application. This leaves the primary atomization module as the missing key parameter for robust spray flow computations [25,56,75]. For example, Gorokhovski and Herrmann [75] correctly assessed that the determination of the drop size in atomization is needed in modern simulations of spray flows. Existing models of primary atomization are not fully generalizable, requiring inputs of detailed extraction of liquid surface and velocity data [25,56,75].

On the other hand, we have used the integral form of conservation equations to find analytical expressions for the drop size during primary atomization [46–52]. In effect, we have utilized the integral form of the conservation equations to analyze spray atomization for numerous spray geometries [46–52]. Through these analyses, the complex details of primary atomization are circumvented by relating the initial and final energy, mass, and momentum states of the spray flow. In addition, we have shown that combining the analytical results with CFD works quite well across different spray geometries. Upon the implementation of an effective primary atomization module, coarse-grid, time-averaged spray flow simulations with minimal computational load are

realized without having to resolve the detailed drop formation processes. Thus far, the computational protocol has been applied and validated for pressure-atomized sprays without and with swirl, and liquid jets in cross-flow. In principle, this methodology can be adapted for any spray geometry, as we will demonstrate in this work for air-assisted flat sprays.

Computational Procedure

This method composes of resolving the continuous liquid-gas mixture prior to atomization followed by dispersed phase particle tracking, as discussed in Section 5.1. To furnish the initial drop sizes in the dispersed phase algorithm, Eq. (3.11) is facilitated as the primary atomization module, which includes the effect of the gas motion. In the simulation, steady-state VoF for the liquid-gas mixture is performed to resolve both the liquid and gas velocities. It is implemented with the assumption that the liquid and gas phases are completely mixed upon exiting the nozzle, based on the Everloy ⅜ inch KSAME 5395 flat spray air-assist nozzle. Hence, a single representative fluid is injected into quiescent air. The material properties of the representative fluid are volume averaged and computed based on the air-water volume ratio provided by the spray nozzle manufacturer.

An inlet velocity profile is made, given the spray angle assigned by the manufacturer. The initial velocity is set at the nozzle exit plane as a top-hat profile with turbulent boundary layers at the walls, adjusted to match the observed spray angle and total fluid volumetric flow rate. As we can see in the results, this approach produces viable results, while bypassing time-consuming simulations of internal injector flows.

Two separate air inlet pressures with the same water flow rate are applied. The implemented conditions are outlined in Table 5.1.

Table 5.1 Test conditions

	Water Flow Rate [L/min]	Air Pressure [bar]	Spray Angle [°]	Nozzle Stand-off [mm]	Air-Water Volume Ratio	Plate Temperature [K]
Case 1	6.0	0.5	90	250	25.0	1500
Case 2	6.0	1.5	90	250	92.0	1500

(a)

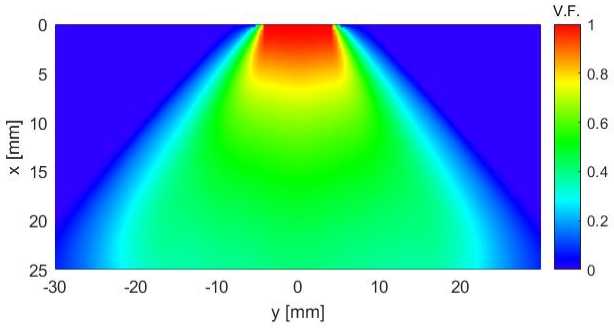

(b)

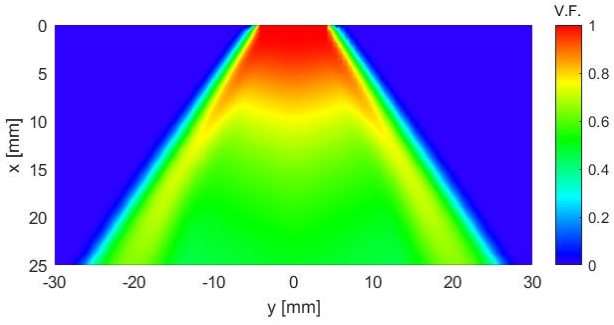

Fig. 5.16 Injected liquid-gas mixture volume fraction near injector exit for air-assist flat spray. The (a) and (b) correspond to inlet air pressure of 0.5 bar from Case 1, and 1.5 bar from Case 2, respectively

Reynolds-averaged Navier-Stokes with two-equation viscous modeling is applied to account for the turbulence in the spray field. Thus, computational requirements are no more than those needed for running k-ε types of turbulence models; in typical studies of detailed spray flows, they involve high temporal and spatial resolutions to capture the evolution of the liquid-gas interface, resulting in two- to three orders of magnitude increase in computing time and power. The resulting VoF is shown as the contour of the liquid-gas mixture trajectory in Fig. 5.16.

The atomization criterion is then applied by examining the centerline velocity and axial velocity gradient in Fig. 5.17. The location downstream where the axial velocity gradient is at the maximum marks the primary atomization plane. Accordingly, the nozzle exit plane is set as the one for both Case 1 and Case 2. Considering that the nozzle has an internal liquid-gas mixing chamber, and since the air-water volume ratio is relatively high in both cases, the primary atomization plane would logically reside at the nozzle exit.

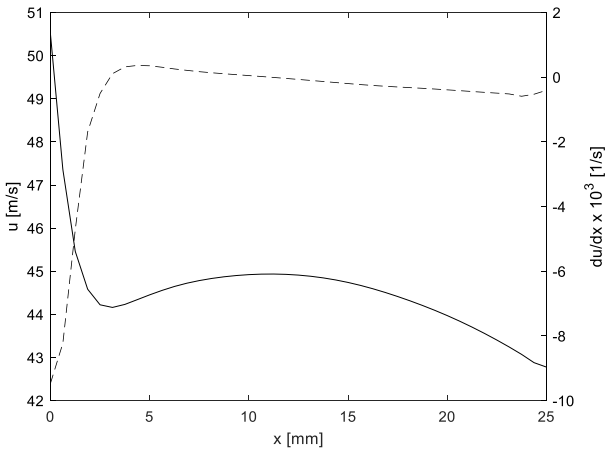

Fig. 5.17 Liquid-gas mixture centerline velocity as solid line, and axial velocity gradient as broken line for air-assist flat spray. They are plotted as a function of downstream position of the nozzle for Case 1.

The liquid and gas phase velocity components are extracted from the primary atomization plane. The mixture velocity is separated into liquid and gas phase velocities via local mass and momentum balance. This function is performed internally within the Fluent CFD, and since the data extraction is local no energy constraints are needed. The liquid and gas phase velocities are input into Eq. (3.11) to furnish the initial drop size.

Then, the initial drop sizes and local mixture velocity components are input into injection files for Lagrangian discrete particle simulations. A total of 375 point injections are defined in a 2D plane, encompassing the nozzle exit plane, and particles are released at the local mixture velocity. The injected particle mass flow rates are computed on a velocity-weighted average basis, so that the entire injected liquid mass flow rate matches the sum of individual particle mass flow rates. The droplets are tracked as Lagrangian point particles in air using the discrete-phase model, DPM in ANSYS Fluent as seen in Fig. 5.18.

In summary, the current computational protocol involves computing the continuous liquid-phase motion first, then from the liquid velocity data, calculating the initial drop size analytically with Eq. (3.11), and lastly tracking the resultant droplet motion. As noted above, it is advantageous in combining the computed momentum field with a theoretical solution of derived drop size. Plus, the performance has been demonstrated well in various spray geometries [54,55,76].

Results and Discussion

In this context, the application of the air-assist spray is considered. Spray flow visualization is made via particle visualization colored by normalized drop number

density shown in Fig. 5.18. The drop number density is normalized by the volume average drop number density to display relative concentrations of droplets. The droplet trajectories with spreading, and their overall figures in atomization near the injector exit, resemble closely experimental images [70,73].

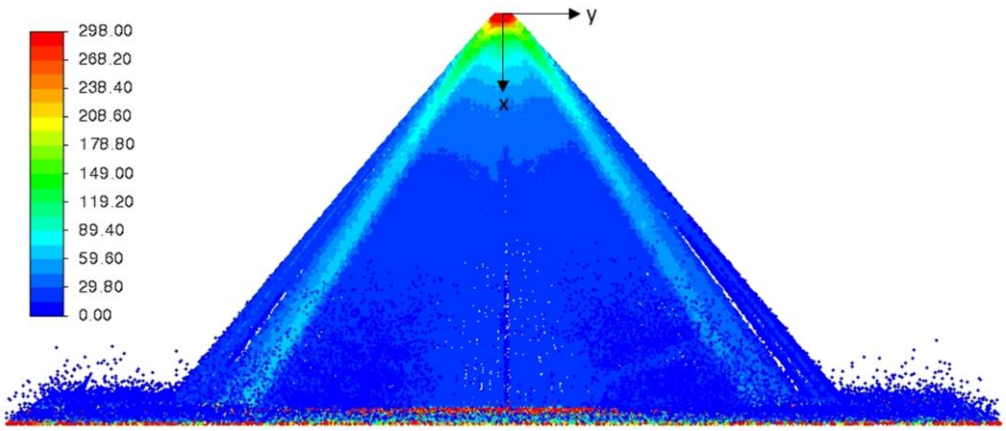

Fig. 5.18 Particle tracks for air-assist flat spray, colored by normalized number density to highlight relative concentrations of droplets for Case 2

The quantitative comparisons for the Case 1 and Case 2 to experimental data from Chabicovsky et al. [71] are made in Fig. 5.19 and Fig. 5.20 respectively. The drop size and velocities were measured using a dual-pulsed high-speed camera setup [71]. The experimental set-up was limited to particles with diameters greater than 5μm and a reasonable dynamic range of 1:100 [77].

First, the averaged droplet velocity magnitudes for each case are compared to the corresponding data in Fig. 5.19(a) and Fig. 5.20(a). For Case 1 of Fig. 5.19(a), the trend of increased particle momentum between 50 and 100mm from the nozzle center is captured in the simulations, with some overestimation of about 7 to 12%. For Case 2 of

Fig. 5.20(a), the droplet velocity profile is relatively flat, 15m/s at the centerline and 20m/s at the periphery in the simulation results, and 16 to 20m/s in the experimental data. Although the trend is reversed, the range of droplet velocities is within the experimental error range. The discrepancies in the droplet velocity magnitudes are likely a statistical error both in the measurements and simulations. In addition to that, there might be some initial input differences from the VoF. Nonetheless, the above computational procedure still returns agreeable results.

(a)

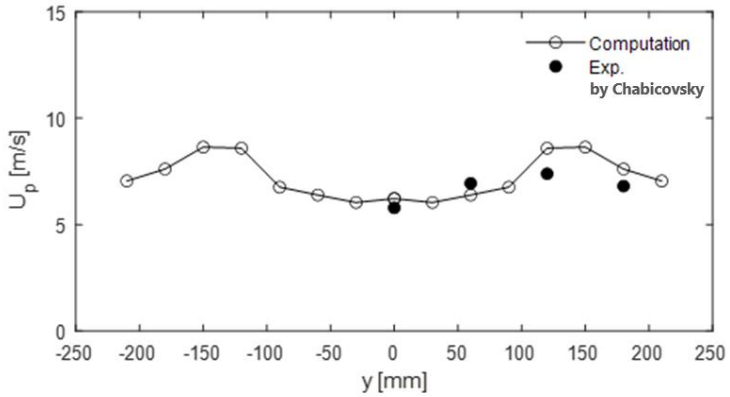

(b)

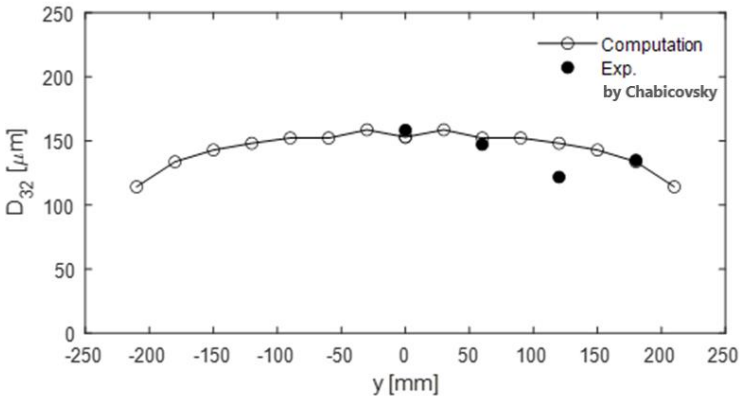

Fig. 5.19 Comparison of averaged (a) particle velocity, and (b) D_{32}, for air-assist flat spray with Case 1. The computation is averaged within 100 × 30mm regions centered at the y-location along the length of the plate at 250mm downstream of the nozzle. The data from Chabicovsky et al. [71]

(a)

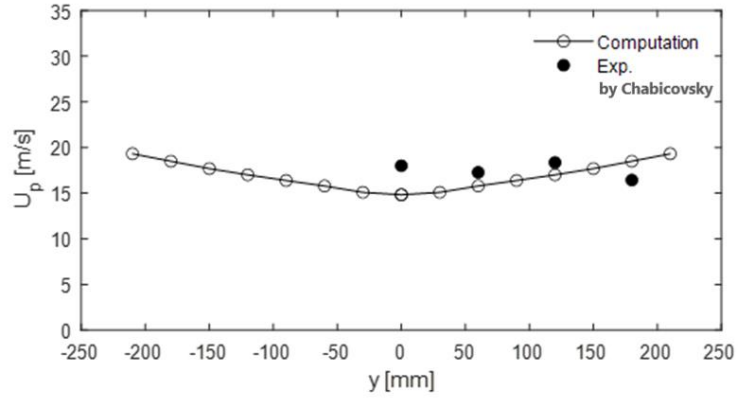

(b)

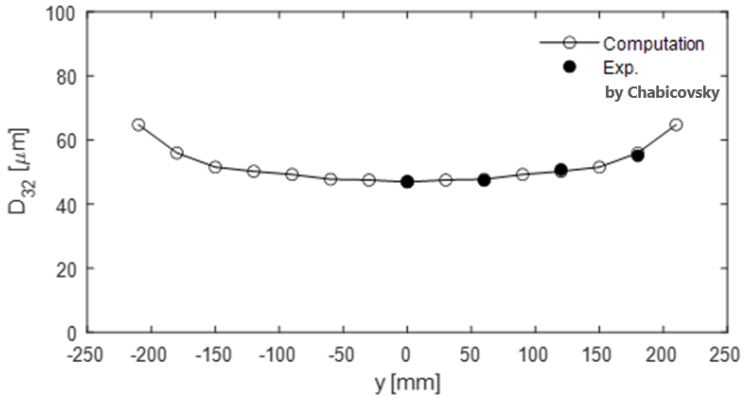

Fig. 5.20 Comparison of averaged (a) particle velocity and, (b) D_{32}, for air-assist flat spray with Case 2. The computation is averaged within 100 × 30mm regions centered at the y-location along the length of the plate at 250mm downstream of the nozzle. The data from Chabicovsky et al. [71]

Next, the averaged Sauter Mean Diameters, i.e., SMD or D_{32}, are studied in comparison as a function of distance from the center of the spray; relative to the y-direction as marked in Fig. 5.18. This returns quite good agreement with experimental data for both Case 1 and Case 2, as found in Fig. 5.19(b) and Fig. 5.20(b), with a maximum deviation of 16%; but that is only at one y-location and probable experimental deviation. The only deviatoric data point is at y = 120mm for Case 1, which relatively

drops off from other points, suggesting an anomaly in the measurement statistics. Except for this data point, the averaged SMD of computation matches well with the experimental data. In addition, the averaged SMD in Case 1 shows the largest one near the center of the spray and decreases slightly as the distance from the centerline increases. For Case 2, the opposite trend is correctly captured in the simulation, where the averaged SMD at the center of the spray is the smallest one and increases as the distance from the centerline increases.

There are atomization models that produce drop size data for specific injectors with a narrow range of test conditions [56]. On the contrary, the current primary atomization module is versatile since it is based on conservation principles applicable to various injector geometries at practical Reynolds and Weber numbers. Accordingly, the results of the above validation corroborate it.

5.3 Jets on the Sea Surface Plumes

Background

One of the places where cross-flow spray atomization has been observed is the sea surface. There is an increasing interest in dynamic phenomena over the sea surface and its interactions with the atmosphere, e.g., exchanges of momentum, species, and heat [78,79]. Since climate change has been a global issue, critical research on the sea surface sprays is conducted by scholars in seeking the causal relationship, essentially unveiling the formation process of the sea spray. Here we try to apply our theoretical methods in the calculations of drop size distribution and compare it with experimental data. In this way, we corroborate our theory as viable in various spray fields. Our simulation is

modeled based on the experiment of sea spray spume droplets by Vernon et al. [80]. The spume drops are generated from the crest of steep waves when wind shear is strong enough to tear it [81]. Therefore, analyses are attempted considering it as the case of liquid jets in the cross-flowing of gas.

Simulation Domain

The three conditions of wind speeds blowing on the sea surfaces are simulated in a two-dimensional computational domain, U_{10} = 31.3, 41.2, and 47.1m/s. The wind is input from the left on the stagnant water surface, and then resulting local velocities are extracted from the sampling positions at various coordinates, x = 0.4, 0.7, 1m, y = 0.46 ~ 0.51m, between the interface region of water and air. The control volume is set as x = 0 ~ 6m, y = 0.4 ~ 0.6m, where the upper region on the free surface seen in Fig. 5.21.

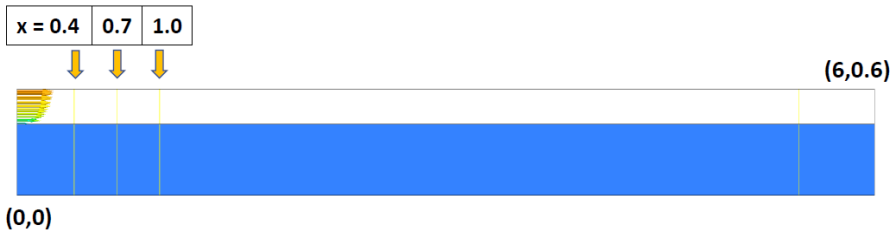

Fig. 5.21 Simulation domain for jets on sea surface plumes

Boundary Condition

The wind velocity profile to input is referred to well-known ‘law of the wall’ by which it renders a logarithmic velocity profile so that pertinent drag effect on the surface can be reflected.

$$u_{in} = u_\tau \left(\frac{1}{k} \ln \frac{y}{y_0} \right) \quad \text{Eq. (5.1)}$$

Eq. (5.1) is for the incoming wind velocity profiles at the boundary. This equation comes from bulk aerodynamic drag relations, $\rho {u_\tau}^2 = C_{DN} \rho {U_R}^2$, where u_τ as friction velocity, C_{DN} as neutral drag coefficient, and U_R as velocity at reference height. In the equations the requiring parameters, such as u_τ, and y_0 as roughness length, are used from the experimental estimation. For example, y_0 is calculated from the given estimations of U_{10}, u_τ, and C_{DN} from the reference paper of Vernon et al. [80]. The k in Eq. (5.1) is von Kármán constant.

Table 5.2 is the parameters implemented on the boundary conditions. It is foreseeable that the boundary layer thickness forming on the water surface should be large due to non-negligible roughness length from undulations, therefore turbulent length scale is set up as sufficiently high as 4m for the simulations.

Table 5.2 Boundary condition parameters

U_{10} [ms^{-1}]	C_{DN}	u_τ [ms^{-1}]	y_0 [m]
31.3	1.7×10^{-3}	1.29	6.0×10^{-4}
41.2	2.3×10^{-3}	1.98	2.4×10^{-3}
47.1	2.4×10^{-3}	2.33	2.8×10^{-3}

Fig. 5.22 depicts different aspects of the undulations on the surface subjecting to the varied U_{10}. It characterizes an increase in acuate spots with more strong velocity blowing on the surface. These can be regarded as sharpened plumes of wave crests or

ripples induced by the high wind momentum. As transferring wind momentum more to the still liquid, the plumes evolve their appearance from diffusive to perturbed.

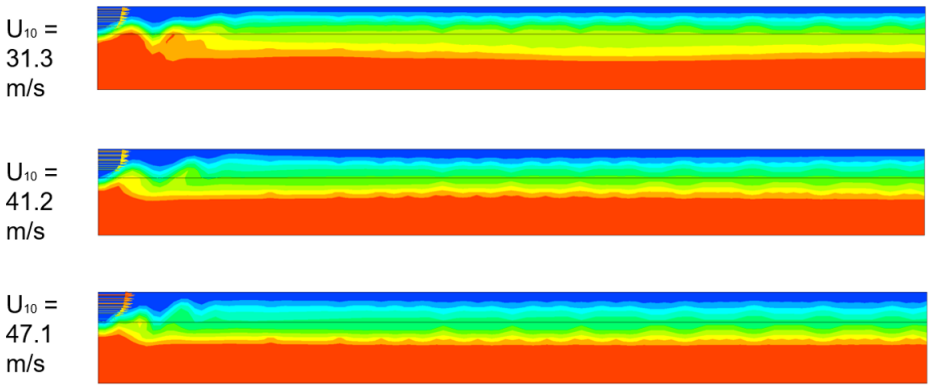

Fig. 5.22 Comparison of the sea surface undulations in various wind speed

Simulation Setup

ANSYS-Fluent is used for the CFD simulation. In the CFD setup, the turbulent k-ε model with VoF multiphase of water and air is taken. Discretization schemes are second-order upwind and first-order upwind for momentum and k-ε equations respectively. The pressure solver is v-cycle with PRESTO, and SIMPLE is in coupling pressure-velocity while correcting continuity. For the volume fraction Compressive scheme is used. The structured quadrilateral mesh of 0.1m × 0.1m is constructed at first, and then gets adapted refining the mesh depending on the volume fraction while solving proceeds, which technique is the equipped function usable in CFD. Not a significant mesh quality problem was reported.

Both transient and steady-state solvers were tried in order to compare what different figures might be drawn in applying the spray simulation. During the transient,

first-order implicit time integration was used. In the transient-solver, the time step size was 0.01 ~ 0.001s for about 5min long so that it could give a quasi-steady state solution. And for the steady-state solver, iterations continued until it reaches the convergence limits. In comparison for both solvers, it turned out to be no noticeable differences overall, having the results by steady-state solver ascertained. Therefore, the simulation results by the steady-state solver are represented here in the analyses.

Implicit Variables

When it comes to the mass conservation for the liquid drops in our mathematical derivations as Eq. (3.1), an inevitable issue arises and hinders our conservation theory from being fulfilled in a normal way. Specifically, the free surface that initially stagnant liquid evolves gradually into dynamic motions owing to incoming gas momentum and interactions with it, resulting in the creation of liquid drops from zero liquid mass flux, within the control volume. This contradiction is compensated by a global variable, which the estimate is obtained by area averaging of the local variable of interest, over the control volume. This means the global estimate should be evaluated implicitly through the resulting local values only after the simulations. How the global estimate is set and enforced into our theoretical formalism would be dependent on the situation. In general liquid injection circumstances, the task does not necessarily a required one. In this study, we use the global estimates of u_{inj}, u_{in}, and turbulent kinetic energy.

Results and Discussion

Fig. 5.23 are local velocities at three different horizontal positions of x = 0.4, 0.7, and 1m for the liquid and gas phase separately when U_{10} = 41.2m/s. In the liquid velocity profiles of Fig. 5.23(b), a drastic changes within the interface region y = 0.4 ~ 0.5 is apparent, especially for x = 0.4m. This observation implies strong shear stress exists and causes spray atomization. In addition to choosing that horizontal position at x = 0.4m as a pertinent sampling location, specific vertical coordinates ranging in y = 0.46 ~ 0.51m are taken in extracting the local velocities, recalling that still surface level is y = 0.4m. These sampling coordinates are corresponding to the experimental measurement carried out, in which they measured at the height of 8 ~ 9.5cm above the still surface to estimate all parameters involved in droplet size distribution.

For the gas velocity profiles of Fig. 5.23(a), inconsiderable differences are made among them. Within the interface region y = 0.4 ~ 0.5, the steep gas velocity gradient is also found, likewise in the liquid velocity profile of Fig. 5.23(b).

Consequently, Fig. 5.23 indicates that the momentum transfer from gas to liquid is effectively reflected in the velocity profiles with x = 0.4m, while farther horizontal locations are not eligible. It is natural since the nearest sampling position downstream from the initiated wind momentum is subjected to a strong influence of it, in CFD simulations. Elsewhere far downstream from the initial boundary conditions of wind, more diffusive or dissipated dynamics for the wind momentum, and therefore relatively less momentum transfer to the liquid phase would result. Conversely, it means that in the nearest downstream distance x = 0.4m, less of the gas momentum is lost to transfer to the liquid so that the liquid can add more momentum, as shown in Fig. 5.23(b).

Therefore, it convinces us of choosing the sampling coordinates, x = 0.4, y = 0.46 ~ 0.51m, as the primary atomization region satisfying the primary atomization criterion, i.e., liquid velocity gradient. And it requires the different vertical coordinates to choose for the sampling with respect to the initiated gas momentum of U_{10}, since the liquid crests positioning and height vary with U_{10}. For example, in the case of U_{10} = 41.2m/s, the y-coordinates of 0.49, 0.5, and 0.51m are chosen for the particular sampling positions.

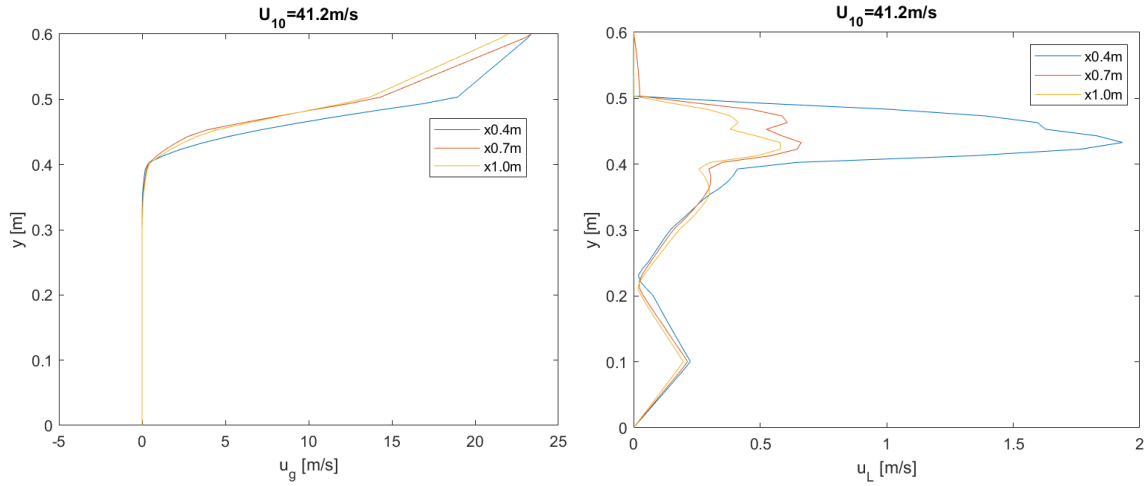

(a) (b)

Fig. 5.23 The velocity profiles in the simulation of jets on the sea surface plumes; (a) for gas phase, and (b) for liquid phase

In virtue of the analytic expression of Eq. (3.11), a representative drop size at a specific coordinate can be calculated from local velocity profiles, recalling that u_{inj}, u_{in}, u_L, $and\ u_g$ are the main variables in the cross-flow spray atomization. On the other hand, it is desirable to construct a drop size distribution rather than a single representative value, which is a better suitable and recognizable measure to characterize a myriad of

generated droplets. For instance, a gaussian distribution is applied to give a statistical variation on the mean local gas velocity with its turbulent kinetic energy as Fig. 5.24(a). The turbulent kinetic energy is obtained in a global manner as mentioned in the previous context. Having the truncated gaussian distribution function with a Z-standard score of 1.75 gives a confidence interval of 96% within a finite range of u_g, and the resulting distribution is shown separately with different vertical positions in Fig. 5.24(a).

Within the range of y = 0.46 ~ 0.51m, the three different vertical positions at y_1, y_2, and y_3 are chosen. These are where the velocity values from the simulation are extracted to make the gaussian distributions of velocity and drop size, as shown in Fig. 5.24(a) and Fig. 5.24(b). Fig. 5.24(b) is the conversion to the drop size probability density function, PDF, from the corresponding velocity PDF of Fig. 5.24(a). Both PDFs are area-normalized distribution to preserve the formal definition, i.e., area = probability.

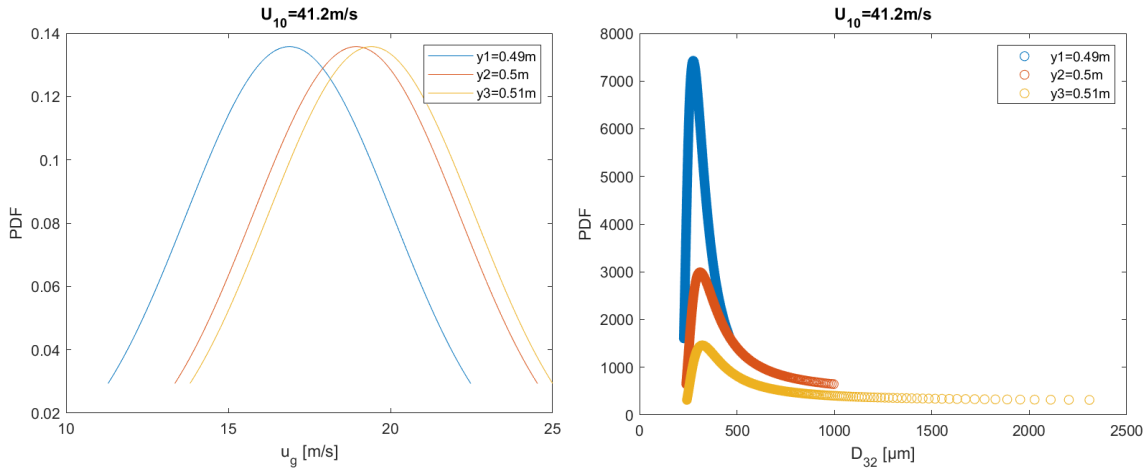

(a) (b)

Fig. 5.24 The normal distributions of velocity and drop size, from simulation of jets on the sea surface plumes; (a) for gas velocity, and (b) for drop size

Further manipulation is devised with Fig. 5.24(b) such that it is discretized in 19 bins logarithmically, which is consistent with the way of experimental treatment on counting droplets, ensuring that the category of drop sizes is also obeyed. In turn, it summed up all three PDFs covering the same bins to make a single combined distribution function. For example, $f(D) = f_1(D) + f_2(D) + f_3(D)$ where $D_i \leq D < D_{i+1}$. After this process, re-normalization is required for the same reason as previously stated, and the resulting distribution shows in Fig. 5.25.

While the combined PDF would suffice to depict the derived drop size distribution as seen in Fig. 5.25, for the purpose of comparison with the experimental data, which is expressed in the spectral concentration for the distribution, additional normalization by the total concentration on the combined PDF is taken. Those results are found in Fig. 5.26, Fig. 5.27, and Fig. 5.28.

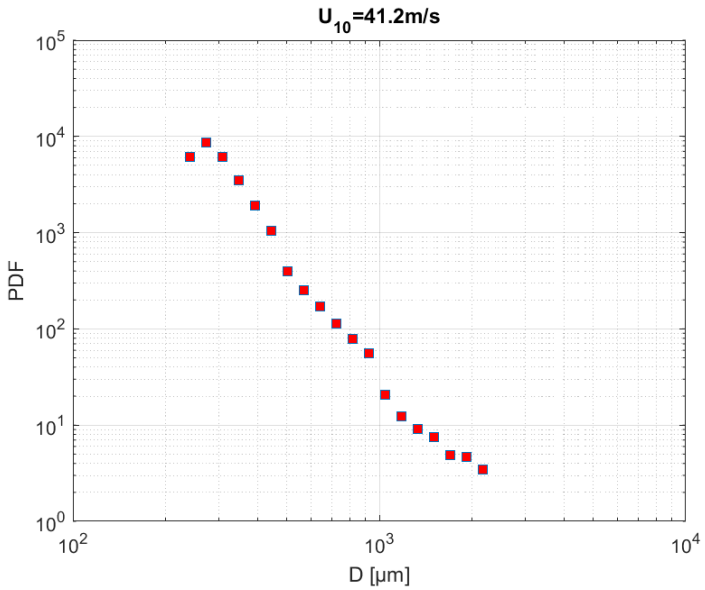

Fig. 5.25 Discrete probability distribution of drop size in the sea spray simulation

Fig. 5.26, Fig. 5.27, and Fig. 5.28 are the calculated distributions, and compared with the experimental data [80] for three different incoming wind velocities, U_{10} = 31.3, 41.2, and 47.1m/s respectively. It manifests that our calculations are in good agreement with them. It is noted that the more strong incoming wind velocity yields higher and more intensive distributions toward small drop ranges. This is deducible in that for the gas-driven cross-flow process, the strong gas momentum plays an important role in spray atomization producing many smaller droplets. The calculated distribution deviates slightly from the experimentally measured one, for the highest wind velocity of Fig. 5.28. Supposedly, in practical circumstances of experimental measurements, energy loss is inevitable whereas the CFD domains obey energy balance. As a result, the deficit energy causes less contribution to the breakup processes, so it comes to broadening its range towards more large drop sizes in measurement.

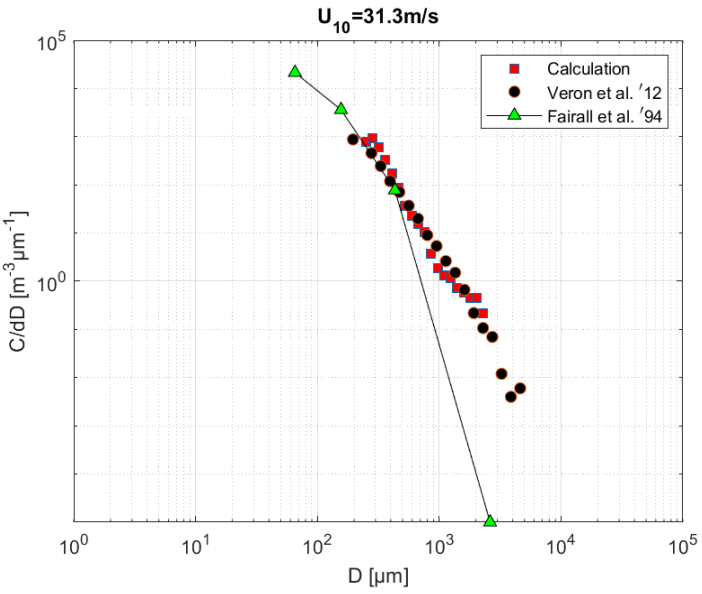

Fig. 5.26 Comparison of drop size distributions for U_{10} = 31.3m/s

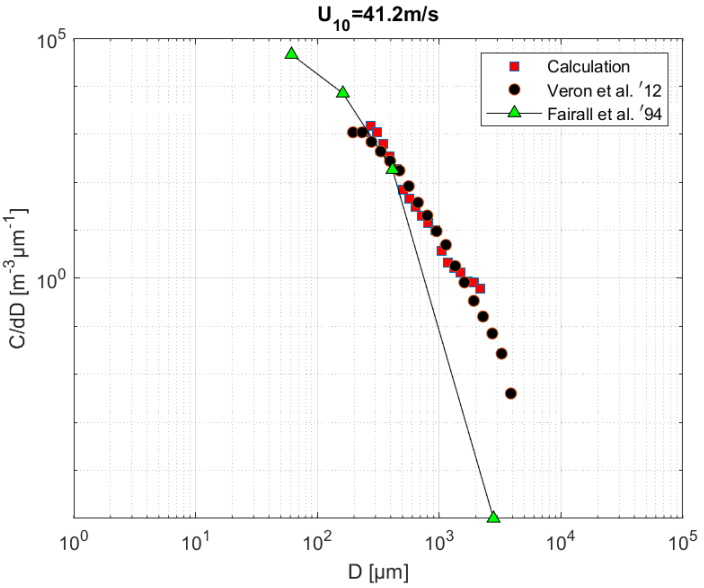

Fig. 5.27 Comparison of drop size distributions for U_{10} = 41.2 m/s

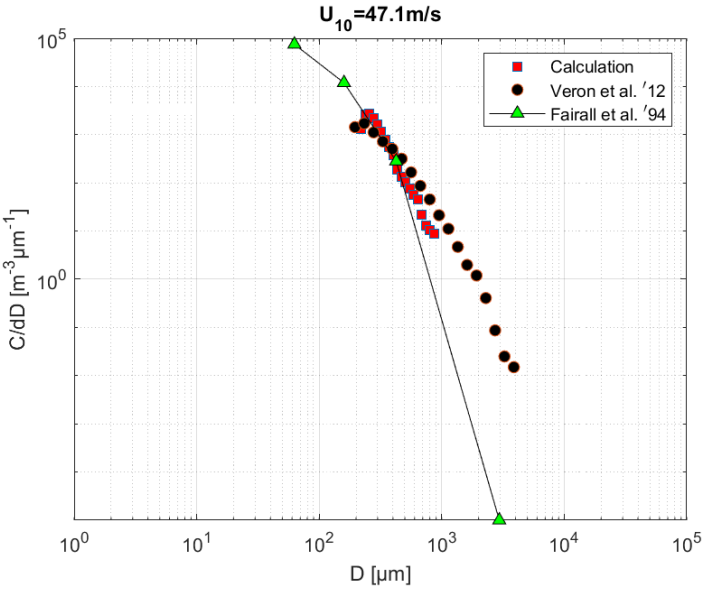

Fig. 5.28 Comparison of drop size distributions for U_{10} = 47.1 m/s

Overall, our method performs well while demanding relatively a low computational cost. In this regard, our method based on conservation principles with the

CFD atomization module, exhibits a promising potential to use as an adaptable approach, as its versatility has been demonstrated in a variety of spray fields.

5.4 Liquid Jets in Sydney-Burner Flows

Background

The idea of making a circumstance where liquid fuel droplets are in more diluted conditions after fuel spray breakup processes, has been of interest in combustion research [82–85]. The combustion in such a condition is observed to have more enhanced performance in effectiveness as fuel droplets are well mixed with ambient oxygen. It benefits in that this prolongs the combustion duration as well as reduces the products of imperfect combustion and unburned fuel. In the usual way of sprays, however, the configurations of resultant droplets are highly sporadic and partially dense.

On the other hand, a specially devised apparatus, by the name of Sydney-Burner, has been proposed by a research group in Canada to improve the performance of conventional sprays. It is characterized by the recession for the location of liquid injection within the pipe where co-flowing air is being supplied. This induces the liquid breakup inside of the pipe long enough, while both fluids are passing through as distance as the recession length before exiting into the atmosphere. The state of diluted droplets was proven in the flame stability experiment, in which the recessed fuel injection was set up [85].

In this context, we apply our method with the recessed spray configuration, then compare the results with the experimental observation. Particularly, the non-reacting fuel spray is considered. In the case of reacting fuel spray, the material composition supplied

through the pilot is manipulated under stoichiometric conditions, so that serves as a reactant on the fuel, e.g., premixed hydrogen, acetylene, and air [85]. However, our theory does not deal with factors coming from combustion that might have an impact on the liquid breakup mechanism, such as chemical reactions or evaporation in thermodynamics. Therefore, we focus on non-flammable spray in the Sydney-Burner. Our procedure including the D_{32} equation is applied to the type of recessed spray under the non-reacting condition to investigate its applicability, so that it can promote its usability beyond ordinary geometric configurations of sprays.

CFD Simulation Setup

The simulation of the Sydney-Burner is modeled based on the serial experimental works of Masri et al. [82–85]. The multiphase VoF, i.e., Volume-of-Fluid, is used and the resulting velocity field is shown in both Fig. 5.29 and Fig. 5.30. It is the type of liquid jets in co-axial flowing of gas, if we place it under the category that used for the theoretic analysis in previous chapters. Therefore, an axisymmetric computation domain suffices to deploy. Acetone and air are used as liquid fuel, and both co-flowing gas and supplementary gas issuing through the pilot. Acetone was injected with a diameter of 0.686mm needle, d_{inj} = 0.686mm, which resides within the coaxial air pipe with a diameter of 10mm, d_{in} (= d) = 10mm. From the jet exit plane at x/d = 0, two distant lengths of the recession were initiated with Lr = 25mm and Lr = 80mm before running the simulation. These configurations in the simulation domain are shown in Fig. 5.29 and Fig. 5.30 respectively, including the resulting velocity fields. The simulation is set up, such as the Shear Stress Transport k-ω turbulence model with VoF multiphase in steady

state, and initial velocities of u_{inj} = 2.58m/s for acetone, u_{in} = 48m/s for co-flowing air, and 4.5m/s for air issuing from the pilot.

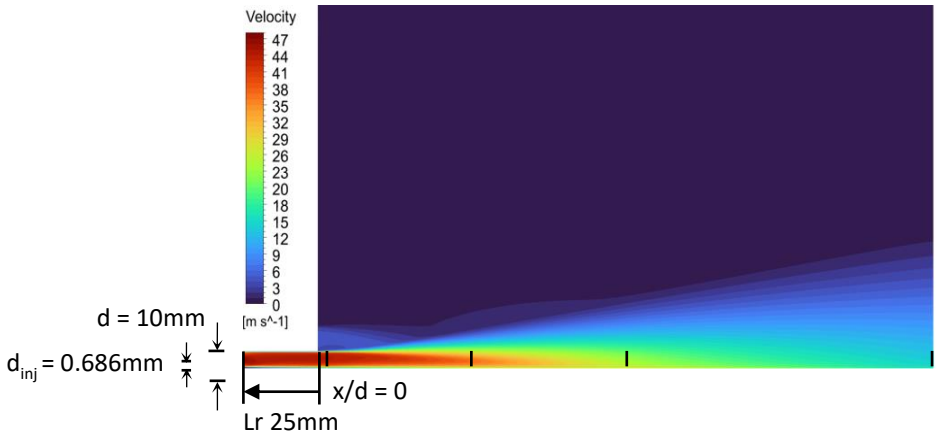

Fig. 5.29 Simulation domain including velocity field, for liquid jets in Sydney-Burner flows with Lr = 25mm. The spray exit plane at x/d = 0 is marked

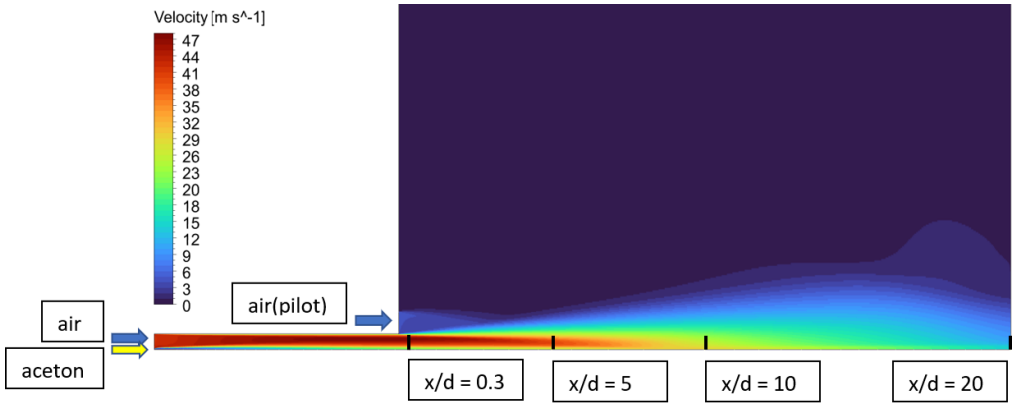

Fig. 5.30 Simulation domain including velocity field, for liquid jets in Sydney-Burner flows with Lr = 80mm. The sampling positions of x/d = 0.3, 5, 10, and 20 are marked

Results and Discussion

From the VoF simulation, the velocity profiles at the specific locations are obtained with x/d = 0.3, 5, 10, and 20, for both cases of Lr = 25mm and Lr = 80mm. And the separate profiles are found in Fig. 5.31 and Fig. 5.32 respectively. Both figures indicate the impending dynamics of turbulent mixing near the exit plane induced by the significant velocity gradient in the jet flow. Especially, more vigorous mixing is presumable in the interface between liquid and gas of r/d = 0.2 ~ 0.4, as trying to neutralize the velocity gradient initiated by the different forcing velocities of u_{inj} and u_{in}. In addition, imposing a far recessed distance led to enhanced inner-mixing in the core region prior to exit, making velocity in the core further neutralized. For example, with Lr = 80mm, the more heightened velocity than with Lr = 25mm is found for r/d = 0 ~ 0.4 where liquid fuel at low speed as u_{inj} is loaded.

The dynamic mixing is induced by the turbulence kinetic energy of contiguous co-flowing air. Due to the high air momentum and wall shear stress within the pipe, turbulent mixing is aroused, and extension in the recessed distance would result in accumulations of the intensively suppressed stress. Consequently, liquid fuel is influenced by the co-flowing air and undergoes a destructive breakup process while passing through turbulent air flows within the air pipe. Then, the confined and accumulated turbulent stress is discharged after the exit plane x/d = 0, hence its mixing scales get expanded and also the dynamics get wider. The dilute droplets can be made during this outer-mixing. After all the inner- and outer-mixing, the increased centerline velocities for Lr = 80mm at all x/d are made, which explain the enhanced mixing momentum than that for Lr = 25, from both the experiment and simulation.

In experimental data, this aspect is noticeable far up to the distance of x/d = 5, in which the centerline velocity is enhanced up to 10m/s from that of Lr = 25mm. Accordingly, the corresponding Vof results appear similarly as well in this respect. On the other hand, diffused and dissipated profiles after x/d = 10 are apparent in both results of the experiment and simulation. Therefore, in the DPM simulation, we only consider the case of Lr = 80mm, and designate a primary atomization plane at x/d = 5 to initiate particle release with DPM. Especially this location is where the most accordance comes between the experiment and simulation results of VoF.

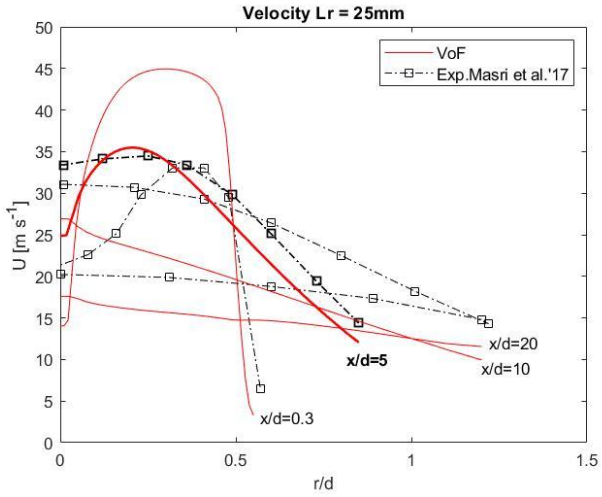

Fig. 5.31 The comparison of velocity profiles, for liquid jets in Sydney-Burner flows with Lr = 25mm. The experimental data from [85]

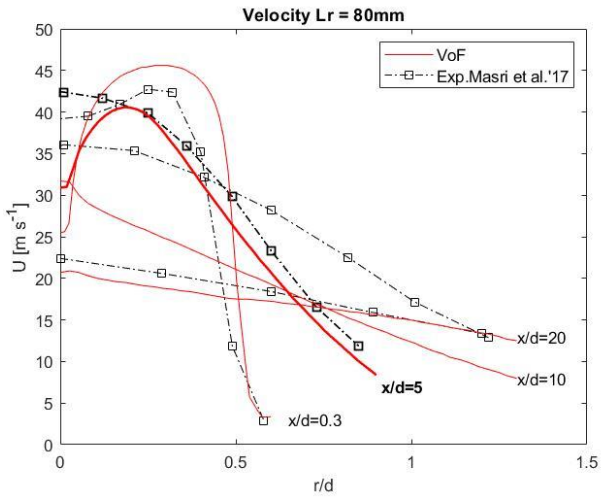

Fig. 5.32 The comparison of velocity profiles, for liquid jets in Sydney-Burner flows with Lr = 80mm. The experimental data from [85]

The DPM, i.e., Discrete Phase Model, is applied on the velocity field after the VoF simulation with continuous phase is completed. Fig. 5.33 shows the derived drop sizes from the calculation of the D_{32} equation in Eq. (3.11) using the updated velocity field after the DPM simulation. The updated velocity field is the result of being influenced by the drag force induced by the particles released at x/d = 5. The Navier-Stokes equations in which a drag force term is added launch a numerical solving under the steady-state condition, starting from the previously solved velocity field in the continuous phase, hence, it subsequently updates the velocity field on the discrete phase.

Fig. 5.33 compares the calculated drop size with corresponding experimental observations [82,83] at the same sampling locations. Because the measurements in drop sizes with respect to the radial coordinates for Lr = 80mm are not available, the second best references in which experimental data for Lr = 60mm [83] and 75mm [82] were available are used as an alternative in comparison to the derived drop sizes seen Fig. 5.33.

There seems to exist some extent of deviations with an approximate margin of error of 5μm for all the sampling locations of x/d. On the other hand, the trend between both is consistent at each sampling locations; drop size in radial direction decreases for x/d = 5, whereas increases for x/d = 10 and 20, in both calculation and experimental data.

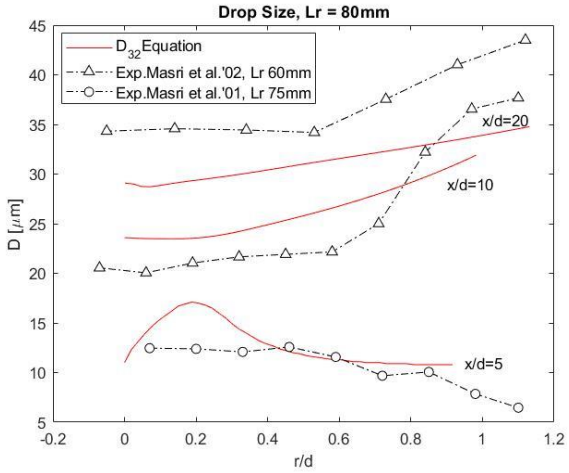

Fig. 5.33 The comparison of drop sizes, for liquid jets in Sydney-Burner flows with Lr = 80mm. The experimental data from [82,83]

In the calculated D_{32} of Fig. 5.33, the individual tendencies are differently found, for the drop sizes in a radial direction at separate axial locations of x/d. To be specific, it gets a decrease as farther from r/d = 0.2 for x/d = 5, on the contrary for x/d = 10 and 20, both get an increase. Plus, it seems constant in r/d = 0 ~ 0.2 for both x/d = 10 and 20, whereas it decreases for x/d = 5 as closer to the centerline. Those spatially varied tendencies also differ from that of the velocity profiles in Fig. 5.32. Hence, this implies that it may be difficult to deduce the relationship between drop size and velocity merely from their portrayal in the plot with bare eyes. But rather, it could be achievable by

coherent analyses attributed to spray dynamics with principle laws, likewise D_{32} equations.

In this regard, a prediction to drop sizes with different sprays has been a hurdle while giving highly sensitive and case-dependent results. This diluted spray configuration is also not exceptional but finds local dependency, e.g., axial and radial direction, in which dynamics and breakup mechanisms have different aspects. Due to the obscurity, a correlation on a fitting curve with a few modifiable coefficients was typically reported from case to case, without revealing a unified framework. By the way, making use of conservation laws in our theory renders a more reasonable framework in that it is capable of covering a wide range of spray methodologies.

Fig. 5.34 DPM simulation including particle tracking and velocity field, for liquid jets in Sydney-Burner flows with Lr = 80mm

Fig. 5.34 shows particle tracking after momentum exchange is completed between the discrete particles and continuous mixture phase, i.e., jet of liquid acetone and airflow. The particles were released at x/d = 5 with Lr = 80mm in the steady-state velocity field

with DPM. To make the picture more realistic, a turbulent dispersion effect is included with a stochastic tracking option. Else physical modeling, such as collision, coalescence, or breakup effect, is not included in this simulation. In this way, it excludes artificial changes in drop sizes but preserves the genuine drop sizes of primary atomization which are derived from our theory with the D_{32} equation. Without having a secondary atomization effect, a discrepancy from the final drop size distributions would exist as we will find in Fig. 5.35.

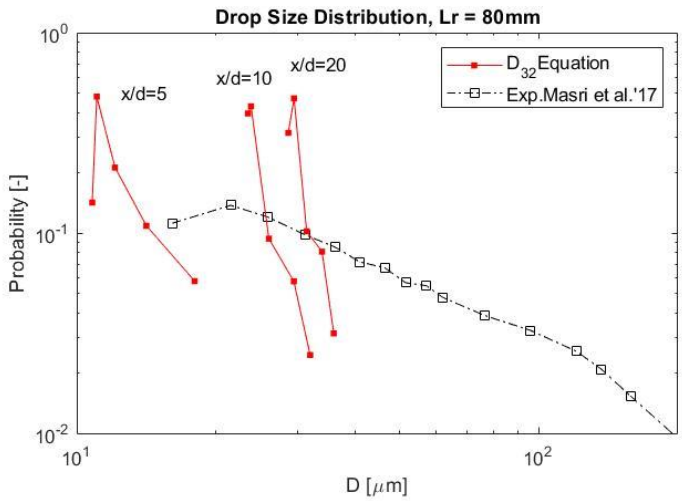

Fig. 5.35 Drop size distribution for liquid jets in Sydney-Burner flows with Lr = 80mm. The experimental data from [85]

Fig. 5.35 shows the derived drop size distribution for Lr = 80mm in comparison to the experimental data [85]. The portion of the probability distributions less than 0.01 in the experimental data is omitted for the optimal plot. According to the experimental observations, it reports as large as 600μm of sampled drops fall into the probability below

0.01. However, less than 1% could be negligible in the event, so we try to focus on the main portion. Another point to be mentioned is that, drop samples in the experiment were collected near the exit plane, whereas our sampling from the simulation is executed at x/d = 5, 10, and 20. Recalling the velocity profiles comparison of Fig. 5.32, the diluted state in simulation is achieved farther away from the exit plane than that in the experiment, thus we samples drop at the above three distant positions.

At each of the sampling positions along the centerline axis, equally spaced 50 radii in a radial direction are assigned. Given the total loaded liquid mass flow rate of 0.00075kg/s, it is assumed to be distributed equally to each of the annulus regions between neighboring radii. Finally, the drop number density is calculated using the derived drop size and corresponding annulus region velocities; for the calculation formula, it can be referred to the Eq. (3.6). In this way the discrete probability distribution of drop size is calculated first, then adjusted with 5 edges by which the structure of the distribution is well characterized. This can be done by grouping each probability into 4 bins; the adjusted probability distribution is obtained after normalization, and preserves add up to 1.

In Fig. 5.35, it is found that the derived distribution is more narrowed than the experimental one. Because neither extra modeling to secondary break up nor coalescence effect with DPM, are included in the current simulation, since these artificial treatments manipulate initial drop sizes, hence some discrepancy arose for the final drop size distribution between them. For the same reason, the turbulent velocity variation effect is also excluded from the results, although the variance from the mean estimates would

yield making a more dispersed drop size distribution seemingly similar to the experimental one.

Besides, with the use of this specially devised spray in Sydney-Burner, the flow dynamics are subject to the outcome of intensified turbulent mixing, driving further deviating results from ones of primary atomization, as seen in Fig. 5.35. Nonetheless, the most plausible drop size, i.e., mean drop size, is in the same order of 10^1 for both derived and measurement data; 20 ~ 30μm in data, and 10 ~ 40μm in the calculation. In the comparison among different sampling positions, it appears the closer to the exit plane, the smaller the drop size in the highest probability and the wider distribution. Therefore, it indicates that liquid breakup as near as the exit plane would make the range of resulting drop sizes broaden, a promising clue to be consistent with the experimental observations.

5.5 Chapter Summary

We have used the generalized primary atomization module in computational simulations of spray flows. The use of our quadratic formula in the simulation with basic spray configurations has been validated, under realistic Reynolds and Weber numbers; pressurized jets without and with swirl, and jets in cross-flow. On top of that, more attempts have been made in the validation with various applications, such as air-assist mist jets for cooling film, sea surface plume jets, and diluted jets in Sydney-Burner.

The computational protocol consists of four steps; 1) continuous phase simulation 2) determination of atomization criterion 3) specify initial drop size and velocity 4) dispersed droplet trajectory simulation. With the comparison to the experimental data, we have corroborated the computational protocol. Our method renders satisfying results

without having to cost substantially in numerical computation. Moreover, this protocol is easy to implement, computationally efficient, and robust in producing realistic spray flow simulations. In addition, the results are utilizable to make the drop size distribution or obtain spray contours.

Instead of relying on intensive numerical tasks, we take advantage of integrating the analytics results into CFD. This is an ideal interconnection between the use of analytic and numeric solutions. The D_{32} quadratic formula, Eq. (3.8) and Eq. (3.11), is derived from the conservation of mass and energy, and it requires liquid and gas velocity as input. VoF is quite capable of obtaining the mean velocity field, and DPM is useful for drop trajectory calculations in post-atomization. Thus, the complex details of the atomization processes at small length scales are coped with the analytic solution from the quadratic formula, resulting in a robust computational protocol for the primary atomization module.

PART II

Turbulence Theory and Inverse Solution Method for Wall-Bounded Flows

CHAPTER 6

TURBULENCE THEORY

Turbulence has been of interest yet remains a long-standing elusive problem [86,87]. In an attempt to cope with the problem, most of the work these days employ direct numerical simulations, DNS, in order to look into the details of the turbulence structure [88–98]. While these results are impressive and useful, still a general theoretical framework to unify the fluid physics of turbulence is demanding.

Some turbulence characteristics are postulated by scholars. For example, the attached eddy hypothesis [99] poses turbulent flows as a hierarchy of eddies, cumulating to the observed profiles. With a logarithmic expression for the energy scale distribution by using “eddy intensity function”, the model achieves agreement with data in the inertial region of the boundary layer [99]. Klewicski et al. [100] supported this hierarchical concept, through a mathematical analysis based on a hypothetical “test function”.

Starting from 2016, an alternative Lagrangian formalism for the Reynolds stress has been derived and presented in a series of works [101–107]. In this new perspective, if an observer moves at the local mean velocity, then the turbulence fluctuation and attendant transport can be mostly decoupled from the mean velocity, resulting in compact expressions for the Reynolds stress tensor components [104]. This decoupling results in a minimalistic but complete description of the inter-dynamics of turbulence momentum and energy, without any ad-hoc or heuristic modeling. The equation set, Eq. (6.1), Eq. (6.2), and Eq. (6.3), is an assertion made in the basic conservation principles of momentum and energy through a Lagrangian perspective, to address the turbulence problem. In addition to that, the Second Law of thermodynamics is applicable to find the uniqueness of the

turbulence structure. With the use of the Second Law in the form of the maximum entropy principle, a lognormal class of the turbulence energy spectra is obtained [105]. Those studies have been validated with either DNS or experimental data [101–107].

In this chapter, we study the turbulence formalism that has been developed and validated. It includes the origin of the turbulence structure as prescribed by the Lagrangian transport equations, and a brief exhibition of the possible solution method to the Navier-Stokes equations, and also a lognormal type of turbulence energy spectra. Although the title has limited the scope to wall-bounded flows, the results should be applicable to other types of turbulence, e.g., jet flows [103]. The work in the following sections has been published in Lee and Park [102,106] and Lee [101,103–105,107].

6.1 A New Set of Turbulence Transport Equations

To begin with, we place the Lagrangian transport of turbulence that leads to a symmetric set of gradient expressions for the Reynolds stress tensor components. From this perspective, turbulence structures in wall-bounded flows are seen to arise from an interaction among a few intuitive dynamical terms; transport, pressure, and viscous term.

A succinct picture of turbulence structure and its origin emerge, indicating a reflection of the basic physics of momentum and energy balance if placed in a specific moving coordinate frame. An iterative algorithm produces an approximate solution for the mean velocity in turbulent channel flows. Since the main features of the turbulent flow can be theoretically prescribed in this way, it enables us to reconstruct channel or boundary layer flows. Accordingly, it is validated in comparison with available data in direct numerical simulation.

The Lagrangian turbulence transport equations introduced in the precedent study are reiterated here below.

u' momentum transport:

$$\frac{d(u'v')}{dy} = -C_{11}U\frac{d(u'^2)}{dy} + C_{12}U\frac{dv'^2}{dy} + C_{13}\frac{d^2u'}{dy^2} \qquad \text{Eq. (6.1)}$$

v' momentum transport:

$$\frac{d(v'^2)}{dy} = -C_{21}U\frac{d(u'v')}{dy} + C_{22}U\frac{dv'^2}{dy} + C_{23}\frac{d^2v'}{dy^2} \qquad \text{Eq. (6.2)}$$

or alternatively,

$$\frac{d(v'^2)}{dy} = \frac{-C_{21}U\frac{d(u'v')}{dy} + C_{23}\frac{d^2v'}{dy^2}}{1 - C_{22}U}$$

u'^2 transport:

$$\frac{d(u'^3)}{dy} = -C_{31}\frac{1}{U}\frac{d(u'v'\cdot u')}{dy} + C_{32}\frac{1}{U}\frac{d(v'\cdot u'v')}{dy} + C_{33}\frac{1}{U}\left(\frac{du'}{dy}\right)^2 \qquad \text{Eq. (6.3)}$$

Note that in these equations and throughout this paper as well, we are using an abbreviated expression for the notations of turbulent variables. The expression for fluctuation variables such as u′v′ and u′^{2} are implicitly Reynolds-averaged, e.g., $\overline{u'v'}$ and $\overline{u'^2}$, and used in a concise form. Likewise, for the expression of u′ and v′ connote root mean square, u'_{rms} and v'_{rms}. These abbreviated terms are used throughout this paper.

The concepts and hypotheses contained in Eq. (6.1), Eq. (6.2), and Eq. (6.3) are described in Lee [104], and also summarized in the next context. When used in conjunction with the Reynolds-averaged Navier-Stokes equations, i.e., RANS, these turbulence transport equations fulfill the number of equations required to solve for the turbulence variables; u'^2, v'^2, $u'v'$, and U.

Examination of the terms in the Lagrangian turbulence equations illuminates the dynamics for the momentum and energy transport intuitively making sense. For example, Eq. (6.1) depicts the Reynolds shear stress of $u'v'$ as the net lateral transport of the turbulence momentum to balance out the streamwise flux, pressure, and viscous forces. Indeed, Fig. 6.1 reveals this explanation supporting our perspective. From Fig. 6.1 the result of computation with Eq. (6.1) is exemplified in the comparison with the DNS data [95] for the $u'v'$ gradient, which finds a good agreement between them. This exposes the simple Lagrangian momentum balance in conformity with our transport equations.

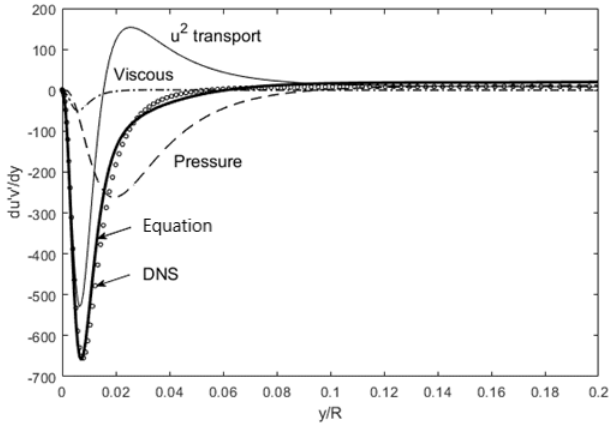

Fig. 6.1 The u' momentum budget for the Reynolds shear stress gradient. The Eq. (6.1) in comparison with DNS data from Graham et al. [95] as symbol

Basically, this approach is in contrast to the Eulerian models that requiring several layers of adjusted relationships to the mean variables. In the Lagrangian perspective, particularly the momentum conservation holds in any non-inertial coordinate frame, i.e., the Galilean invariance, and the principle of relative motion removes most of the complex coupling with the mean components, leaving bare core dynamics of the turbulence fluctuating variables. So to speak, in place of taking unproven proportionality to the mean velocities for granted, e.g., $u'v' \sim \nu_t \, dU/dy$, to relate one fluctuating component to another makes far more dynamical sense to figure out Reynolds stresses, as in our approach.

Since this formalism is relatively new, a synopsis of the logic involved is represented in Fig. 6.2 and Fig. 6.3. In a control volume moving at the local mean velocity of U and V, the effects of turbulence fluctuation components, i.e., Reynolds stress, can be isolated as depicted in Fig. 6.2. And Fig. 6.3 illustrates the displacement effect, in which d/dx is converted to the d/dy term with the mean velocity of U(y) as the proportionality constant [101–104].

(a) $\rho u'$ transport

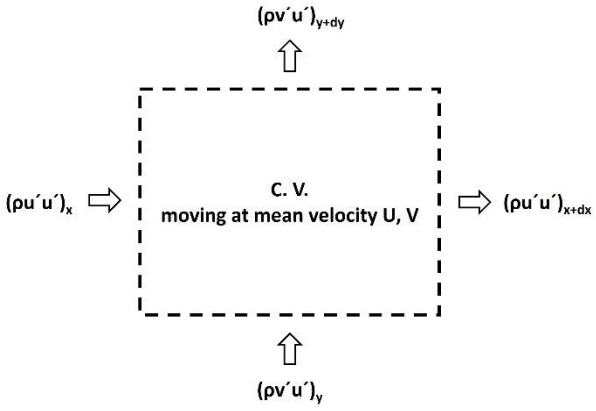

(b) $\rho v'$ transport

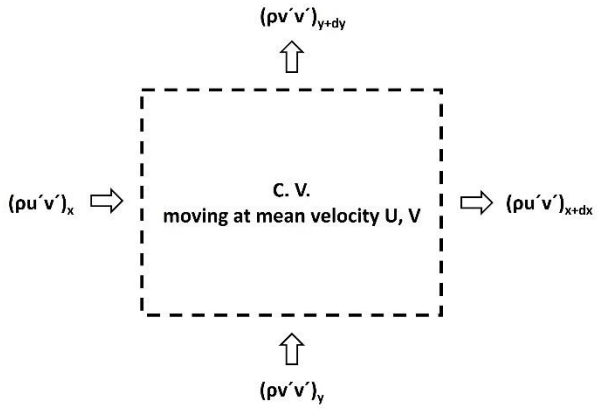

(c) $\rho u'^2$ transport

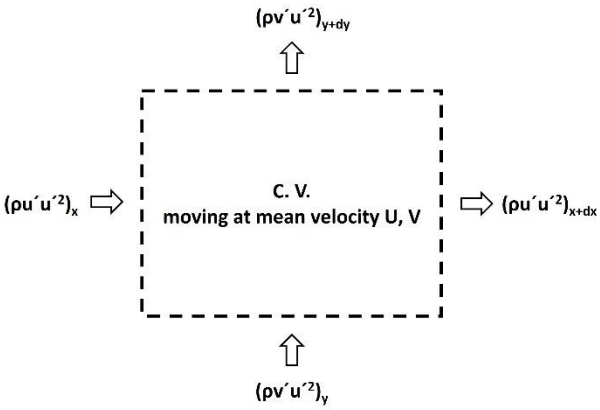

Fig. 6.2 Schematics of the dynamics contained in the Lagrangian turbulence transport that following a control volume moving at the local mean velocity

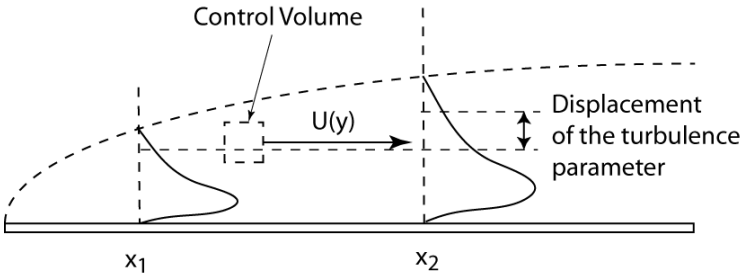

Fig. 6.3 Schematic for the concept of displacement effect that leading to d/dx → d/dy transform. The schematic is from Lee [104]

The conversion of the derivative due to the displacement effect as seen in Fig. 6.3 is expressed as Eq. (6.4).

$$\frac{d}{dx} \rightarrow \pm CU \frac{d}{dy} \qquad \text{Eq. (6.4)}$$

The C is a constant with the unit of ~ $1/U_{ref}$. The +/- sign depends on the flow geometry, i.e., the direction of displacement relative to the reference point. There are no displacement effects for channel flows since the flow is bounded by the walls on both sides. However, we still obtain the above conversion in the spatial gradients using the "probe transform" analysis [104]. Implicit in this transform idea is that both vectors of u′ and v′, and scalar of u'^2 are displaced or transformed in this manner.

For the triple correlations of the u'^2 energy transport equation in Eq. (6.3), a simple product rule is applied with Eq. (6.5).

$$u'^2 v' \approx u' \cdot u'v' \quad \text{and} \quad u'v'^2 \approx v' \cdot u'v' \qquad \text{Eq. (6.5)}$$

Also, pressure and rate of work of pressure are written as $P \approx -\rho v'^2$ and $\frac{d(Pu')}{dx}$, respectively. These are evidently new and unique concepts, and further details can be found in reference papers [103,104].

It is quite well known that the mean velocity profile in channel flows arises due to the mean momentum balance among the Reynolds shear stress, viscous, and pressure

forces, described by RANS [108]. Accordingly, Eq. (6.6) represents this balanced relation among them.

$$\frac{d^2U}{dy^2} = \frac{1}{\nu}\frac{d(u'v')}{dy} + \frac{1}{\mu}\frac{dP}{dx} \qquad \text{Eq. (6.6)}$$

By integrating Eq. (6.6) once with a constant found from the boundary condition, we obtain the mean velocity gradient as Eq. (6.7), which will be used as the starting viewpoint to demonstrate our derived equations along with its plot in Fig. 6.4.

$$\frac{dU}{dy} = \frac{1}{\nu}(u'v') + \frac{1}{\mu}\frac{dP}{dx}\left(\frac{y}{R} - 1\right) \qquad \text{Eq. (6.7)}$$

Validations with DNS Data

In Fig. 6.4 the individual terms in Eq. (6.7) are plotted as showing each profile of the mean velocity gradient, Reynolds stress, and pressure force. More focus is given to the near-wall region, i.e., $y/R < 0.2$, for close inspection and comparison with DNS data for $Re_\tau = 1000$ from Graham et al. [95]. The parameter Re_τ denotes friction velocity based Reynolds number formed $u_\tau R/\nu$, in which R denotes a half channel height.

It may be implemented according to the following procedures. First, inputting u'^2, v'^2, and U from the DNS data on the right-hand side, RHS, of Eq. (6.1) leads to our own version of $d(u'v')/dy$. Subsequently, its numerical integration yields $u'v'$ itself, as plotted in Fig. 6.4. Then, this $u'v'$ is used to derive dU/dy through Eq. (6.7). Successively, both the derived $u'v'$ and dU/dy are comparable to each of the corresponding data from DNS.

There is a very close agreement in the current result with DNS data for the u′v′, although for the dU/dy somewhat less possibly due to the division by a small viscosity. Nonetheless, the dU/dy computed using the u′v′ from Eq. (6.1) and Eq. (6.7) has sufficient accuracy to reproduce the mean velocity profile. To be specific, it has all the structural features such as the initial mild slope in the near-wall region, y/R < 0.004, and then the sharp descent shortly afterward. Consecutively, the gradual transitions to a small slope find between y/R ~ 0.02 to 0.05. These aspects of the dU/dy will result in a flattened velocity profile in channel and other wall-bounded flows, as acknowledged well. Hence, we ascertain that the current dynamics are well realized with the aid of our procedure, in which substituting the u′v′ Reynolds shear stress obtained from Eq. (6.1), and then inputting it into Eq. (6.7).

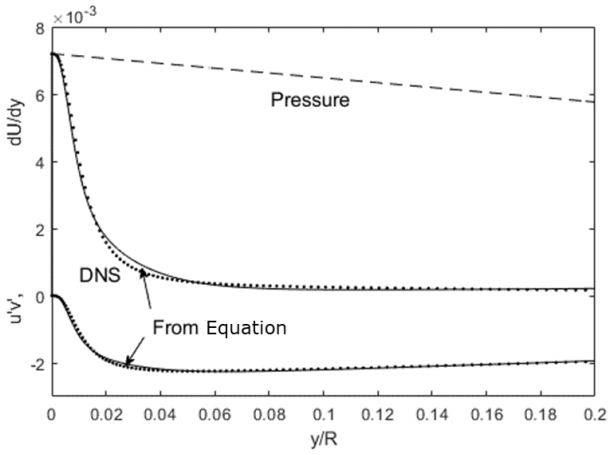

Fig. 6.4 The Reynolds shear stress gradient du′v′/dy of Eq. (6.1) is integrated, and the mean velocity gradient of Eq. (6.7) with the integrated u′v′, both are compared with DNS data from Graham et al. [95] that plotted as dot symbol. The y is normalized by the channel half-width of R, and also u′v′ and U are normalized by u_τ^2 and u_τ

Some analytics on the turbulence structure is facilitated by these dynamical equations while delving into intriguing questions. The first question that arises is what are the origins of these features in dU/dy? It is evidently from the Reynolds shear stress profile [108], which in turn owes to the d(u′v′)/dy shown earlier in Fig. 6.1. In that figure, u'^2 transport term, $-C_{11}U\, du'^2/dy$ in Eq. (6.1), has a sharp negative peak near the wall, y/R ~ 0.01, while the viscous stress near the wall adds to this negativity. This is the reason the Reynolds shear stress in Fig. 6.4 descends rapidly near the wall with an inflection at y/R ~ 0.01. And the negative plateau occurs y/R ~ 0.05 in Fig. 6.4 since that is approximately the location where d(u′v′)/dy → 0 in Fig. 6.1. For the pressure force term in Eq. (6.1), we find from Fig. 6.1 that it compromises the u'^2 transport term to subdue the positive slope to keep its positive slope small. Thus, from the Lagrangian perspective with Fig. 6.1, the negative peak for the Reynolds shear stress gradient in the near-wall is due to the momentum balance between streamwise momentum flux u'^2 and cross-stream momentum flux u′v′ with the pressure force modifying this x-momentum. Reynolds shear stress is the cross-stream momentum flux to balance the large streamwise flux of u′. Consequently, tracking the terms in Eq. (6.1) with Fig. 6.1 allows us to predict the dU/dy trajectory as found in Fig. 6.4.

The next question is what brings forth the structure for x-momentum u′, or its flux u'^2? This momentum component is typically expressed through its kinetic energy manifestation, $(u'_{rms})^2 = \overline{u'^2}$. Eq. (6.3) is the Lagrangian transport equation for the u'^2 flux, $u'^3 = (u'_{rms})^3$, which consists of the lateral flux of u'^2, pressure work, and viscous dissipation term. Fig. 6.5 shows the comparison of Eq. (6.3) with DNS data [95] for du'^3/dy. In the same way as previously implemented, DNS data for u'^2, v'^2, and u′v′, are

input on the RHS of Eq. (6.3), to come up with our own "mix" for du'^3/dy, and plotted in Fig. 6.5 to validate the Lagrangian energy balance. The budget terms, consisting mainly of lateral flux and pressure work, add to a nearly perfect match with DNS data, in spite of the fact that the viscous term was omitted. It justifies, however, due to its small magnitude. Thus, Eq. (6.3) depicts the Lagrangian transport for u'^2, as validated with DNS data, and presents us with a dynamical picture wherein u'^2 is transported laterally by v', while some of that energy is expended through pressure work that is with the negative sign correctly. The lateral transport is compacted toward the wall, and this causes a very sharp peak near the wall region. This peak then undergoes a gradual decline to the centerline boundary condition, as observed in wall-bounded flows. Notice that most of the action is over by y/R = 0.05 at this Reynolds number, with only a small residual negative slope beyond that.

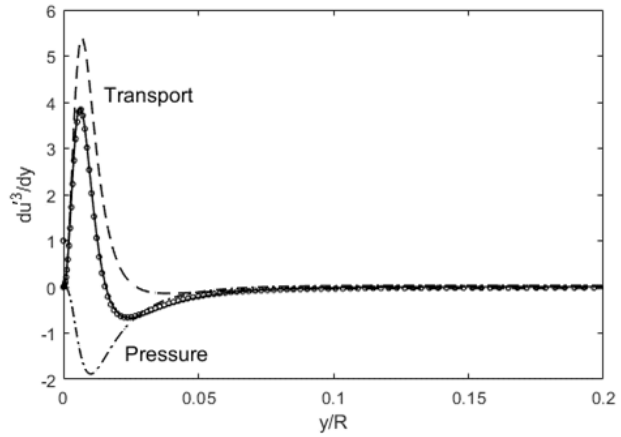

Fig. 6.5 The budget for u'^2 of kinetic energy in Eq. (6.3), and comparison with DNS data from Graham et al. [95] that plotted as symbol, normalized by friction velocity u_τ

Lastly, what stands in a causal relation for the structure of y momentum flux v'^2? Fig. 6.6 shows Lagrangian momentum balance for v′ through dv'^2/dy. In this figure, sub-components of the v′ momentum balance have been plotted, which includes each term in the RHS of Eq. (6.2). In comparison to the DNS data [95], the agreement is nearly exact till y/R ~ 0.1. Although the negative slope is slightly less than DNS beyond y/R ~ 0.1, it could be corrected by enforcing the centerline or the total v'^2 content with boundary conditions. It is worth mentioning that more emphasis should be placed on the profile near-wall region. In this regard, the v′ momentum balance of Eq. (6.2) gives favorable results overall. Indeed, it is usually the near-wall where dynamics are more complex and difficult to predict. The triad of forces which are subject to u′v′ transport, pressure, and viscous, make influence intricately to cause the v'^2 profile near the wall. It is also interesting to note that the pressure term is the most dominant, which would represent a feedback mechanism to outline the v'^2 distribution in wall-bounded flows; it finds that the profile of the pressure term multiplied by an arbitrary constant is comparable solely to the v'^2 profile as seen in Fig. 6.6. When we use $P = -\rho v'^2$, then the role of v'^2 is quite significant as it modifies the turbulence structure, and this will be pronounced in boundary layer flows too, that discussed later. Considering that the moving control volume is subjected to the shifted gradient in lateral profiles as illustrated in Fig. 6.3, the $C_{22}U$ term must be factored into the dP/dy in Eq. (6.2), in order to account for this displacement effect.

We have posed the above structural questions separately. However, in effect, Eq. (6.1), Eq. (6.2), and Eq. (6.3) contain a coupling among the turbulence variables, u'^2, v'^2 and u′v′ so that we can start our logical train with any one of these three components. The

important conclusion is that the Lagrangian transport equations furnish the inter-relationships between the turbulence variables, thus we can obtain a succinct view of the underlying dynamics, and also compute and reconstruct the variables directly. Moreover, the same set of transport equations holds for turbulent flows in various geometries [103,104]. Let us see what this new perspective can reveal when we examine boundary layer flows over a flat plate.

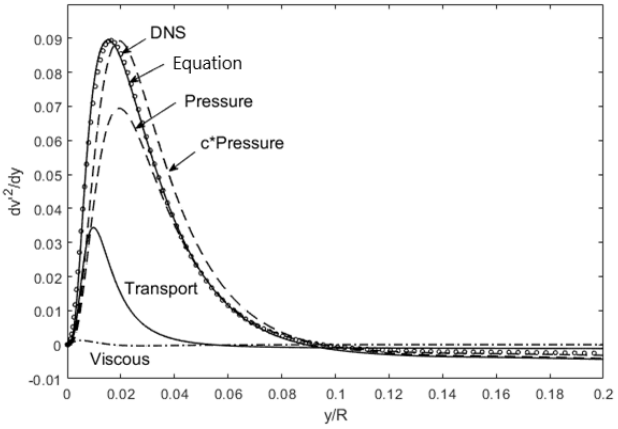

Fig. 6.6 The budget for v′ momentum in Eq. (6.2), and comparison with DNS data from Graham et al. [95] that plotted as symbol, normalized by u_τ^2

Fig. 6.7 is a plot exhibiting the Reynolds shear stress gradient budget, for flow over a flat plate with a zero pressure gradient, ZPG. The DNS data from Spalart [92] are used in comparison for $Re_\theta = 670$, where Re_θ is a momentum thickness based Reynolds number. The description of Fig. 6.7 finds in a similar manner to the previously examined one of channel flow, in that the contribution of the viscous term to the Reynolds stress gradient is relatively small and limited to the near-wall region. For the u'^2, i.e., longitudinal transport term, it has the largest effect particularly near the wall due to its

steep gradient. For the pressure force term, in the current Lagrangian analysis, it is manifest in the cross-stream direction due to the displacement effect; movement of the control volume in the displaced boundary layer will cause a small but finite pressure imbalance in the y-direction, and that is expressed in Eq. (6.1) through $dP/dx \approx -CUdv'^2/dy$ where the mean pressure is approximated as $P \sim -\rho v^2$ [109]. These three terms all add up near to the Reynolds stress gradient precisely as shown in Fig. 6.7.

The Reynolds shear stress appears structurally similar to those from channel flows, meanwhile, this flat plate flow contains some pronounced positive slope bulging, as one moves away from the wall. And it finds that this bulge is induced by the combination of the transport and pressure terms. This has some consequences if the flow is subjected to an adverse pressure gradient, APG, as will find in the following context.

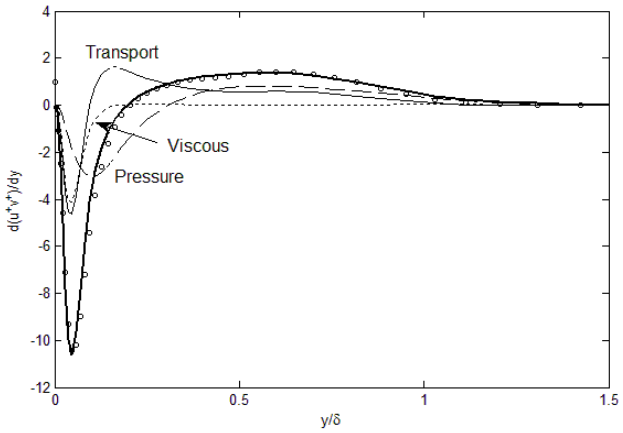

Fig. 6.7 Reynolds shear stress gradient budget for flow over a flat plate at zero pressure gradient. The DNS data with $Re_\theta = 670$ from Spalart [92] as symbol, and solid line from Eq. (6.1). The y is normalized by boundary layer thickness δ, u^+v^+ is nondimensional after normalized by u_τ^2

To begin with, we preview the alterations of the basic turbulence parameters when an adverse pressure gradient, APG, is applied for boundary layer flows by plotting u'^2 and v'^2 from DNS data in Fig. 6.8. Both the u'^2 and v'^2 profiles contain pronounced protuberance relative to ZPG in the mid-layer region; in ZPG, the u'^2 and v'^2 have a monotonic decrease after the near-wall peak. To be specific, the protuberance appears where in positive slope for $100 < y^+ < 380$ then negative slope for $380 < y^+ < 900$. And the few weak undulations between $y^+ \sim 500$ to 900 are observed too. As having these behaviors, Eq. (6.1) predicts that profiles of $d(u'v')/dy$ will reflect these aspects, drawing similar features in the Reynolds shear stress; recall that Eq. (6.1) includes the first order gradient of u'^2 and v'^2.

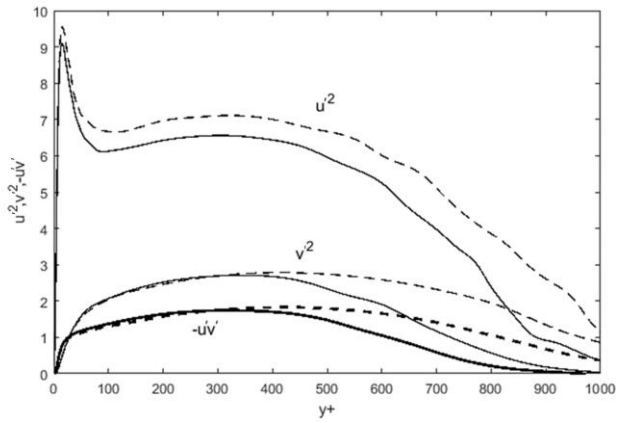

Fig. 6.8 Reproduced profiles of basic turbulence variables for $-u'v'$, u'^2, and v'^2. The DNS data from Kitsios et al. [93] for flow over a flat plate with adverse pressure gradient in $Re_\theta = 3500$ as solid line and $Re_\theta = 4800$ as dash line; $y^+ = yu_\tau/\nu$, each of $-u'v'$, u'^2, and v'^2 is normalized by u_τ^2 where u_τ is a friction velocity

In Fig. 6.9, the plots of the individual terms in Eq. (6.1) are shown, and the sum of these terms is compared with DNS data under the adverse pressure gradient. The viscous

term is included to illustrate its impact despite its numerical perturbations. It does add to the overall momentum balance, but it seems for a neat plot, a higher definition of data than what was available to us is required to compute its second-order gradient accurately; recall that in Eq. (6.1) viscous term includes the second-order gradient.

(a)

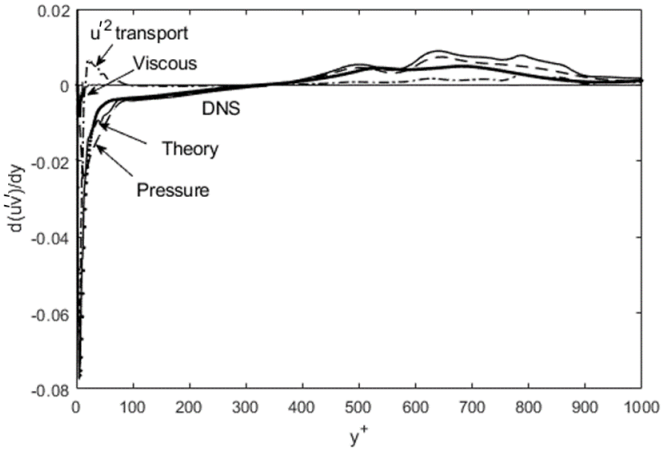

(b)

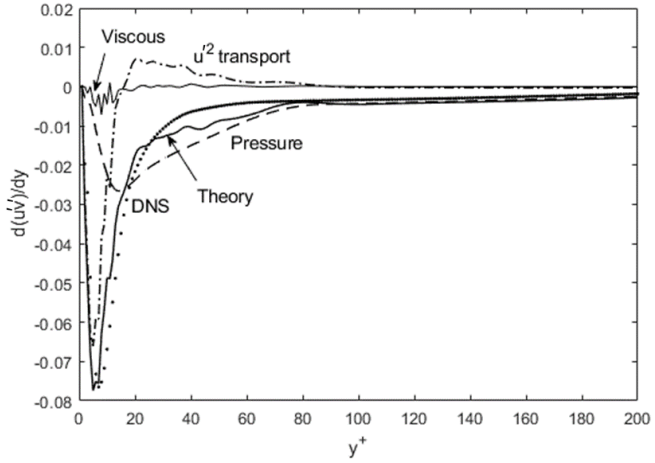

Fig. 6.9 Reynolds shear stress gradient budget for flow over a flat plate with adverse pressure gradient. The DNS data as dot symbol from Kitsios et al. [93] at $Re_\theta = 3500$, and solid line from Eq. (6.1); (b) contains the same data as (a), with zoom in on the near-wall region

Fig. 6.9(a) shows the entire d(u′v′)/dy profile across the boundary layer, while Fig. 6.9(b) zooms in on the near-wall region for a closer inspection. The overall agreement between Eq. (6.1) and DNS results is good across the boundary layer, however, the gradients are not entirely smooth and there are some deviations. This includes the undulations away from the wall, which is mimicked but not exactly followed. This is attributed to the tracing of the DNS data from Kitsios et al. [6], leading to some errors when taking the gradient of the transcribed data. And this kind of numerical differentiation error is also present from a close inspection of the near-wall region in Fig. 6.9(b). And, there is some deviation from DNS data at the inflection point, i.e., $y^+ \sim 40$ with some small spikes and undulations, but still, Eq. (6.1) tracks the DNS data reasonably well. Therefore, the overall structure and origin of the Reynolds shear stress are moderately captured by Eq. (6.1), providing further ascertainment with a different flow geometry.

As for the features in u'^2 and v'^2 profiles translating to d(u′v′)/dy, Fig. 6.8 is brought back and examined their tendency once again. The profiles of both u'^2 and v'^2 after the near-wall peak, increase for $100 < y^+ < 380$ and then decrease for $380 < y^+ < 900$, in which both slope or equivalently gradient are expected to be positive and then negative. This protuberance leads to a positive short, and then negative long slope, and for du'^2/dy and dv'^2/dy, being short positive and then negative. Since the u'^2 transport and pressure terms, i.e., the first and second term on the RHS of Eq. (6.1), point toward d(u′v′)/dy having the negative sign, the opposite trend is expressed in Fig. 6.9, i.e., a negative shortly before positive long, over the range of $100 < y^+ < 900$.

While the u'^2 transport effect is quite strong at $y^+ < 100$, however, since it is the pressure force that dictates the momentum balance afterward, the adverse pressure gradient effect is manifest through the pressure term and onto $d(u'v')/dy$ during $380 < y^+ < 900$. These distinctive features for the Reynolds shear stress with APG result in the mean velocity profile that exhibits different slopes in comparison to ZPG for the same region of $380 < y^+ < 900$ [93].

In summary, the transport equation set, Eq. (6.1), Eq. (6.2), and Eq. (6.3), is based on the fundamental fluid physics of momentum and energy conservation in a specific moving coordinate frame, and provides intuitive, dynamical explanations. Eulerian versions of the same phenomena tend to hide the underlying dynamics, first due to a large number of inter-correlated source and sink terms, and secondly, when layers of complex ad-hoc models, e.g., mean gradient transport, are introduced to the pure transport equations, then basic fluid physics of turbulence tends to become obscured or at times abandoned. As validated, the current turbulence transport equations provide a clear view of turbulence physics. In addition, it points to a viable solution method since there is a sufficient number of equations, i.e., Eq. (6.1), Eq. (6.2), Eq. (6.3), and Eq. (6.7) for the unknown turbulence variables. In specific, the transport expressions for $u'v'$, v'^2, and u'^2 corresponding to Eq. (6.1), Eq. (6.2), and Eq. (6.3), along with RANS of Eq. (6.7) for U, they furnish an inter-coupled but complete set of equations to solve for these variables; four equations with four variables reserve the solvability. The following Steps are to draw up guidelines for the attainment, that has been used similarly in previous work [103];

1. Start from initially estimated test functions for u'^2, v'^2, and U
2. Compute then integrate d(u′v′)/dy to find u′v′ using Eq. (6.1)
3. Use u′v′ in Eq. (6.7) to compute dU/dy and then integrate to find U
4. Update v'^2 using the computed d(u′v′)/dy and U in Eq. (6.2)
5. With the computed u′v′, U, and updated v'^2, update u'^2 using Eq. (6.3)
6. Repeat until convergence

Fig. 6.10 and Fig. 6.11 show the result of running the above routine. The starting test functions for u'^2 and v'^2 are lognormal functions, while we expedite the numerics with an initial $U = y^{1/n}$ where n = 7. All the test functions including this U, are updated using Eq. (6.1), Eq. (6.2), and Eq. (6.3) during the iteration. To facilitate convergence, we also use a y^{-m} type of function for u'^2 on the "backside", e.g., for channel flows y/R = 0.5 ~1, which ensures the boundary conditions are enforced both at y/R = 0 and 1. It is found that a reasonable u'^2 profile starts to emerge after just one iteration. And then it is enforced at y/R = 1 by the centerline boundary condition as setting $u'^2 = (u'^2)_{y/R=1}$, seen in Fig. 6.10. The $(u'^2)_{y/R=1}$ can be obtained from DNS data, or estimated from E with Eq. (6.8) in below context.

Reynolds shear stress is obtained from the Step 2, which leads to the mean velocity profile in Step 3. This resulting single iteration for the mean velocity shown in Fig. 6.11 is quite close to the DNS data. In order to circumvent integration errors in the mid-layer, dU/dy is integrated from both y/R = 0 and 1 until the solutions intersect, e.g., at about y/R = 0.6. The outer solution has a small slope that is fairly close to the often used approximation, $U \sim y^{1/n}$ [109]. The inner solution advances to this "power-law"

region while tracking all the DNS data closely. An important point to be made here is that the mean velocity profile in Fig. 6.11 satisfies the RANS of Eq. (6.7) along with other transport equations that are associated with or needed to solve it; Eq. (6.1) for the Reynolds shear stress u′v′, that goes in Eq. (6.7) explicitly, and then into Eq. (6.2) and Eq. (6.3) for v'^2 and u'^2, respectively. Thus, the U profile is a valid solution to RANS since it satisfies Eq. (6.1), Eq. (6.2), and Eq. (6.3) implicitly as well as Eq. (6.7) explicitly.

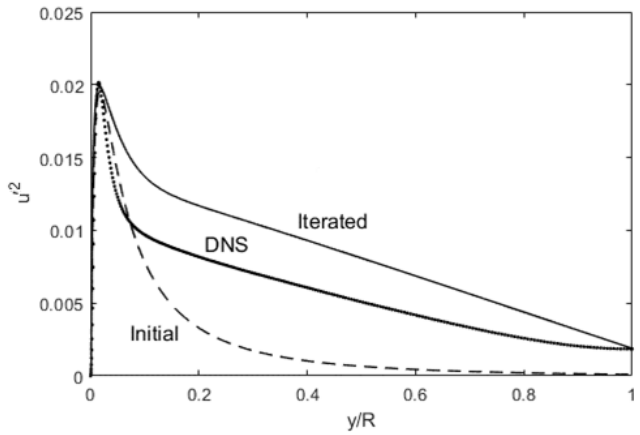

Fig. 6.10 Turbulence kinetic energy u'^2, iterated using Eq. (6.1), Eq. (6.2), Eq. (6.3), and Eq. (6.7) in comparison with DNS data from Graham et al. [95]

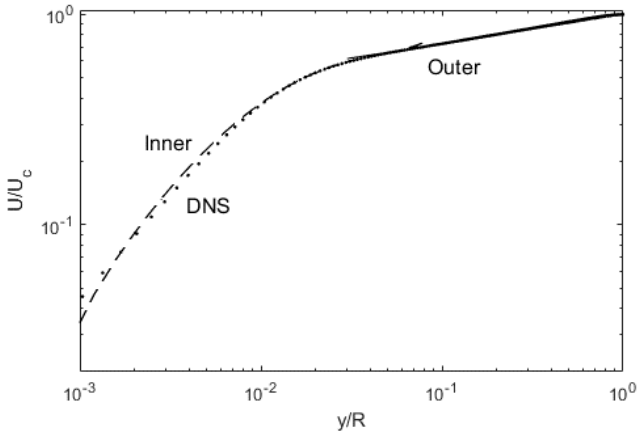

Fig. 6.11 Normalized mean velocity profile, iterated using Eq. (6.1), Eq. (6.2), Eq. (6.3), and Eq. (6.7) in comparison with DNS data from Graham et al. [95]

6.2 Scaling in Gradient Profile of Reynolds Stress

In the near-wall region for wall-bounded turbulent flow, non-dimensional inner variables u^+ and y^+ are customarily used in describing its profile of interest. The u^+ denotes the mean velocity scaled by a friction velocity u_τ, and the y^+ denotes the distance away from the wall scaled by a viscous length scale ν/u_τ. Those scalings are advantageous in attempting to illustrate turbulence structures. Specifically, among different flows, characterized by Re_τ, i.e., $\delta u_\tau/\nu$ where δ is a boundary layer thickness which could be a half-channel width or a diameter, some identical features can be captured under the inner coordinates. For example, a near-wall peak of turbulent intensity scaled by the inner variable, $u^{2+} = \overline{u'^2} / u_\tau^2$, was found to be located at the same inner coordinate of y^+ [110]. As a matter of fact, the y^+ coordinate is equivalent to the local Reynolds number consisting of y and ν/u_τ, therefore, a universal profile in turbulence structure can be investigated by means of the inner coordinates.

For boundary-layer flows with zero pressure gradients, the normalized one-dimensional turbulence kinetic energy, $u'^{2+} = u'^2 / u_\tau^2$, with respect to y/δ where y is normalized by the outer length scale δ of boundary layer thickness, exhibits a progression of the profiles, with a peak sharpening and moving closer to the wall with an increasing Reynolds number [111]. Similarly, a negative peak in the Reynolds shear stress, $u'v'$, moves closer to the wall with a gradual ascent toward zero centerline boundary condition in the outer coordinate of y/δ [111]. For pipe flows, the pattern for u'^{2+} is similar, but interestingly the peak location in the inner coordinates is mostly invariant at $y^+ \sim 15$ [110]. The scalability of these turbulence variables will have significant implications on the structure of channel flows, including the mean velocity profiles [112].

Here, scaling and structural evolutions are contemplated in a new perspective for turbulent channel flows. The total integrated turbulence kinetic energy remains constant when normalized by the friction velocity squared, while the total dissipation increases linearly with respect to the Reynolds number. This serves as a global constraint on the turbulence structure.

Motivated by the flux balances in the root turbulence variables, we discover dissipative scaling for u'^2 and v'^2, respectively through its first and second gradients. This self-similarity allows the profile reconstruction at any Reynolds numbers based on a common template, with a simple multiplicative operation. Using these scaled variables in the Lagrangian transport equations derives the Reynolds shear stress, which in turn computes the mean velocity profile. The dissipation scaling along with the transport equations render possible views of the turbulence dynamics and computability of the full structure in channel flows.

Let us begin by taking a brief look at Fig. 6.12 the evolution of one-dimensional turbulence kinetic energy u'^2 for a sequence of Reynolds number Re_τ. The channel flow data are from the DNS works of Iwamoto et al. [98], Graham et al. [95], and Lee and Moser [90]. In our work, u'^2 and other turbulence variables are normalized by a friction velocity squared u_τ^2, e.g., as denoted by u'^{2+}, but at times written as u'^2 in abbreviation. A pronounced feature of the u'^2 curves is the movement of peak location toward the wall, and it is known that when plotted in the inner coordinate y^+, this point tends to stay fixed [110]. The peak height elevates with an increasing Reynolds number, even after normalizing by u_τ^2 as shown in Fig. 6.12. No single function seems capable of collapsing the curves with any kind of stretching or scaling, particularly because of the sharp peak followed by an abrupt bend close to the wall, e.g., for $Re_\tau = 5200$. However, if we make an estimate of the area under each curve in Fig. 6.12, the possibility emerges that a total integrated turbulence kinetic energy may be constant; denoted by E, defined in Eq. (6.8).

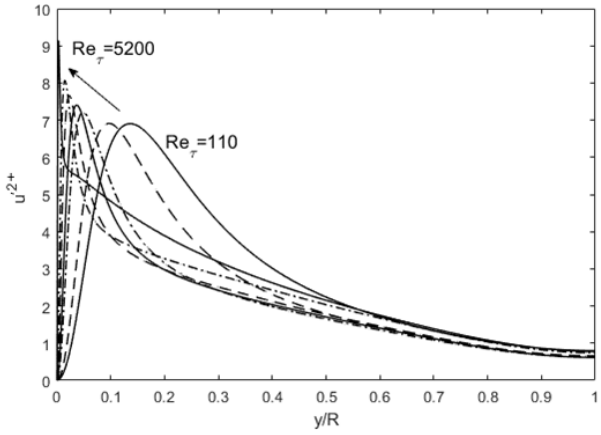

Fig. 6.12 Reproduced u'^{2+} profiles showing a progression from $Re_\tau = 110$ to 5200; DNS data of $Re_\tau = 110$, 150, 300, 400, 650 from Iwamoto et al. [98]; $Re_\tau = 1000$ from Graham et al. [95]; $Re_\tau = 5200$ from Lee and Moser [90]

Indeed, numerical integration by Eq. (6.8) shows that this total integrated turbulence kinetic energy, E, is invariant with respect to the Reynolds number. This owes to the fact that u_τ is the momentum scale representing a total available momentum, which would then makes u_τ^2 the energy scale. Therefore, normalizing by the global energy scale results in constant E, as shown in Fig. 6.13. Additionally, we define a total integrated dissipation, Φ, as in Eq. (6.9) based on the gradient of the square root of u'^2, which presents a linear dependence on the Reynolds number in Fig. 6.13.

$$E = \int_0^1 u'^{2+}(y)\, d\left(\frac{y}{R}\right) \qquad \text{Eq. (6.8)}$$

$$\Phi = \int_0^1 \left(\frac{du'^{+}}{dy}\right)^2 d\left(\frac{y}{R}\right) \qquad \text{Eq. (6.9)}$$

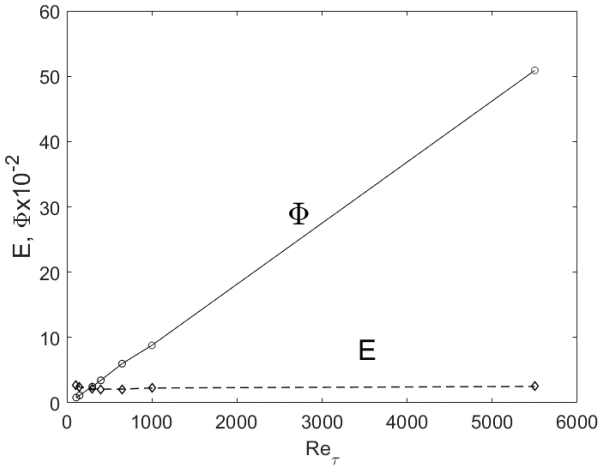

Fig. 6.13 The total turbulence kinetic energy E, and dissipation Φ, as a function of Reynolds number from 110 to 5200; DNS data of Re_τ = 110, 150, 300, 400, 650 from Iwamoto et al. [98]; Re_τ = 1000 from Graham et al. [95]; Re_τ = 5200 from Lee and Moser [90]

Consequently, those global characteristics reaffirm u_τ^2 as a useful energy scale, and also provoke the following interpretations; (1) the total turbulence kinetic energy E remains constant even though the "internal" transport distributes u'^2 in progressively skewed curves, (2) the dissipation Φ must increase with Reynolds number as the restraining effect of viscosity is reduced relative to the turbulence energy that exists in the flow. These may be considered as global constraints on the u'^2 distribution; $E \approx$ const., and $\Phi \approx A\, Re_\tau$ where A is a constant. If we perceive the dissipation through a thermodynamic lens, then it is recognizable as the degree of disorder that exists in the system. When the restoring force of viscosity is relatively reduced at higher Reynolds numbers, then it would spare more room for the disorder. Accordingly, dissipation must occur as showing severe skewness in the profile. Therefore, we postulate that the Φ increases with respect to the Reynolds number proportionately.

In this light, Fig. 6.13 indicates some potential scaling of the plot with the "local dissipation" in y/R coordinates. The above observations together with the transport equations of Eq. (6.1), Eq. (6.2), and Eq. (6.3) elicit us to ponder upon the internal dissipation structure. Recalling that an invariant u'^{2+} peak location in the y^+ coordinate is observed in experimental [110] and DNS [90,98] data, we redefine the dissipation scaling in the y^+ coordinate, such as $\varepsilon^+(y^+) = du'^{2+}/dy^+$. Then, an interesting pattern emerges, as found in Fig. 6.14. Note that the differentiation for ε^+ is with respect to the y^+ coordinate, and it differs from the y, y/R coordinate, or d/dy operation in Eq. (6.8) and Eq. (6.9).

In Fig. 6.14, the $\varepsilon^+(y^+)$ curves appear to merge for all Reynolds numbers except for the positive and negative peaks that protrude progressively in an inverted manner. That is, the positive peak in $\varepsilon^+(y^+)$ increases with Re_τ, while the negative peak decreases

in magnitude. Therefore, the dissipation curves, $\varepsilon^+(y^+)$, are self-similar with an inverted proportionality on either side of a zero-crossing. The zero-crossing means the position where a profile is across the axis of abscissa with $\varepsilon^+(y^+) = 0$. Alternatively, in this profile the zero-crossing is equivalent to the near-wall peak position of u'^{2+}, hence denoting by y^+_{peak}. To explain, it is at $\varepsilon^+(y^+) = du'^{2+}/dy^+ = 0$, satisfying the change of the sign of slope in u'^{2+} curvature.

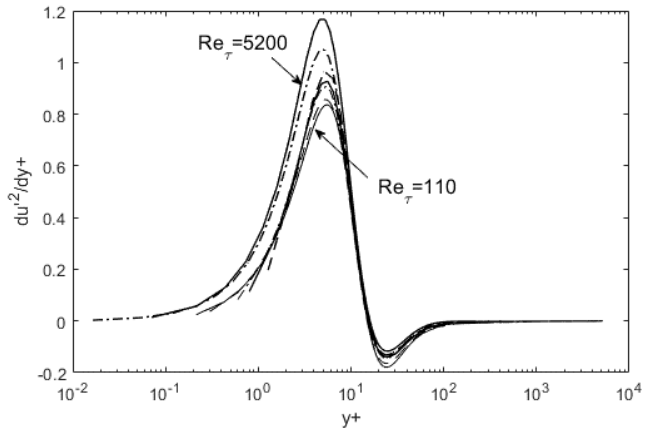

Fig. 6.14 The du'^{2+}/dy^+ profiles from $Re_\tau = 110$ to 5200. The near-wall peaks ascend, and the negative undulations reduce in magnitude with increasing Reynolds number. DNS data of $Re_\tau = 110$, 150, 300, 400, 650 from Iwamoto et al. [98]; $Re_\tau = 1000$ from Graham et al. [95]; $Re_\tau = 5200$ from Lee and Moser [90]

This calls for an asymmetrical scaling in the front ($y^+ < y^+_{peak}$) and back ($y^+ > y^+_{peak}$) sides, as depicted in Fig. 6.15(a) and Fig. 6.15(b). For the front side, the scaling factor increases, while for the back side the opposite is applicable. Multiplying asymmetrical scaling factors to the template profile at a very low Reynolds number, $Re_\tau = 110$, replicates the du'^{2+}/dy^+ curves at all others up to $Re_\tau = 5200$. Consequently, this analysis justifies that the dissipative structure scales with the Reynolds number.

With asymmetrical boundary conditions on $u'^2 = 0$ at y = 0 and $u'^2 > 0$ at the centerline, the internal transport dynamics end up with the resulting u'^2 distributions in space as prescribed by Eq. (6.3) while enforced by the global constraints of $E \approx$ const. and $\Phi \sim Re_\tau$. As shown earlier in Fig. 6.5, the interior fluxes are delineated by Eq. (6.3), and the dissipation scaling exhibited in Fig. 6.15 is the result of this re-distribution process. Therefore, the self-similarity in du'^{2+}/dy^+ can be regarded as the manifestation that a Reynolds number is the sole dynamical parameter in the transport equations.

(a)

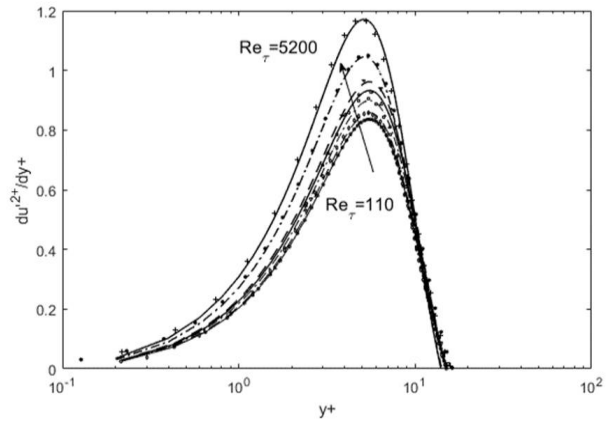

(b)

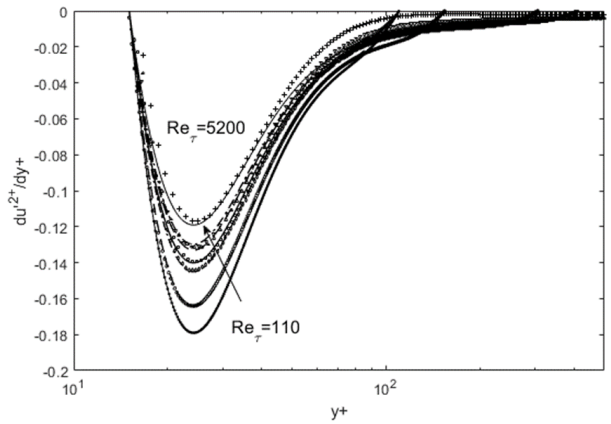

Fig. 6.15 Comparison of the scaled profiles of du'^{2+}/dy^+ from Re_τ = 110 to 5200 based on the template at Re_τ = 110. (a) Near-wall side prior to the zero-crossing, and (b) aft side. DNS data of Re_τ = 110, 150, 300, 400, 650 from Iwamoto et al. [98]; Re_τ = 1000 from Graham et al. [95]; Re_τ = 5200 from Lee and Moser [90]

A beneficial characteristic of this scaling is that we can start from a base template of the du'^{2+}/dy^{+} profile at any low Reynolds number and reconstruct curves at other higher Re_{τ}. Although at high Reynolds numbers, the curves start running out of the y^{+} range with some deviations on the back side seen in Fig. 6.15(b), nevertheless the scaling covers a wide dynamic range from Re_{τ} = 110 to 5200 across individual data sets [90,95,98]. The errors are mostly on the backside and within tolerable margins. It could be remedied by changing a baseline template at a higher Reynolds number or adjusting the centerline boundary condition in corrective extrapolation algorithms. Likewise, the du'^{2+}/dy^{+} profiles show the possibility of self-similarity. With this scaling and via the transport equations of Eq. (6.1), Eq. (6.2), and Eq. (6.3), a reconstruction of the entire turbulence structure is realizable, as will be demonstrated in the next section.

In Fig. 6.16(a), we can see that the peak of the dv'^{2+}/dy^{+} elevates in a similar manner as the du'^{2+}/dy^{+} profiles, but the trailing edge continues to digress outward. On the other hand, the aligned peaks indicate that their second-order gradient should all merge at the zero-crossing point on that profile. Indeed, it turns out that taking a second-order gradient as $d^2v'^{2+}/dy^{+2}$ exhibits a self-similarity structure found in Fig. 6.16(b). The scaling factors in Fig. 6.17 this time monotonically increase on both sides of the zero-crossing point.

The governing equations for u'^2 and v'^2 are evidently different; Eq. (6.3) and Eq. (6.2) are energy- and momentum-conserving equations, respectively. This leads to the speculation on the existence of different scaling schemes that are involved; the energy is dissipated by the first gradient squared while the momentum diffusion is prescribed by

the second-order gradient, thus resulting in the different gradient scalings between the energy and momentum.

(a)

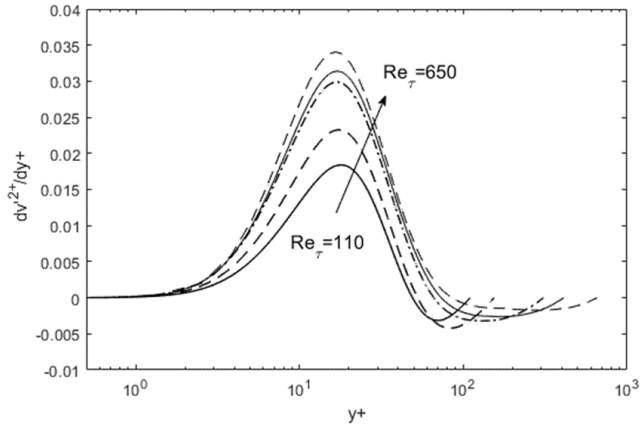

(b)

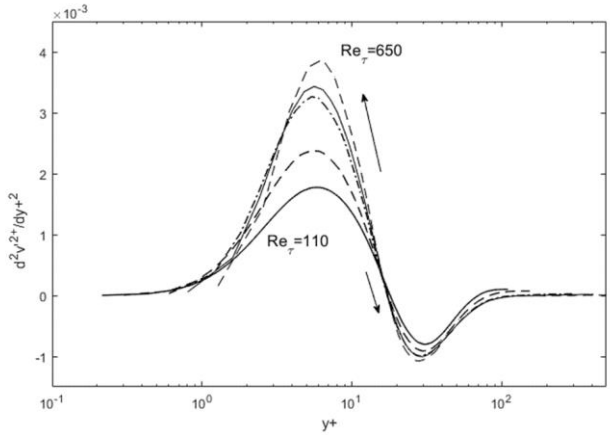

Fig. 6.16 The (a) dv'^{2+}/dy^{+} profiles, and (b) $d^2v'^{2+}/dy^{+2}$ profiles from Re_τ = 110 to 650. The v'^{2+} is applied dissipation scaling via second-order gradient as in (b); DNS data of Re_τ = 110, 150, 300, 400, 650 from Iwamoto et al. [98]

In Fig. 6.17, the template for a second-order gradient of v'^{2+} at a lower Reynolds number, Re_τ = 300, can be expanded through simple arithmetic stretching to replicate the profiles at any higher Reynolds number, Re_τ = 1000 and 5200. Reconstruction to the

$d^2v'^{2+}/dy^{+2}$ profiles simply involves multiplication by monotonically increasing scaling factors, that are disproportionate for the front and back sides.

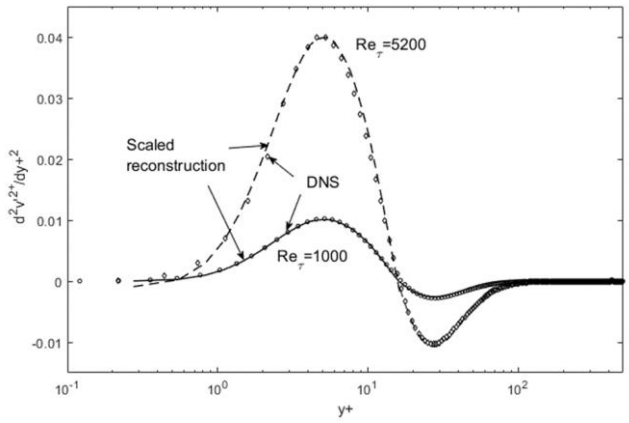

Fig. 6.17 Comparison of the scaled profiles of $d^2v'^{2+}/dy^{+2}$ based on the template at Re_τ = 300, with DNS data of Re_τ = 300 from Iwamoto et al. [98], Re_τ = 1000 from Graham et al. [95], Re_τ = 5200 from Lee and Moser [90]

The second-order gradient profiles for the Reynolds shear stress, $d^2u'v'^{+}/dy^{+2}$, are shown in Fig. 6.18. The zero-crossing points tend to merge, but as Reynolds number increases both the negative- and positive-segment widths are broadened. Also, the scaling factor exhibits a steady increase for Re_τ = 110 to 650, but leaps and insignificantly varies from Re_τ = 1000 to 5200, having the scaling behavior out of expectation. A possible speculation is that u'^2 and v'^2 flux terms scale differently, and the cross-transport $u'v'$ contains the mixture of both elements contributing in as Eq. (6.1), hence resulting in the scaling deviations. There may be some pertinent operations or alternative coordinates utilizable specifically for the "mixed" variable such as the Reynolds shear stress, although we defer pursuing such a possibility. Instead, we turn to examine the Reynolds

shear stress variations by using self-similar, scalable u'^2 and v'^2 gradients with the transport equation Eq. (6.1) in the next section.

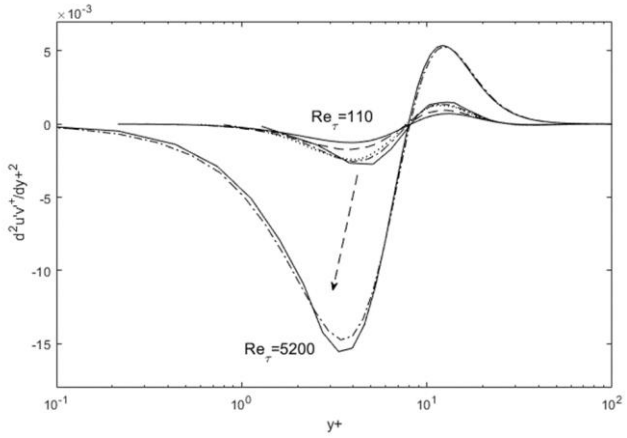

Fig. 6.18 The $d^2u'v'^{+}/dy^{+2}$ profiles from Re_τ = 110 to 5200. The $u'v'$ is applied dissipation scaling via second-order gradient. DNS data of Re_τ = 110, 150, 300, 400, 650 from Iwamoto et al. [98]; Re_τ = 1000 from Graham et al. [95]; Re_τ = 5200 from Lee and Moser [90]

To summarize, the gradient profiles of turbulence stresses bring our attention to their self-similarity, and scalability with respect to the Reynolds number. The scalability is viable as capturing well essential features of wall-bounded turbulent flows across the entire width of the boundary layer. And applying the different order of gradient is apposite to this scaling, such that first-order gradient for u'^{2+}, and second-order gradient for v'^{2+} and $u'v'^{+}$. This remark is germane to the dynamics in which either dissipation or diffusion is involved with the corresponding Reynolds stress transport formation. In addition to that, the zero-crossing point draws attention that emerges from the gradient profiles; the local maximum of u'^{2+}, and the inflection point of v'^{2+} and $u'v'^{+}$.

Since the peak and nadir magnitudes of the gradient of u'^{2+}, v'^{2+}, and $u'v'^{+}$ vary asymmetrically with respect to Reynolds number, by adjusting scaling factors with Reynolds number, e.g., maximum and minimum of du'^{2+}/dy^{+} as a function of Reynolds number, the profiles with different Reynolds numbers could be reconstructed. As for the scaling factors, they are dealt with in the way of making a unitary functional form of the gradient structure, which we will find in the following section.

6.3 Gradient Structure Functions for Reynolds Stress

A single profile to represent the gradient structure of Reynolds stress is suggested as a functional form for channel flows and flat plate flows. To be precise, the gradient profiles of Reynolds stresses in Fig. 6.19, Fig. 6.20, and Fig. 6.21 are constructed using the two distinctive structure functions from Eq. (6.10) and Eq. (6.11), which zero-crossing point near the wall is the watershed. Because of having a different magnitude between maximum and minimum for the gradient profile at each of the different Reynolds numbers, it necessitates the adjustment of both magnitudes being ratioed, so that multiple profiles get congregated as being laid closely onto the single representative structure which made by Eq. (6.10) and Eq. (6.11).

Modified Gaussian Function (prior to zero-crossing):

$$f(x) = y_o + \frac{A}{t_0} e^{\left[\frac{1}{2}\left(\frac{w}{t_0}\right)^2 - \frac{x-x_c}{t_0}\right]} \frac{1}{2}\left[erf\left(\frac{z}{\sqrt{2}}\right) + 1\right] \qquad \text{Eq. (6.10)}$$

where $\quad erf(z) = \frac{2}{\sqrt{\pi}} \int_0^z e^{-y^2} dy$

, and $z = \frac{x-x_c}{w} - \frac{w}{t_0}$

Exponentially-Decaying Sinusoidal Function (aft of zero-crossing):

$$g(x) = y_o + Ae^{-\frac{x}{t_0}} sin\left(\pi \frac{x - x_c}{w}\right) \qquad \text{Eq. (6.11)}$$

Table 6.1 Coefficients used in the functions of Eq. (6.10) and Eq. (6.11), for Fig. 6.19, Fig. 6.20, and Fig. 6.21

		y_o (offset)	A (amplitude)	x_c (phase shift)	w (period)	t_o (decay const.)
$\frac{du'^{2+}}{dy^+}$	Eq. (6.10)	-0.45851	19.0855	2.2697	2.74361	6.9332
	Eq. (6.11)	-0.0258	5606.23332	-67342.61328	67358.30435	9.74248
$\frac{d^2v'^{2+}}{dy^{+2}}$	Eq. (6.10)	-0.36326	17.45365	2.38421	2.55586	7.04135
	Eq. (6.11)	-0.0095	2432.8139	-29463.52313	29480.08518	11.3206
$\frac{d^2u'v'^{+}}{dy^{+2}}$	Eq. (6.10)	0.26135	-7.064892	2.56368	1.8676	1.39541
	Eq. (6.11)	0.00437	3.15388E7	7.88493	8.68622E7	4.30653

The du'^{2+}/dy^+ profile in Fig. 6.19 shows that on the near-wall side $y^+ < 15$, i.e., prior to the zero-crossing point of $y^+ \sim 15$, is traced by the Modified Gaussian Function Eq. (6.10), while on the aft side $y^+ > 15$, Exponentially-Decaying Sinusoidal Function Eq. (6.11) suffices to approximate DNS data. Parametric modifications are made in these functions to capture the structural curves of the gradients, and the parameters are listed and tabulated in Table 6.1.

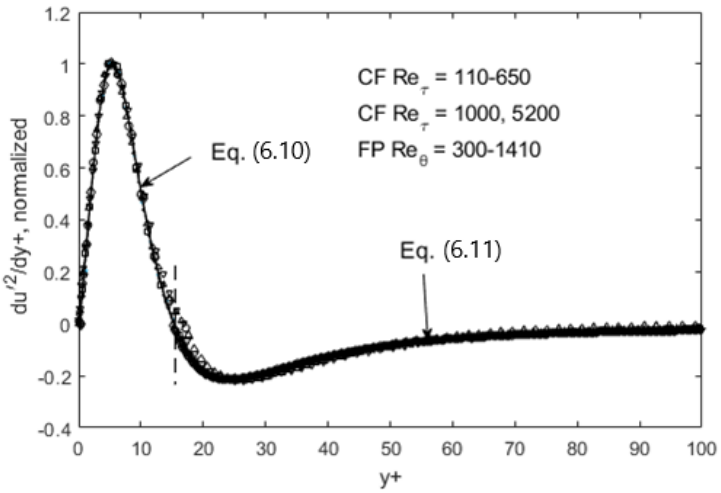

Fig. 6.19 The du^{+2}/dy^{+} profiles with gradient structure functions, ratioed by respective peak and nadir heights in left and right of zero-crossing $y^{+} \sim 15$ to preserve the overall function shape; channel flow (CF) DNS data of Re_τ = 110, 150, 300, 400, 650 from Iwamoto et al. [98], Re_τ = 1000 from Graham et al. [95], Re_τ = 5200 from Lee and Moser [90]; boundary-layer flow over a flat plate (FP) DNS data of Re_θ = 300, 670, 1410 from Spalart [92]

Interestingly, the second-order gradient of v^{+2} in Fig. 6.20, not only collapses for all the Reynolds numbers considered but also exhibits similarity to the first-order gradient of u^{+2} in shape, even though at the raw data level u^{+2} and v^{+2} profiles appear different. This points to the availability in the second-order gradient profile as well, with the same structure functions. Precisely, The zero-crossing where an inflection point of d^2v^{+2}/dy^{+2} is somewhat aft of $y^{+} \sim 15$, but the function shape on either side of it is again properly traced by the Modified Gaussian Eq. (6.10) or the Exponentially-Decaying Sinusoids Eq. (6.11).

For the Reynolds shear stress, $d^2u'v'^{+}/dy^{+2}$ in Fig. 6.21, the resulting shape from both functions is also retained except for being inverted. And that on the near-wall side, prior to the zero-crossing of $y^{+} \sim 10$, is compressed severely toward the wall.

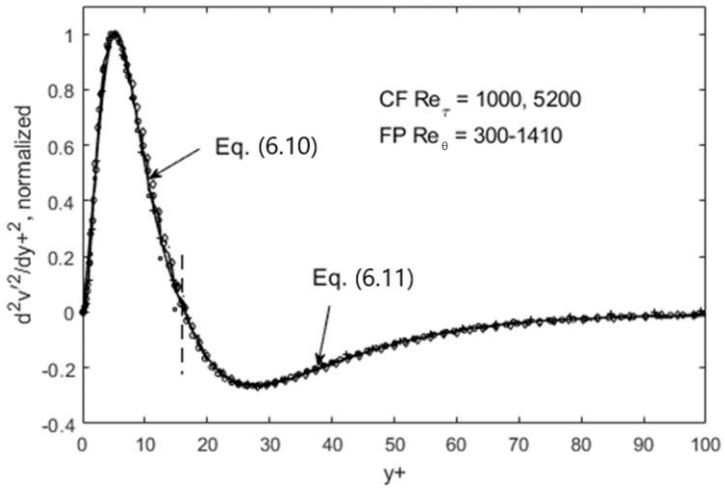

Fig. 6.20 The $d^2v'^{2+}/dy^{+2}$ profiles with gradient structure functions, ratioed by respective peak and nadir heights in left and right of zero-crossing $y^+ \sim 17$ to preserve the overall function shape; channel flow (CF) DNS data of $Re_\tau = 1000$ from Graham et al. [95], $Re_\tau = 5200$ from Lee and Moser [90]; boundary-layer flow over a flat plate (FP) DNS data of $Re_\theta = 300, 670, 1410$ from Spalart [92]

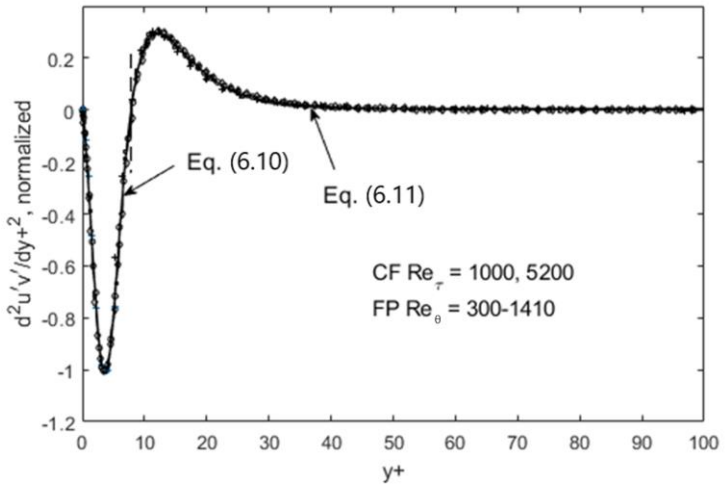

Fig. 6.21 The $d^2u'v'^{+}/dy^{+2}$ profiles with gradient structure functions, ratioed to preserve the overall function shape by respective peak and nadir heights in left and right of zero-crossing $y^+ \sim 10$; channel flow (CF) DNS data of $Re_\tau = 1000$ from Graham et al. [95], $Re_\tau = 5200$ from Lee and Moser [90]; boundary-layer flow over a flat plate (FP) DNS data of $Re_\theta = 300, 670, 1410$ from Spalart [92]

Fig. 6.22 shows the normalization constants that are used in collapsing the profiles from DNS data [90,95,98] on the unified gradient structure functions of Eq. (6.10) and Eq. (6.11), as found in Fig. 6.19, Fig. 6.20, and Fig. 6.21; the magnitudes of the peak and nadir in the profiles at different Reynolds numbers are normalized. In this way, they are closely organized as converging on a single unitary curve. Conversely, it implies that the curve can be expanded to its realization at any Reynolds number by using the normalizing factor. For example, function forms of Eq. (6.10) and Eq. (6.11) can be multiplied by the constants a_i and b_i from Fig. 6.22 to retrieve the gradient profile which is aimed at the Reynolds number.

In this light, the utility of the gradient structure functions is the same as what other self-similar profiles are capable of doing. To explain, the form of the gradient profile abiding by the structure functions Eq. (6.10) and Eq. (6.11), is feasible in the reconstruction of u'^2, v'^2, and $u'v'$ through numerical or analytical integrations.

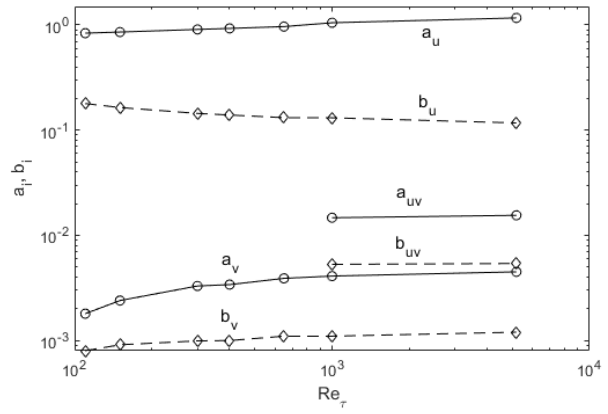

Fig. 6.22 Scaling factor for the gradient structure in channel flows, based on DNS data of Re_τ = 110, 150, 300, 400, 650 from Iwamoto et al. [98], Re_τ = 1000 from Graham et al. [95], Re_τ = 5200 from Lee and Moser [90]; (a_u, b_u) = magnitude of the (peak, nadir) for the du'^{2+}/dy^+ structure; (a_v, b_v) = magnitude of the (peak, nadir) for the $d^2v'^{2+}/dy^{+2}$ structure; (a_{uv}, b_{uv}) = magnitude of the (nadir, peak) for the $d^2u'v'^{+}/dy^{+2}$ structure

On top of that, the gradient structure functions may shed a little light on the explanation of some discernable features that are exhibited in the profile. More precisely, a secondary peak in the u'^{2+} profile starts to evolve at high Reynolds numbers. And this phenomenon has been reported by other researchers [87,113,114] with the interpretation that it is owing to some energetic feature from large scales. However, it remains still in obscurity with ambiguous concepts.

Meanwhile, the gradient structure functions may give a clue to further understating the secondary peak development. Based on the meaning of the gradient structure functions, this is attributed to a second harmonic in the du'^{2+}/dy structure, in which the harmonic sinusoidal function is capable of reproducing this high-Reynolds number effect.

With the functional form of Eq. (6.11), the relaxation in the decay rate would produce a higher amplitude for the sinusoids as shown in Fig. 6.23(a), and it is associated with the larger dissipation according to our theory; recalling that the total dissipation Φ increases with respect to the Reynolds number in Fig. 6.13, and the profiles with higher Reynolds numbers show increasing skewness in Fig. 6.12.

Since high-resolution DNS-type data for precise analyses are not feasible currently, only the experimental data at the high Reynolds numbers are examined as in Fig. 6.23(b). Even so, it finds that the synthetic second-harmonic function with a slower decay factor by Eq. (6.11) produces the secondary rising-up when integrated, as described in Fig. 6.23(b).

(a)

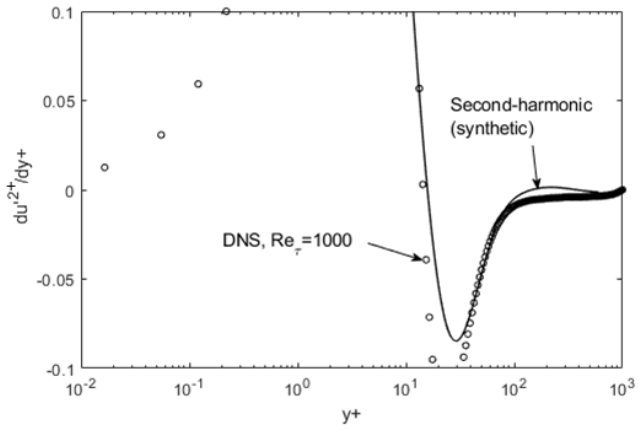

(b)

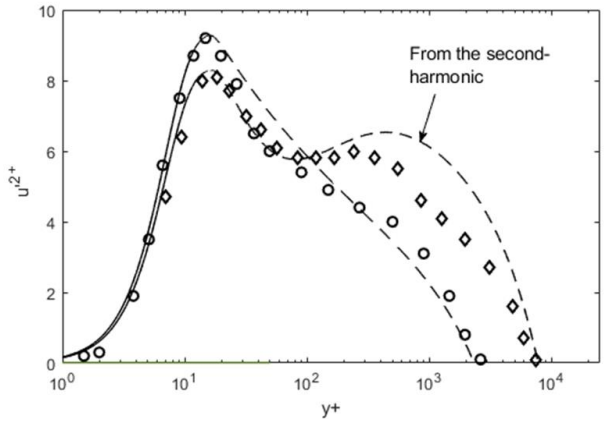

Fig. 6.23 Secondary peak structure at high Reynolds numbers; (a) the synthesized harmonic function using Eq. (6.11), DNS data at $Re_\tau = 1000$ from Graham et al. [95]; (b) integration of the function to obtain the secondary peak, in comparison with experimental data from Fernholz and Finley [115] at $Re_\theta = 5023$ in circle, $Re_\theta = 16080$ in diamond

To summarize, the Lagrangian turbulence transport framework, finds inter-related dynamics among the Reynolds stress components in terms of momentum and energy flux, outlined in Eq. (6.1), Eq. (6.2), and Eq. (6.3). And particularly the turbulence shear stress $u'v'$, is the key unknown in the RANS, outlined in Eq. (6.6) and Eq. (6.7). Based on that, the gradient structure functions can be used as the approximate solution for Eq. (6.1), Eq. (6.2), and Eq. (6.3) with the satisfaction of mutual inter-relationships among

u'^{2+}, v'^{2+} and $u'v'^{+}$ gradient. Therefore, the gradient structure functions can serve as the inverse solution that can be input into RANS for wall-bounded turbulent flows. And then, the self-similarity from the Reynolds stress gradient structure is utilizable to scale to other Reynolds numbers.

6.4 Maximum Entropy Turbulence Energy Spectra

Background

The kinetic energy distribution in turbulence, often referred to as the power spectrum, is of importance for fundamental and practical reasons. Numerous "spectral closure" has been an intensely studied topic in fluid physics. Much effort has been expended on identifying the interaction mechanisms between eddies, so-called cascade transfer. Some analytical methods for viscous incompressible flows have been developed since long ago, with turbulence energy spectrum scaling in the inertial range such as well acknowledged "$k^{-5/3}$ law" [116]. This is attributed to theoretically, the similarity transform in which turbulent flow is postulated in self-similar, i.e., homogeneous and isotropic [117], at small scales having a unique scaling exponent. And also empirically, the second-order longitudinal structure function that is observed in fully developed turbulence supports the power law [116]. Rather sophisticated methods like the EDQNM [118], i.e., Eddy Damped Quasi Normal Markovian, or one applied for two-dimensional turbulence [119] are available in the literature as examples among the numerous ones. Unfortunately, DIA [120], i.e., Direct Interaction Approximation, and EDQNM [118] tend to be complex in derivation and also the final form, hence reducing the accessibility. A more compact and easily understandable theory is preferred for practical purposes.

There have been some attempts to use the maximum entropy principle in deriving the turbulence energy spectra [121,122]. This is a cogent argument since turbulence consists of a statistically large ensemble of eddies which is expected to achieve rapid dynamical equilibrium. And essentially, it aligns with the Second Law of Thermodynamics that dictates the state of this equilibrium, wherein the partition of energy is prescribed by the maximum entropy principle [123]. The assertion of the maximum entropy principle through the Lagrange multiplier method typically results in inverse exponential distributions. Then, the remaining step is to apply associated constraints or boundary conditions, to arrive at the final energy spectral distribution [124].

There are several constraints or boundary conditions that can be stipulated within the maximum entropy formalism. The most frequently used ones are momentum and energy conservation, written in terms of some variations of the Navier-Stokes equations, such as Fourier-transformed [121] or expressed vorticity equation [122]. On the other hand, there are more obvious and easily implementable constraints from boundary conditions, such as limiting length scales with their energy contents. And the previous work has shown that by using these constraints in the maximum entropy method, the most probable energy distribution in turbulence is a lognormal form [105]. Even better, this functional form is intuitive and utilizable to parameterize the energy distribution since it involves the basic turbulence properties.

In this section, an overview of scaling properties for the spectral form derived from the previous work [105] is offered, with a demonstration of how they can be adapted in different turbulent flows. To be specific, the log-normal type of turbulence

energy spectral function, derived from the maximum entropy principle, is shown to be parameterizable in terms of a root turbulence variable including the Reynolds number. The spectral function is first compared with a number of experimental data sets, showing a very close agreement across the entire energy and length scales in wavenumber. Moreover, Energy spectra at various locations in channel flows are also reproduced using the same function, indicating its applicability wherever local equilibrium is achieved. Therefore, based on a small number of scaling parameters, the full energy spectra can be prescribed using the maximum entropy formalism.

Turbulence Energy Spectral Function Using Maximum Entropy

The energy distribution that maximizes Shannon entropy under the physical constraints can be obtained using the Lagrange multiplier method [124]. Here, the principal constraint is the conservation of turbulence energy; the kinetic energy is dissipated by a viscosity effect progressively at large wavenumbers [116]. The detailed derivation can be guided to the reference paper [106], and we start from Eq. (6.12) which is the resulting distribution function for the turbulence energy spectra.

$$E(k) = \frac{C_1}{k^4} exp\{-C_2 u'^2 - C_3 k^2 u'^2\} \qquad \text{Eq. (6.12)}$$

The constants C_1, C_2, and C_3 in Eq. (6.12) are determined from the constraints of the turbulence energy content, limiting length scales, and viscosity. For the limiting length scales, it is considered such that from the Kolmogorov dissipation length scale to

the maximum length scale that exists in the flow. We still need the kinematic scaling for $u'(k)$ in Eq. (6.12). In the Kolmogorov theory, $u'^2(k) \sim k^{-5/3}$ is obtained in the inertial subrange. In the current maximum entropy formalism, however, this is an unknown element or lack of a piece of information. The maximum entropy principle gives the most probable energy distribution under the given physical constraints, but it does not produce unknown information. Thus, the missing piece of information needs to be supplemented from observational data, and Eq. (6.12) provides a framework for testing various kinematic scaling of $u'(k)$.

To deduce the empirical form for $u'(k)$, several attempts are made. For example, Fig. 6.24 shows the plot of $u'(k) \sim k^{-1/3}$ which is comparable with a log form of k^{-1}, precisely the expression in $u'(k) \sim m - \log(k)$. The m is a parameter associated with shifting and heightening for the spectra as it prescribes the spectral location and magnitude. Note that it is within the exponential function of E(k). The η denotes a dissipation length scale associated with the Kolmogorov length scale of $(\nu^3\varepsilon^{-1})^{1/4}$, and normalizes k in the expression of a nondimensional form of wavenumber, $k\eta$.

In Fig. 6.25, the comparison of the power spectra E(k) from Eq. (6.12) to the observational data [125] is made, as while applying the various empirical forms of $u'(k)$ into the E(k). And it shows the E(k), generated using the inverse logarithmic expression, i.e., marked as a with the plot, gives the best consistency with the experimental data [125]. Therefore, the inverse logarithmic scaling for $u'(k)$ appears most plausible to apply along with Eq. (6.12) for the time being, although subjecting to further experimental verifications. The data is measured with Taylor microscale based Reynolds number, $Re_\lambda = (u')_{rms}\,\lambda/\nu$ where $\lambda = (15\nu\,\overline{u'^2}\,/\varepsilon)^{1/2}$.

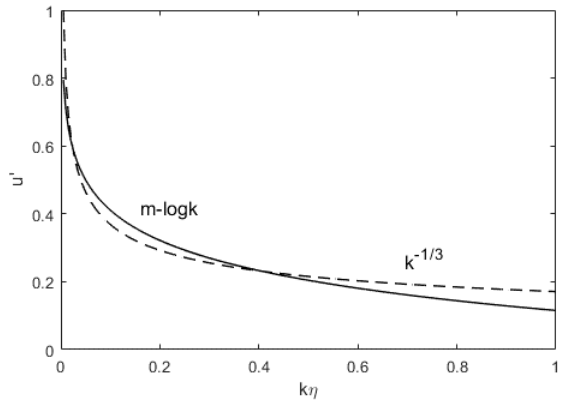

Fig. 6.24 Comparison of u′(k) format as u′(k) ~ m − log(k) with u′(k) ~ $k^{-1/3}$

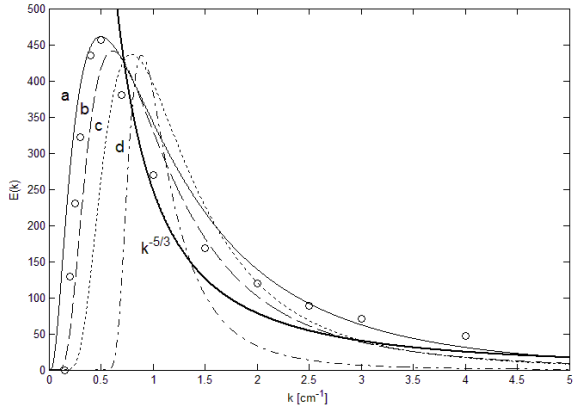

Fig. 6.25 Various u′(k) scaling used in Eq. (6.12) to generate the turbulence energy spectra; a. u′(k) = m − log(k), b. $k^{-1/2}$, c. $k^{-1/3}$, d. k^{-3}; bold line is the Kolmogorov's $k^{-5/3}$ law in the inertial subrange; symbol is data from Comte-Bellot and Corrsin [125] at Re_λ = 71.6. Note the lognormal shape from the data plot when graphed in linear scale axes

Fig. 6.26 demonstrates the efficacy of this lognormal form in reproducing the observed turbulence spectra, in which the agreement between Eq. (6.12) and data is quite good for a wide range of Reynolds numbers. Furthermore, the spectral coverage encompasses the entire energy as well as the wavenumber ranges, starting from the energy-generating to the Kolmogorov dissipation scale. There is no restriction either

theoretically or pragmatically to be within the so-called “inertial range”, as the maximum entropy principle produces the full energy state across the entire wavenumber domain. At the lower energy-generating wave number, the distribution is truncated since the mode of turbulence production at these scales differ from one experiment to another, and it has not been input as a constraint.

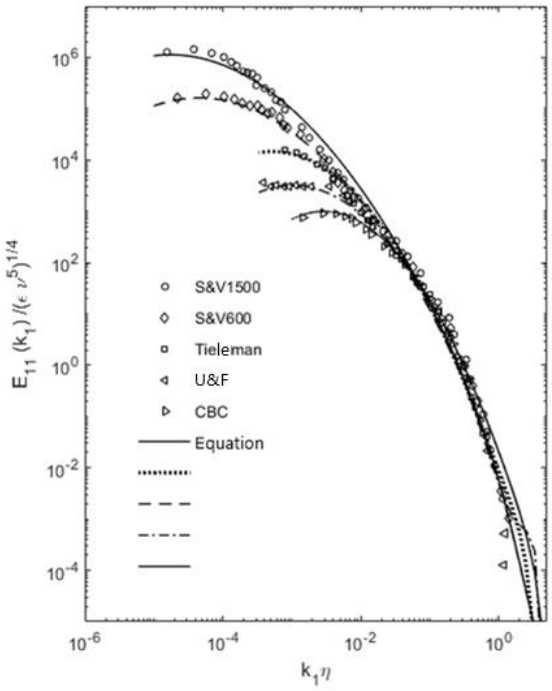

Fig. 6.26 Comparison of maximum entropy spectra from Eq. (6.12) with experimental data [125–128] for normalized longitudinal velocity spectrum of $Re_\lambda = 71.6 \sim 1500$. The data references are listed in Table 6.2 with details

The final form of Eq. (6.12) may be referred to as a lognormal-type distribution in which it is truncated at k_{min} and with the k^{-4} modifier in place of k^{-1} in the conventional lognormal distribution function, e.g., $f(k) \sim k^{-1} \exp\{-[\log(k) - \mu]^2\}$ where μ is mean

parameter. Note that the similar functional format between the conventional one and Eq. (6.12) in which if $u'(k) \sim m - \log(k)$ is input then $u'^2(k) \sim [\log(k) - m]^2$, as leading to $E(k) \sim k^{-4} \exp\{-[\log(k) - m]^2\}$. Hence, it comes by that called a lognormal-type distribution.

As a matter of fact, various k^n type of scalings, e.g., the most prominent one is $n = -5/3$ [116], are local or regional tangents to the lognormal distributions. Although for large Reynolds numbers, $n = -5/3$ tangent overlaps with the full E(k) over a good range of scales, however, it is a localized approximation. Conversely, it implies that unless the Reynolds number is very high, the so-called inertial range would be only a small portion of the entire energy spectrum, as being missed off large sections near the energy-containing and dissipation scales from the full picture.

The lognormal form of Eq. (6.12) is beneficial in that it makes straight forward to parameterize the distribution functions. For example, the m is the logarithmic mean, which in this case corresponds to the $\log(k_m)$ where k_m is the wavenumber at the peak energy scale, i.e., $1/k_m \sim L$ is the energy-generating length scale. Given some variations in the energy generation processes, we write as $m \sim \log(k_m)$.

The C_1 is the amplitude parameter, proportional to E_{max}. Considering that various experimental conditions exist or sometimes are unclear in reference papers, the simpler form is taken as $C_1 \sim E_{max}$.

The C_2 is the width parameter, inversely proportional to the logarithmic variance. Because the current form is not normalized, but instead vertically scaled by $C_1 \sim E_{max}$ in energy magnitude, C_2 has a large influence on the energy scale too. In other words, small C_2 is corresponding to a more gradual decrease in E(k) slope, leading to stretching out the

k range farther with a larger amount of total content of E. Consequently at large Reynolds numbers, both the width and height of the energy spectra are increased by decreasing C_2. To be specific, when the Reynolds number increases C_2 has ~ $1/(Re)^p$ dependence, with the exponent $p \sim k_m$. For this reason, C_2 is the key parameter in the use of maximum-entropy turbulence energy distribution.

Finally, the C_3 is the viscosity parameter, $C_3 \sim \nu$, setting the maximum wavenumber and causing rapid dissipation close to this scale. It only modifies the spectral form near the dissipation range noting that C_3 is multiplied by k^2, and controls the rate of descent with rapidly depleting kinetic energy.

Thus, k_m, E_{max}, Re_λ, k_{max}, and ν furnish the parameters to prescribe the full turbulence energy spectra over the correspondent wavenumbers. The function parameters for the plots in Fig. 6.26 are listed in Table 6.2.

Table 6.2 Parameters of the energy spectra for various data sets

Re_λ	$E_{max} / (\varepsilon\nu^5)^{1/4}$	$(k\eta)_{@Emax}$	$(k\eta)_{max}$	C_2	m	ν	Reference
71.6	878	0.00439	1.164	0.315	0.5	0.0225	CBC: Comte-Bellot and Corrsin [125]
132	3183	0.001283	1.229	0.25	1.12	0.032	U & F: Uberoi and Freymuth [126]
282	15849	0.000777	0.685	0.25	0.45	0.01	Tieleman [127]
600	199000	0.0000578	1.429	0.16	2.5	0.05	S & V: Saddoughi and Veeravalli [128]
1500	1446000	0.0000379	1.2	0.1475	2.5	0.05	S & V: Saddoughi and Veeravalli [128]

In Fig. 6.27 more recent data from LES by Kang et al. [129] is examined, in which the evolution of the energy spectrum in decaying turbulence is observed. Eq.

(6.12) follows this decay with a change in only the parameter C_2, meanwhile, all other constants are kept without change. The spectra tend to merge near the dissipation range, while diverging at the low wavenumbers as the Reynolds number decreases downstream. This spectral characteristic is reproduced by Eq. (6.12) with only a small variation in C_2 from 0.135 at Re_λ = 716 to 0.140 at Re_λ = 626. The current spectra by Eq. (6.12) overestimate the data in the range of $k_1\eta$ ~ 0.002 to 0.05. Strictly straight or triangular probability distribution on logarithmic axes is seldom observed except in the inertial turbulence range, as energy distributions in nature tend to be of exponential decay found in Maxwell-Boltzmann distribution, or lognormal-type found in Planck distribution, that depending on the physical constraints. During a single experiment, it is also difficult to cover larger spans of the Reynolds number. Nonetheless, the lognormal-type distribution of Eq. (6.12) exhibits feasible parametric variations to apply, as it mimics the Reynolds number dependence seen in Fig. 6.27; recall that $C_2 \sim 1/(Re)^p$.

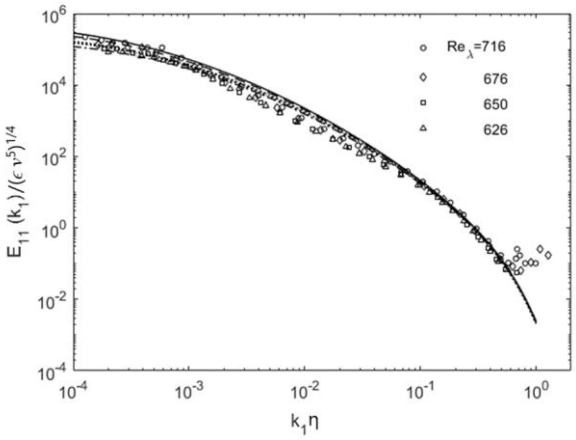

Fig. 6.27 Comparison of the turbulence energy spectra with LES data of Kang et al. [129] for decaying turbulence. The C_2 is varied from 0.135 at Re_λ = 716 to 0.140 at Re_λ = 626, with fixed for C_1, m, and C_3 in Eq. (6.12); data in symbols and the equation in lines

Likewise, it has merit in terms of complementing the observed k^n scaling exponents which tended to vary across different experiments. For example, in atmospheric turbulence, the exponent n goes from -3 to -5/3 in the inertial range as seen in Fig. 6.28, when the flow transition from two- to three-dimension, e.g., synoptic scales to mesoscale [130,131]. This change in the slope is realizable with Eq. (6.12) when the width of the spectra is broadened, i.e., with decreased C_2. More specifically, Fig. 6.28 shows that reducing C_2 from 0.1 to 0.034 in Eq. (6.12) can replicate the transition of energy spectra from two- to three-dimension for zonal wind, as compared with large-scale atmospheric data [131]. For meridional and potential temperature spectra, similar transitions are found when $C_2 = 0.1 \rightarrow 0.05$ and $0.1625 \rightarrow 0.05$, respectively. The dimensional transition at these scales involves a substantial change in C_2.

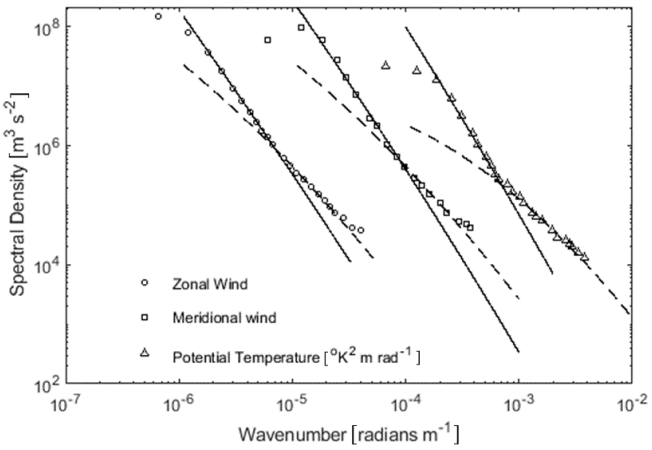

Fig. 6.28 Transition of the energy spectra from two- to three-dimension with Eq. (6.12) as solid and dash line respectively; synoptic and sub synoptic mesoscale data as symbols are from Nastrom and Gage [131]

The lognormal behavior of turbulence energy spectra is as well evident in inhomogeneous flows such as channel flows in Fig. 6.29. The power spectra DNS data [97] for Re_τ = 180, 395, and 590 are taken at various heights from the wall, and the current lognormal form follows all to an acceptable degree when compared with the data shown in Fig. 6.29. Current maximum-entropy distribution replicates the observed spectra quite well, except near the wall in the mid-wavenumber range, i.e., $k_x/k_{max} \sim 10^{-1}$, where Eq. (6.12) underestimates from the data. Also, at low Reynolds number Re_τ = 180, there is a small discrepancy at low wavenumbers. Except that, the overall reconstruction of the energy spectra using Eq. (6.12) is good as in Fig. 6.29. It can be interpreted such that local equilibrium is achieved at high Reynolds numbers so the state of maximum entropy exists, indicating that the lognormal energy spectra form is as well applicable to the inhomogeneous flows. Moreover, lognormal behavior is dominant across nearly the entire range of scales, reaching far beyond the so-called inertial range.

Consequently, the extent of the current concept is viable to even inhomogeneous flows at sufficiently high Reynolds numbers, implying that our concept has universal applicability in globally and also locally equilibrated turbulence.

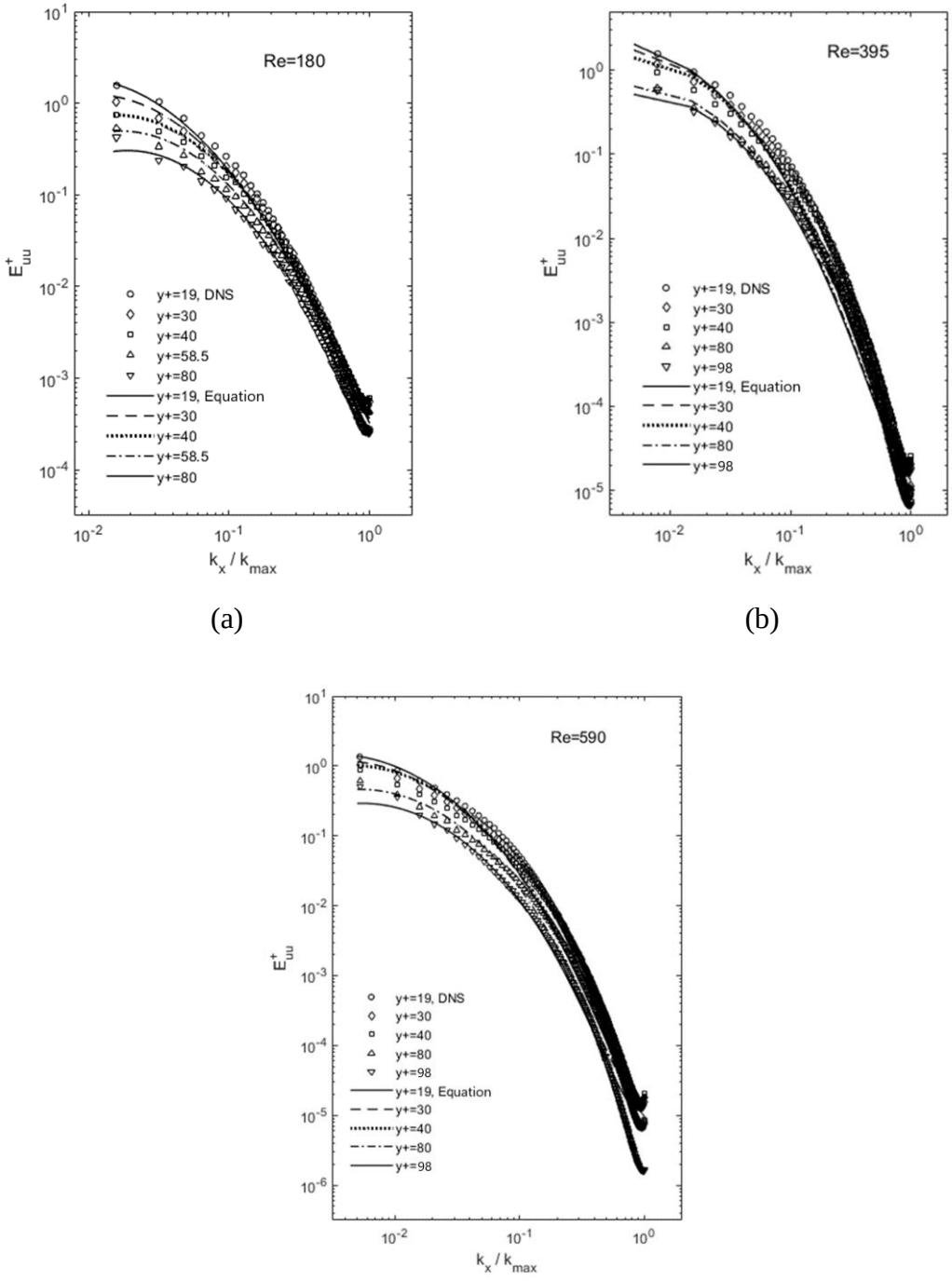

(a) (b)

(c)

Fig. 6.29 Comparison of the turbulence energy spectra with DNS data of Moser et al. [97] at various distances y^+ from the wall for channel flows, with (a) $Re_\tau = 180$, (b) $Re_\tau = 395$, and (c) $Re_\tau = 590$; Eq. (6.12) as lines are compared with DNS data as symbols

6.5 Chapter Summary

The gradient of u'^2 and v'^2 are key terms in the expression of Reynolds shear stress $u''v''$ from Eq. (6.1). With the computed $u''v''$ profile, in turn, that can be used to generate the mean velocity profile. And we have shown that the derived profiles are within reasonable margins of error relative to the DNS data.

The mean velocity profiles can be obtained from RANS, in conjunction with the scaled Reynolds shear stress profile or transport equation set. Since the pressure force term in RANS is linear, while $u''v''$ is highly nonlinear, no single function, either linear or logarithmic, appears likely to track the observed mean velocity profile across the entirety of the boundary layers. Instead, since the Reynolds shear stress is fairly well prescribed by the current scaling and dynamical formalism, a simple combination of the pressure, viscous, and $u''v''$ facilitates determining the mean velocity in wall-bounded flows.

The global effect of Reynolds number is to increase the maximum allowable total dissipation Φ, while u'^2 and v'^2 after being normalized by the energy scale u_τ^2 must contain a fixed total kinetic energy E. The route for elevating Φ is by skewing the u'^2 spatial distribution. However, u'^2 and v'^2 transports are internally constrained by the flux terms in Eq. (6.3) and Eq. (6.2), and also must follow continuous and smooth functional progressions.

And we have shown that the gradient profile of these variables has self-similarity, with which they perform such interior dynamics via the gradient transport. The self-similarity in the root turbulence variables is found in the "dissipation space" using d/dy^+ and d^2/dy^{+2} operations. The fact that u'^2 and v'^2 transports are dictated by

energy and momentum fluxes respectively, is a potential cause of the different dissipation scaling, such as first- and second-order gradient, $du^{\prime 2+}/dy^{+}$ and $d^2v^{\prime 2+}/dy^{+2}$.

Making use of these operations neatly folds the profiles at various Reynolds numbers onto a single curve. Meanwhile, a normalized gradient structure form can serve as a template to expand to other Reynolds numbers. The ordered gradient structure function from Table 6.1 is made with the two distinctive functions Eq. (6.10) and Eq. (6.11), that allows for reconstructive tasks at any Reynolds numbers. The scalability has been utilized from the turbulence structure in this way, with the validation on wall-bounded flows through a comparison study with experimental data from others. Therefore, it proves that these scaling characteristics along with the transport equations of Eq. (6.1), Eq. (6.2), and Eq. (6.3) furnish useful insights and computability for the interior dynamics of turbulent channel flows.

Turbulence energy distribution derived from existing spectral closure models like DIA or EDQNM, includes some approximated transport modeling functions for eddy interaction. By the way, energy transfer is a natural phenomenon prevalent existing in other systems too, such as during molecular collisions or thermal energy variations through blackbody radiation. Hence, a more general approach would be useful to explain the turbulence energy distribution.

To portray turbulent flows, energetic particles or turbulent eddies will organize themselves in an order that maximizes entropy. In this light, derivation for the turbulence energy or power spectra would be possible under the maximum-entropy formalism. This route does not necessitate complex eddy interaction terms

since the distribution is representative of the final statistical state. Plus, this approach is referred to as the method of most probable distribution, representing a universally observable behavior in energetic systems. In this way, the complex details of the energetic interactions can be circumvented, essentially through the use of the maximum entropy principle, as seen in Maxwell-Boltzmann or Planck distribution function.

The postulated lognormal-type distribution is validated through the comparison study with experimental data from various reference papers. Mostly, those reference data resort to showing punctuated $E(k) \sim k^n$, that is n = 2 to 4 for the ascending portion while n = -5/3, -3, or near, for the descending portion, which depending on the dimensionality and type of the turbulent flow. On the other hand, lognormal functions trace a parabola in log-log scale axes, thereby any one of these tangents can be observed without having to describe in segments of a range of scales.

Given observable constraints, such as the cutoff at the energy-generating length scale and width of the spectrum as a function of the Reynolds number, the distribution form can be parameterized in the lognormal function. And we have demonstrated that through this parametric scaling, full energy spectra can be graphed based on input parameters, such as Reynolds number, viscosity, energy-producing length scales, and its containing energy scale, for homogeneous and some inhomogeneous turbulent flows. While a limited applicable range is expected under k^n scaling, the current theoretical results, by the way, cover the observed energy spectra over the entire range of length and energy scales.

The parameters are deployed under the following considerations. When the Reynolds number increases, the range of length scales increases leading to the widening of the spectra through the C_2 term in Eq. (6.12). The C_2 also raises the overall energy spectrum magnitude because there is a linkage effect at high Reynolds numbers. The peak energy level, however, is determined by the total energy generation rate, typically estimated as U^3/L. Therefore, the peak energy level for different turbulence geometries needs to be adjusted with the C_1 in Eq. (6.12). The bending of the spectra at high wavenumbers due to viscosity is achieved by maneuvering the C_3 in Eq. (6.12). These attributes of the current study are worth consideration and should be further explored.

Comments on the Turbulence Theory Relative to the Existing Models

There is growing evidence against the eddy viscosity concept in turbulence models despite their relative success in simple flow geometries. From a simple physical standpoint, however, turbulent eddies interact strongly at all scales, and there is no reason to believe that the viscosity concept based on elastic molecular collisions is applicable in turbulent flows. By the way, the current theory is based on a Lagrangian analysis by applying the conservation equations to a coordinate frame moving at the local mean velocities. This results in a set of transport equations relating to the Reynolds stress components. Thus, the physics of turbulent flows in wall-bounded and other flows is revealed in this work, amenable to mathematical prescriptions without ad-hoc modeling.

REFERENCES

[1] Landau, L. D., and Lifshitz, E. M., 1980, *Course of Theoretical Physics*, Elsevier, https://doi.org/10.1016/B978-0-08-023039-9.50007-X.

[2] Rayleigh, Lord, 1878, "On the Instability of Jets," Proc. London Math. Soc., **14**, pp. 4–12.

[3] Weber, C., 1931, "Breakup of a Liquid Jet."

[4] Taylor, G., 1950, "The Instability of Liquid Surfaces When Accelerated in a Direction Perpendicular to Their Planes. I," Proc. R. Soc. London. Ser. A. Math. Phys. Sci., **201**(1065), pp. 192–196.

[5] Sterling, A. M., and Sleicher, C. A., 1975, "The Instability of Capillary Jets," J. Fluid Mech., **68**(3), pp. 477–495.

[6] Reitz, R. D., and Bracco, F. V., 1982, "Mechanism of Atomization of a Liquid Jet," Phys. Fluids, **25**(10), pp. 1730–1742.

[7] Savart, F., 1833, "Suite Du Mémoire Sur Le Choc D´une Veine Liquide Lancée Contre Un Plan Circulaire," Ann. Chim. Phys., **54**, pp. 113–145.

[8] Dombrowski, N., and Johns, W. R., 1963, "The Aerodynamic Instability and Disintegration of Viscous Liquid Sheets," Chem. Eng. Sci., **18**(7), p. 470.

[9] Faeth, G. M., Hsiang, L.-P., and Wu, P.-K., 1995, "Structure and Breakup Properties of Sprays," Int. J. Multiph. Flow, **21**, pp. 99–127.

[10] Huh, K. Y., Lee, E., and Koo, J., 1998, "Diesel Spray Atomization Model Considering Nozzle Exit Turbulence Conditions," At. Sprays, **8**(4), pp. 453–469.

[11] O'Rourke, P. J., and Amsden, A. A., 1987, "The TAB Method for Numerical Calculation of Spray Droplet Breakup," *SAE Technical Paper 872089*.

[12] Reitz, R. D., 1987, "Mechanisms of Atomization Processes in High-Pressure Vaporizing Sprays," At. Spray Technol., **3**, pp. 309–337.

[13] Patterson, M. A., and Reitz, R. D., 1998, "Modeling the Effects of Fuel Spray Characteristics on Diesel Engine Combustion and Emission," *SAE Technical Papers*, pp. 27–43.

[14] Tanner, F. X., 2003, "A Cascade Atomization and Drop Breakup Model for the Simulation of High-Pressure Liquid Jets," *SAE Technical Papers*, pp. 1352–1366.

[15] Sirignano, W. A., and Mehring, C., 2000, “Review of Theory of Distortion and Disintegration of Liquid Streams,” Prog. Energy Combust. Sci., **26**(4), pp. 609–655.

[16] Senecal, P. K., Schmidt, D. P., Nouar, I., Rutland, C. J., Reitz, R. D., and Corradini, M. L., 1999, “Modeling High-Speed Viscous Liquid Sheet Atomization,” Int. J. Multiph. Flow, **25**(6–7), pp. 1073–1097.

[17] Schmidt, D. P., Nouar, I., Senecal, P. K., Rutland, J., Martin, J. K., Reitz, R. D., and Hoffman, J. A., 1999, “Pressure-Swirl Atomization in the near Field,” SAE Trans., **108**, pp. 471–484.

[18] Shinjo, J., 2018, “Recent Advances in Computational Modeling of Primary Atomization of Liquid Fuel Sprays,” Energies, **11**(11), p. 2971.

[19] Herrmann, M., 2010, “A Parallel Eulerian Interface Tracking/Lagrangian Point Particle Multi-Scale Coupling Procedure,” J. Comput. Phys., **229**(3), pp. 745–759.

[20] Ling, Y., Zaleski, S., and Scardovelli, R., 2015, “Multiscale Simulation of Atomization with Small Droplets Represented by a Lagrangian Point-Particle Model,” Int. J. Multiph. Flow, **76**, pp. 122–143.

[21] Herrmann, M., 2010, “Detailed Numerical Simulations of the Primary Atomization of a Turbulent Liquid Jet in Crossflow,” J. Eng. Gas Turbines Power, **132**(6), pp. 1–10.

[22] Vallet, A., Burluka, A. A., and Borghi, R., 2001, “Development of a Eulerian Model for the Atomization of a Liquid Jet,” At. Sprays, **11**(6), pp. 619–642.

[23] Lebas, R., Menard, T., Beau, P. A., Berlemont, A., and Demoulin, F. X., 2009, “Numerical Simulation of Primary Break-up and Atomization: DNS and Modelling Study,” Int. J. Multiph. Flow, **35**(3), pp. 247–260.

[24] Navarro-Martinez, S., 2014, “Large Eddy Simulation of Spray Atomization with a Probability Density Function Method,” Int. J. Multiph. Flow, **63**, pp. 11–22.

[25] Saeedipour, M., Pirker, S., Bozorgi, S., and Schneiderbauer, S., 2016, “An Eulerian–Lagrangian Hybrid Model for the Coarse-Grid Simulation of Turbulent Liquid Jet Breakup,” Int. J. Multiph. Flow, **82**, pp. 17–26.

[26] Umemura, A., and Shinjo, J., 2018, “Detailed SGS Atomization Model and Its Implementation to Two-Phase Flow LES,” Combust. Flame, **195**, pp. 232–252.

[27] Ketterl, S., and Klein, M., 2018, "A-Priori Assessment of Subgrid Scale Models for Large-Eddy Simulation of Multiphase Primary Breakup," Comput. Fluids, **165**, pp. 64–77.

[28] Kim, D., and Moin, P., 2020, "Subgrid-Scale Capillary Breakup Model for Liquid Jet Atomization," Combust. Sci. Technol., **192**(7), pp. 1334–1357.

[29] Lefebvre, A. H., and McDonell, V. G., 2017, *Atomization and Sprays*, CRC Press, Second edition. | Boca Raton : Taylor & Francis, CRC Press, 2017.

[30] Bachalo, W., 2000, "Spray Diagnostics for the Twenty-First Century," At. Sprays, **10**(3–5), pp. 439–474.

[31] Linne, M., 2013, "Imaging in the Optically Dense Regions of a Spray: A Review of Developing Techniques," Prog. Energy Combust. Sci., **39**(5), pp. 403–440.

[32] Moon, S., Liu, Z., Gao, J., Dufresne, E., Fezzaa, K., Wang, J., Xie, X., and Lai, M.-C., 2010, "Ultrafast X-Ray Phase-Contrast Imaging of High-Speed Fuel Sprays from a Two-Hole Diesel Nozzle," *22nd Annual Conference on Liquid Atomization and Spray Systems,ILASS Americas*, Cincinnati, OH.

[33] Schmidt, J. B., Schaefer, Z. D., Meyer, T. R., Roy, S., Danczyk, S. A., and Gord, J. R., 2009, "Ultrafast Time-Gated Ballistic-Photon Imaging and Shadowgraphy in Optically Dense Rocket Sprays," Appl. Opt., **48**(4), p. B137.

[34] Charalampous, G., Hadjiyiannis, C., Hardalupas, Y., and Taylor, A. M. K. P., 2010, "Measurement of Continuous Liquid Jet Length in Atomizers with Optical Connectivity, Electrical Conductivity and High-Speed Photography Techniques," *23rd Annual Conference on Liquid Atomization and Spray Systems, ILASS—Europe*, Brno, Czech Republic.

[35] Berrocal, E., Kristensson, E., Hottenbach, P., Aldén, M., and Grünefeld, G., 2012, "Quantitative Imaging of a Non-Combusting Diesel Spray Using Structured Laser Illumination Planar Imaging," Appl. Phys. B Lasers Opt., **109**(4), pp. 683–694.

[36] Mugele, R. A., and Evans, H. D., 1951, "Droplet Size Distribution in Sprays," Ind. Eng. Chem., **43**(6), pp. 1317–1324.

[37] Babinsky, E., and Sojka, P. E., 2002, "Modeling Drop Size Distributions," Prog. Energy Combust. Sci., **28**(4), pp. 303–329.

[38] Paloposki, T., 1994, "Drop Size Distributions in Liquid Sprays," Acta Polytech. Scand. Mech. Eng. Ser., **36:114**.

[39] Dumouchel, C., 2009, “The Maximum Entropy Formalism and the Prediction of Liquid Spray Drop-Size Distribution,” Entropy, **11**(4), pp. 713–747.

[40] Sellens, R. W., and Brzustowski, T. A., 1986, “A Simplified Prediction of Droplet Velocity Distributions in a Spray,” Combust. Flame, **65**(3), pp. 273–279.

[41] Li, X., and Tankin, R., 1987, “Droplet Size Distribution: A Derivation of a Nukiyama-Tanasawa Type Distribution Function,” Combust. Sci. Technol., **56**(1), pp. 65–76.

[42] Sivathanu, Y. R., and Gore, J. P., 1993, “A Discrete Probability Function Method for the Equation of Radiative Transfer,” J. Quant. Spectrosc. Radiat. Transf., **49**(3), pp. 269–280.

[43] Sovani, S. D., Sojka, P. E., and Sivathanu, Y. R., 1999, “Prediction of Drop Size Distributions from First Principles: The Influence of Fluctuations in Relative Velocity and Liquid Physical Properties,” At. Sprays, **9**(2), pp. 133–152.

[44] Williams, F. A., 1958, “Spray Combustion and Atomization,” Phys. Fluids, **1**(6), p. 541.

[45] Laurent, F., Massot, M., and Villedieu, P., 2004, “Eulerian Multi-Fluid Modeling for the Numerical Simulation of Coalescence in Polydisperse Dense Liquid Sprays,” J. Comput. Phys., **194**(2), pp. 505–543.

[46] Lee, T.-W., and Robinson, D., 2010, “Calculation of the Drop Size Distribution and Velocities from the Integral Form of the Conservation Equations,” Combust. Sci. Technol., **183**(3), pp. 271–284.

[47] Lee, T.-W., Lee, J. Y., and Do, Y. H., 2012, “Momentum Effects on the Spray Drop Size, Calculated from the Integral Form of the Conservation Equations,” Combust. Sci. Technol., **184**(3), pp. 434–443.

[48] Lee, T.-W., and Ryu, J.-H., 2014, “Analyses of Spray Break-up Mechanisms Using the Integral Form of the Conservation Equations,” Combust. Theory Model., **18**(1), pp. 89–100.

[49] Lee, T.-W., and An, K., 2016, “Quadratic Formula for Determining the Drop Size in Pressure-Atomized Sprays with and without Swirl,” Phys. Fluids, **28**(6), p. 063302.

[50] Lee, T.-W., Park, J. E., and Kurose, R., 2018, “Determination of the Drop Size during Atomization of Liquid Jets in Cross Flows,” At. Sprays, **28**(3), pp. 241–254.

[51] Lee, T.-W., and Park, J. E., 2019, “Determination of the Drop Size During Air-Blast Atomization,” J. Fluids Eng., **141**(12), pp. 1–6.

[52] Lee, T. W., Park, J. E., Bellerova, H., Hnizdl, M., and Raudensky, M., 2020, “Momentum Analyses for Determination of Drop Size and Distributions during Spray Atomization,” At. Sprays, **30**(2), pp. 97–109.

[53] Bellerova, H., Luks, T., Pohanka, M., Resl, O., and Raudensky, M., 2019, *Cooling Characteristics of Air-Mist Nozzles for Continuous Casting, Heat Transfer and Fluid Flow Laboratory Report*, Brno, Czech Republic.

[54] Lee, T.-W., Greenlee, B., and Park, J. E., 2021, “Computational Protocol for Spray Flow Simulations Including Primary Atomization,” J. Fluids Eng., **143**(3), p. 031402.

[55] Lee, T.-W., Greenlee, B., Park, J. E., Bellerova, H., and Raudensky, M., 2021, “Computational Simulations of Liquid Sprays in Crossflows With an Algorithmic Module for Primary Atomization,” J. Eng. Gas Turbines Power, **143**(6), p. 061020.

[56] Reitz, R. D., and Beale, J. C., 1999, “Modeling Spray Atomization with the Kelvin- Helmholtz/Rayleigh-Taylor Hybrid Model,” At. Sprays, **9**(6), pp. 623–650.

[57] Elkotb, M. M., 1982, “Fuel Atomization for Spray Modelling,” Prog. Energy Combust. Sci., **8**(1), pp. 61–91.

[58] Tratnig, A., and Brenn, G., 2010, “Drop Size Spectra in Sprays from Pressure-Swirl Atomizers,” Int. J. Multiph. Flow, **36**(5), pp. 349–363.

[59] Shimizu, M., Arai, M., and Hiroyasu, H., 1984, “Measurements of Breakup Length in High Speed Jet,” Bull. JSME, **27**(230), pp. 1709–1715.

[60] Chen, Y., Wagner, J. L., Farias, P. A., DeMauro, E. P., and Guildenbecher, D. R., 2018, “Galinstan Liquid Metal Breakup and Droplet Formation in a Shock-Induced Cross-Flow,” Int. J. Multiph. Flow, **106**, pp. 147–163.

[61] Eroglu, H., and Chigier, N., 1991, “Initial Drop Size and Velocity Distributions for Airblast Coaxial Atomizers,” J. Fluids Eng., **113**(3), pp. 453–459.

[62] Ruff, G. A., Bernal, L. P., and Faeth, G. M., 1991, “Structure of the Near-Injector Region of Nonevaporating Pressure-Atomized Sprays,” J. Propuls. Power, **7**(2), pp. 221–230.

[63] Martinez, G. L., Magnotti, G. M., Knox, B. W., Genzale, C. L., Matusik, K. E., Duke, D. J., Powell, C. F., and Kastengren, A. L., 2017, "Quantification of Sauter Mean Diameter in Diesel Sprays Using Scattering-Absorption Extinction Measurements," *ILASS-Americas 29th Annual Conference on Liquid Atomization and Spray Systems,* Atlanta, GA.

[64] Lee, C. S., and Park, S. W., 2002, "An Experimental and Numerical Study on Fuel Atomization Characteristics of High-Pressure Diesel Injection Sprays," Fuel, **81**(18), pp. 2417–2423.

[65] Marchione, T., Allouis, C., Amoresano, A., and Beretta, F., 2007, "Experimental Investigation of a Pressure Swirl Atomizer Spray," J. Propuls. Power, **23**(5), pp. 1096–1101.

[66] Eslamian, M., Amighi, A., and Ashgriz, N., 2014, "Atomization of Liquid Jet in High-Pressure and High-Temperature Subsonic Crossflow," AIAA J., **52**(7), pp. 1374–1385.

[67] Song, J., Cary Cain, C., and Guen Lee, J., 2015, "Liquid Jets in Subsonic Air Crossflow at Elevated Pressure," J. Eng. Gas Turbines Power, **137**(4), pp. 1–12.

[68] Rachner, M., Becker, J., Hassa, C., and Doerr, T., 2002, "Modelling of the Atomization of a Plain Liquid Fuel Jet in Crossflow at Gas Turbine Conditions," Aerosp. Sci. Technol., **6**(7), pp. 495–506.

[69] Mashayek, A., 2006, "Experimental and Numerical Study of Liquid Jets in Crossflow," M.Sc. thesis, University of Toronto, Toronto, ON, Canada.

[70] Kotrbacek, P., Bellerova, H., Luks, T., and Raudensky, M., 2021, "Heat Transfer Correlations for Secondary Cooling in Continuous Casting," steel Res. Int., **92**(3), p. 2000465.

[71] Chabicovsky, M., Kotrbacek, P., Bellerova, H., Kominek, J., and Raudensky, M., 2020, "Spray Cooling Heat Transfer above Leidenfrost Temperature," Metals (Basel)., **10**(9), p. 1270.

[72] Salazar, E., 2020, "Air-Mist Spray Model Development in Steel Secondary Cooling Process," M.Sc. thesis, Purdue University, West Lafayette, IN.

[73] de León B., M., and Castillejos E., A. H., 2015, "Physical and Mathematical Modeling of Thin Steel Slab Continuous Casting Secondary Cooling Zone Air-Mist Impingement," Metall. Mater. Trans. B, **46**(5), pp. 2028–2048.

[74] Minchaca M, J. I., Castillejos E, A. H., and Acosta G, F. A., 2011, "Size and Velocity Characteristics of Droplets Generated by Thin Steel Slab Continuous Casting Secondary Cooling Air-Mist Nozzles," Metall. Mater. Trans. B, **42**(3), pp. 500–515.

[75] Gorokhovski, M., and Herrmann, M., 2008, "Modeling Primary Atomization," Annu. Rev. Fluid Mech., **40**(1), pp. 343–366.

[76] Lee, T.-W., Greenlee, B., Park, J. E., Bellerova, H., and Raudensky, M., 2020, "A Computational Protocol for Simulation of Liquid Jets in Crossflows with Atomization," At. Sprays, **30**(5), pp. 319–330.

[77] "Particle Master," LaVision [Online]. Available: http://www.armansg.com/Editor/UploadFiles/Lavision/BR_ParticleMaster.pdf.

[78] Veron, F., 2015, "Ocean Spray," Annu. Rev. Fluid Mech., **47**(1), pp. 507–538.

[79] Andreas, E. L., 2004, "Spray Stress Revisited," J. Phys. Oceanogr., **34**(6), pp. 1429–1440.

[80] Veron, F., Hopkins, C., Harrison, E. L., and Mueller, J. A., 2012, "Sea Spray Spume Droplet Production in High Wind Speeds," Geophys. Res. Lett., **39**(16), https://doi.org/10.1029/2012GL052603.

[81] Andreas, E. L., Edson, J. B., Monahan, E. C., Rouault, M. P., and Smith, S. D., 1995, "The Spray Contribution to Net Evaporation from the Sea: A Review of Recent Progress," Boundary-Layer Meteorol., **72**(1–2), pp. 3–52.

[82] Chen, Y., Starner, S. H., and Masri, A. R., 2001, "Combined PDA / LIF Measurements in Simple , Evaporating Turbulent Spray Jets," *Fourteenth Australasian Fluid Mechanics Conference*, B.B. Dally, ed., Causal Productions, Adelaide, Australia, pp. 267–270.

[83] Chen, Y.-C., Strner, S. H., and Masri, A. R., 2002, "Characteristics of Turbulent Spray Combustion in a Piloted Jet Flame Burner," Proc. Combust. Inst., **29**(1), pp. 625–632.

[84] Gounder, J. D., Kourmatzis, A., and Masri, A. R., 2012, "Turbulent Piloted Dilute Spray Flames: Flow Fields and Droplet Dynamics," Combust. Flame, **159**(11), pp. 3372–3397.

[85] Lowe, A., Kourmatzis, A., and Masri, A. R., 2017, "Turbulent Spray Flames of Intermediate Density: Stability and near-Field Structure," Combust. Flame, **176**, pp. 511–520.

[86] Adrian, R. J., 2010, “Closing In on Models of Wall Turbulence,” Science (80-.)., **329**(5988), pp. 155–156.

[87] Marusic, I., McKeon, B. J., Monkewitz, P. A., Nagib, H. M., Smits, A. J., and Sreenivasan, K. R., 2010, “Wall-Bounded Turbulent Flows at High Reynolds Numbers: Recent Advances and Key Issues,” Phys. Fluids, **22**(6), p. 065103.

[88] Moin, P., and Mahesh, K., 1998, “Direct Numerical Simulation: A Tool in Turbulence Research,” Annu. Rev. Fluid Mech., **30**(1), pp. 539–578.

[89] Mansour, N. N., Kim, J., and Moin, P., 1988, “Reynolds-Stress and Dissipation-Rate Budgets in a Turbulent Channel Flow,” J. Fluid Mech., **194**(1), pp. 15–44.

[90] Lee, M., and Moser, R. D., 2015, “Direct Numerical Simulation of Turbulent Channel Flow up to $Re\tau \approx 5200$,” J. Fluid Mech., **774**, pp. 395–415.

[91] Kim, J., Moin, P., and Moser, R., 1987, “Turbulence Statistics in Fully Developed Channel Flow at Low Reynolds Number,” J. Fluid Mech., **177**, pp. 133–166.

[92] Spalart, P. R., 1988, “Direct Simulation of a Turbulent Boundary Layer up to $R\theta = 1410$,” J. Fluid Mech., **187**, pp. 61–98.

[93] Kitsios, V., Atkinson, C., Sillero, J. A., Borrell, G., Gungor, A. G., Jiménez, J., and Soria, J., 2016, “Direct Numerical Simulation of a Self-Similar Adverse Pressure Gradient Turbulent Boundary Layer,” Int. J. Heat Fluid Flow, **61**, pp. 129–136.

[94] Nygård, F., and Andersson, H. I., 2009, “DNS of Swirling Turbulent Pipe Flow,” Int. J. Numer. Methods Fluids, **38**(3), pp. 945–972.

[95] Graham, J., Kanov, K., Yang, X. I. A., Lee, M. K., Malaya, N., Lalescu, C. C., Burns, R., Eyink, G., Szalay, A., Moser, R. D., and Meneveau, C., 2016, “A Web Services Accessible Database of Turbulent Channel Flow and Its Use for Testing a New Integral Wall Model for LES,” J. Turbul., **17**(2), pp. 181–215.

[96] Na, Y., Hanratty, T. J., and Liu, Z. C., 2001, “The Use of DNS to Define Stress Producing Events for Turbulent Flow over a Smooth Wall,” Flow, Turbul. Combust., **66**(4), pp. 495–512.

[97] Moser, R. D., Kim, J., and Mansour, N. N., 1999, “Direct Numerical Simulation of Turbulent Channel Flow up to $Re\tau=590$,” Phys. Fluids, **11**(4), pp. 943–945.

[98] Iwamoto, K., Suzuki, Y., and Kasagi, N., 2002, “Reynolds Number Effect on Wall Turbulence: Toward Effective Feedback Control,” Int. J. Heat Fluid Flow, **23**(5), pp. 678–689.

[99] Marusic, I., and Monty, J. P., 2019, “Attached Eddy Model of Wall Turbulence,” Annu. Rev. Fluid Mech., **51**(1), pp. 49–74.

[100] Klewicki, J., Fife, P., and Wei, T., 2009, “On the Logarithmic Mean Profile,” J. Fluid Mech., **638**, pp. 73–93.

[101] Lee, T. W., 2018, “The Reynolds Stress in Turbulence from a Lagrangian Perspective,” J. Phys. Commun., **2**(5).

[102] Lee, T.-W., and Park, J. E., 2017, “Integral Formula for Determination of the Reynolds Stress in Canonical Flow Geometries,” *Progress in Turbulence VII. Springer Proceedings in Physics*, J. Örlü, R., Talamelli, A., Oberlack, M., Peinke, ed., Springer International Publishing, pp. 147–152.

[103] Lee, T. W., 2020, “Lagrangian Transport Equations and an Iterative Solution Method for Turbulent Jet Flows,” Phys. D Nonlinear Phenom., **403**, p. 132333.

[104] Lee, T.-W., 2020, “A Generalizable Theory for the Reynolds Stress, Based on the Lagrangian Turbulence Transport,” arXiv:1708.00966 [Online]. Available: http://arxiv.org/abs/2006.01634.

[105] Lee, T., 2020, “Lognormality in Turbulence Energy Spectra,” Entropy, **22**(6), p. 669.

[106] Lee, T.-W., and Park, J. E., 2021, “Entropy and Turbulence Structure,” Entropy, **24**(1), p. 11.

[107] Lee, T.-W., 2021, “Dissipation Scaling and Structural Order in Turbulent Channel Flows,” Phys. Fluids, **33**(5), p. 055105.

[108] Panton, R. L., 2013, *Incompressible Flow.*, John Wiley & Sons, Incorporated, Somerset.

[109] Pope, S. B., 2000, *Turbulent Flows*, Cambridge University Press.

[110] Hultmark, M., Bailey, S. C. C., and Smits, A. J., 2010, “Scaling of Near-Wall Turbulence in Pipe Flow,” J. Fluid Mech., **649**, pp. 103–113.

[111] De Graaff, D. B., and Eaton, J. K., 2000, “Reynolds-Number Scaling of the Flat-Plate Turbulent Boundary Layer,” J. Fluid Mech., **422**, pp. 319–346.

[112] Barenblatt, G. I., Chorin, A. J., and Prostokishin, V. M., 1997, “Scaling Laws for Fully Developed Turbulent Flow in Pipes,” Appl. Mech. Rev., **50**(7), pp. 413–429.

[113] Hutchins, N., Nickels, T. B., Marusic, I., and Chong, M. S., 2009, "Hot-Wire Spatial Resolution Issues in Wall-Bounded Turbulence," J. Fluid Mech., **635**, pp. 103–136.

[114] Smits, A. J., McKeon, B. J., and Marusic, I., 2011, "High–Reynolds Number Wall Turbulence," Annu. Rev. Fluid Mech., **43**(1), pp. 353–375.

[115] Fernholz, H. H., and Finley, P. J., 1996, "The Incompressible Zero-Pressure-Gradient Turbulent Boundary Layer: An Assessment of the Data," Prog. Aerosp. Sci., **32**(4), pp. 245–311.

[116] Frisch, U., 1995, *Turbulence: The Legacy of A. N. Kolmogorov*, Cambridge University Press.

[117] Kolmogorov, A. N., 1968, "Local Structure of Turbulence in an Incompressible Viscous Fluid at Very High Reynolds Numbers," Sov. Phys. Uspekhi, **10**, pp. 734–746.

[118] Orszag, S. A., 1970, "Analytical Theories of Turbulence," J. Fluid Mech., **41**(2), pp. 363–386.

[119] Boffetta, G., and Ecke, R. E., 2012, "Two-Dimensional Turbulence," Annu. Rev. Fluid Mech., **44**(1), pp. 427–451.

[120] Kraichnan, R. H., 1959, "The Structure of Isotropic Turbulence at Very High Reynolds Numbers," J. Fluid Mech., **5**(04), p. 497.

[121] Brown, T. M., 1982, "Information Theory and the Spectrum of Isotropic Turbulence," J. Phys. A. Math. Gen., **15**(7), pp. 2285–2306.

[122] Verkley, W. T. M., and Lynch, P., 2009, "Energy and Enstrophy Spectra of Geostrophic Turbulent Flows Derived from a Maximum Entropy Principle," J. Atmos. Sci., **66**(8), pp. 2216–2236.

[123] Planck, M., 1901, "On the Law of the Energy Distribution in the Normal Spectrum," Phys, Ann, **4**, p. 553.

[124] Conrad, K., 2004, "Probability Distributions and Maximum Entropy," online note, https://kconrad.math.uconn.edu/blurbs/analysis/entropypost.pdf.

[125] Comte-Bellot, G., and Corrsin, S., 1971, "Simple Eulerian Time Correlation of Full-and Narrow-Band Velocity Signals in Grid-Generated, 'Isotropic' Turbulence," J. Fluid Mech., **48**(2), pp. 273–337.

[126] Uberoi, M. S., and Freymuth, P., 1969, “Spectra of Turbulence in Wakes behind Circular Cylinders,” Phys. Fluids, **12**(7), p. 1359.

[127] Tieleman, H. W., 1967, “Viscous Region of Turbulent Boundary Layer,” Ph.D. dissertation, Colorado State University, Fort Collins, CO.

[128] Saddoughi, S. G., and Veeravalli, S. V., 1994, “Local Isotropy in Turbulent Boundary Layers at High Reynolds Number,” J. Fluid Mech., **268**, pp. 333–372.

[129] Kang, H. S., Chester, S., and Meneveau, C., 2003, “Decaying Turbulence in an Active-Grid-Generated Flow and Comparisons with Large-Eddy Simulation,” J. Fluid Mech., **480**, pp. 129–160.

[130] Tung, K. K., and Orlando, W. W., 2003, “The k −3 and k −5/3 Energy Spectrum of Atmospheric Turbulence: Quasigeostrophic Two-Level Model Simulation,” J. Atmos. Sci., **60**(6), pp. 824–835.

[131] Nastrom, G. D., and Gage, K. S., 1985, “A Climatology of Atmospheric Wavenumber Spectra of Wind and Temperature Observed by Commercial Aircraft.,” J. Atmos. Sci., **42**(9), pp. 950–960.

APPENDIX A

DERIVATION OF MOMENTUM EQUATIONS

The momentum balance within a spray control volume is considered. Let u_L(x, t) denote the average velocity for the local spray structure of liquid in the control volume. It is assumed that asymptotic status is reached inside the control volume, starting from the inlet plane to just before the primary break-up where it yields at the end of the control volume called the exit plane. Accordingly, it approximates u_L(x, t) ~ u_L(x). The most prominent factor considered in the momentum exchange between liquid and gas, is the aerodynamic drag force. And let the drag coefficient C_D encompass any other momentum effects from surface tension or viscous force. Gravity is also neglected.

Case 1: Liquid Injection into an Initially Quiescent Gas Surrounding

The momentum of the liquid is subjected to the drag force by the surrounding gas. Since the spray velocity is of interest, it is assumed that the local liquid mass is distributed without being varied significantly, at the stage of the primary breakup. The momentum balance is written as,

$$m_L \frac{du_L}{dt} = F_D \qquad \text{Eq. (A.1)}$$

In Eq. (A.1), m_L and F_D denote liquid mass and drag force respectively, and du_L/dt is changed its expression in term of a spatial derivative. Those are presented as Eq. (A.2), Eq. (A.3), and Eq. (A.4).

$$m_L = \rho_L V_s \qquad \text{Eq. (A.2)}$$

$$F_D = -\frac{C_D}{2}\rho_g\left(u_L - u_g\right)^2 A_D \qquad \text{Eq. (A.3)}$$

$$\frac{du_L}{dt} = \frac{\partial u_L}{\partial x}\frac{dx}{dt} + \frac{\partial u_L}{\partial t} = \frac{du_L}{dx}u_L \qquad \text{Eq. (A.4)}$$

The local spray volume V_s in Eq. (A.2), and the local spray area A_D subjected to the drag force effectively in Eq. (A.3), are used. The rate of velocity is shown in the spatial derivative form as Eq. (A.4). The arrangement of them into Eq. (A.1) leads to the liquid momentum equation as in Eq. (A.5), which is corresponding to the Eq. (4.1).

Liquid $$u_L\frac{du_L}{dx} = -\frac{C_D}{2}\frac{\rho_g}{\rho_L}\frac{A_D}{V_s}\left(u_L - u_g\right)^2 \qquad \text{Eq. (A.5)}$$

The gas momentum is influenced by the drag force in addition to the gas entrainment effect that would appear in the form of pressure force. The gas momentum balance is written as Eq. (A.6).

$$\frac{d}{dt}\left(m_g u_g\right) = F_D + F_p = 0 \qquad \text{Eq. (A.6)}$$

In Eq. (A.6), the gas momentum is balanced between the pressure force and the drag force. The pressure force F_p is represented as in Eq. (A.7). The local spray projection area A_p is used, which is subjected to the pressure force effectively in Eq. (A.7). Note that the sign of Δp is negative.

$$F_p = -\Delta p\, A_p = \rho_g u_g^2\, A_p \qquad \text{Eq. (A.7)}$$

The arrangement for both Eq. (A.3) and Eq. (A.7) into Eq. (A.6) leads to the expression of the gas momentum equation as in Eq. (A.8), which is corresponding to Eq. (4.2).

Gas $$\rho_g u_g^2 A_p = \frac{C_D}{2} \rho_g A_D \left(u_L - u_g\right)^2 \qquad \text{Eq. (A.8)}$$

Case 2: Liquid Injection with Added Gas Momentum of Co-Flowing of Gas

Let $u_{L,x}$ denotes the average velocity for the whole continuous spray structure of liquid in the control volume whose status is asymptotic. In a similar approach, the momentum balance mainly depends on the aerodynamic drag force. The effect of gas entrainment is assumed to be negligible when it is compared to that of an initially quiescent gas surrounding. When it comes to the gas-driven type of spray atomization, high input gas momentum is generally preferred since a more destructive breakup is expected if desired. The momentum balance is written for liquid and gas simultaneously between inlet and exit of the system as in Eq. (A.9). Each of the corresponding momentums is delineated as Eq. (A.10), and its arrangement into Eq. (A.9) results in Eq. (A.11).

$$\frac{d}{dt}(mv)_i = \frac{d}{dt}(mv)_e \qquad \text{Eq. (A.9)}$$

$$(mv)_i = m_L u_{inj} + m_g u_{in} \qquad (mv)_e = m_L u_{L,x} + m_g u_{out} \qquad \text{Eq. (A.10)}$$

$$u_{inj}\frac{dm_L}{dt} + u_{in}\frac{dm_g}{dt} = u_{L,x}\frac{dm_L}{dt} + u_{out}\frac{dm_g}{dt} \qquad \text{Eq. (A.11)}$$

or equivalently,

$$\dot{m}_L u_{inj} + \dot{m}_g u_{in} = \dot{m}_L u_{L,x} + \dot{m}_g u_{out}$$

In the meanwhile, the drag force is derived from the change in the rate of momentum for gas as shown in Eq. (A.12). And this relation is regarded as the momentum balance of gas.

$$\dot{m}_g(u_{in} - u_{out}) = -F_D \qquad \text{Eq. (A.12)}$$

Therefore, the momentum balance for liquid is obtainable by Eq. (A.11) and Eq. (A.12), which is shown in Eq. (A.13).

$$\dot{m}_L(u_{L,x} - u_{inj}) = -F_D \qquad \text{Eq. (A.13)}$$

In Eq. (A.12) and Eq. (A.13), $\dot{m}_L$, $\dot{m}_g$, and F_D denote mass flow rate of liquid, gas, and drag force respectively. Those are presented as Eq. (A.14) and Eq. (A.15).

$$F_D = -\frac{C_D}{2}\rho_g(u_{in} - u_{L,x})^2 A_D \qquad \text{Eq. (A.14)}$$

$$\dot{m}_L = \rho_L u_{inj} A_{inj} \qquad \dot{m}_g = \rho_g u_{in} A_{in} \qquad \text{Eq. (A.15)}$$

The projection area for the whole spray structure A_D is used, which is subjected to the drag force effectively in Eq. (A.14). The arrangement for both Eq. (A.14) and Eq. (A.15) into Eq. (A.13) and Eq. (A.12) leads to the expression of the momentum equation for liquid and gas, respectively. The results appear in Eq. (A.16) and Eq. (A.17), which are corresponding to Eq.(4.3) and Eq. (4.4).

Liquid $$\rho_L u_{inj} A_{inj}\left(u_{L,x} - u_{inj}\right) = \frac{C_D}{2}\rho_g A_D \left(u_{in} - u_{L,x}\right)^2 \quad \text{Eq. (A.16)}$$

Gas $$\rho_g u_{in}^2 A_{in} = \rho_g u_{in} A_{in} u_{out} + \frac{C_D}{2}\rho_g A_D \left(u_{in} - u_{L,x}\right)^2 \quad \text{Eq. (A.17)}$$

Details of Spatial Integration for Case 1

Fig. 4.1 has shown the momentum exchanges between liquid and gas via drag force, which is the result of spatial integration of the momentum equations for Case 1. Fig. 4.1 has been presented to prove the usability of the momentum balance with a simple spray as the example; ρ_L = 1000 kg/m^3, ρ_g = 1.225 kg/m^3, u_{inj} = 120 m/s, d_{inj} = 0.3mm. The numerical calculations for u_L and u_g by the aid of spatial integration are suggested as follows.

Liquid $$u_{L,i+1} = u_{L,i} - \frac{\Delta x_i}{u_{L,i}}\left[\frac{C_{D,i+1}}{2}\frac{\rho_g}{\rho_L}\left(\frac{A_D}{V_s}\right)_{i+1}\left(u_{L,i} - u_{g,i}\right)^2\right] \quad \text{Eq. (A.18)}$$

Gas $$u_{g,i+1} = \sqrt{\frac{C_{D,i+1}}{2}\left(\frac{A_D}{A_p}\right)_{i+1}\left(u_{L,i} - u_{g,i}\right)^2} \quad \text{Eq. (A.19)}$$

Eq. (A.18) and Eq. (A.19) are shown in the expression with the discretizational form of Eq. (A.5) and Eq. (A.8), for liquid and gas respectively. The elusive parameters to determine in the implementations are C_D, (A_D/V_s), and $\left(A_D/A_p\right)$, these are dependent on the distance from the injection, i.e., the x variable.

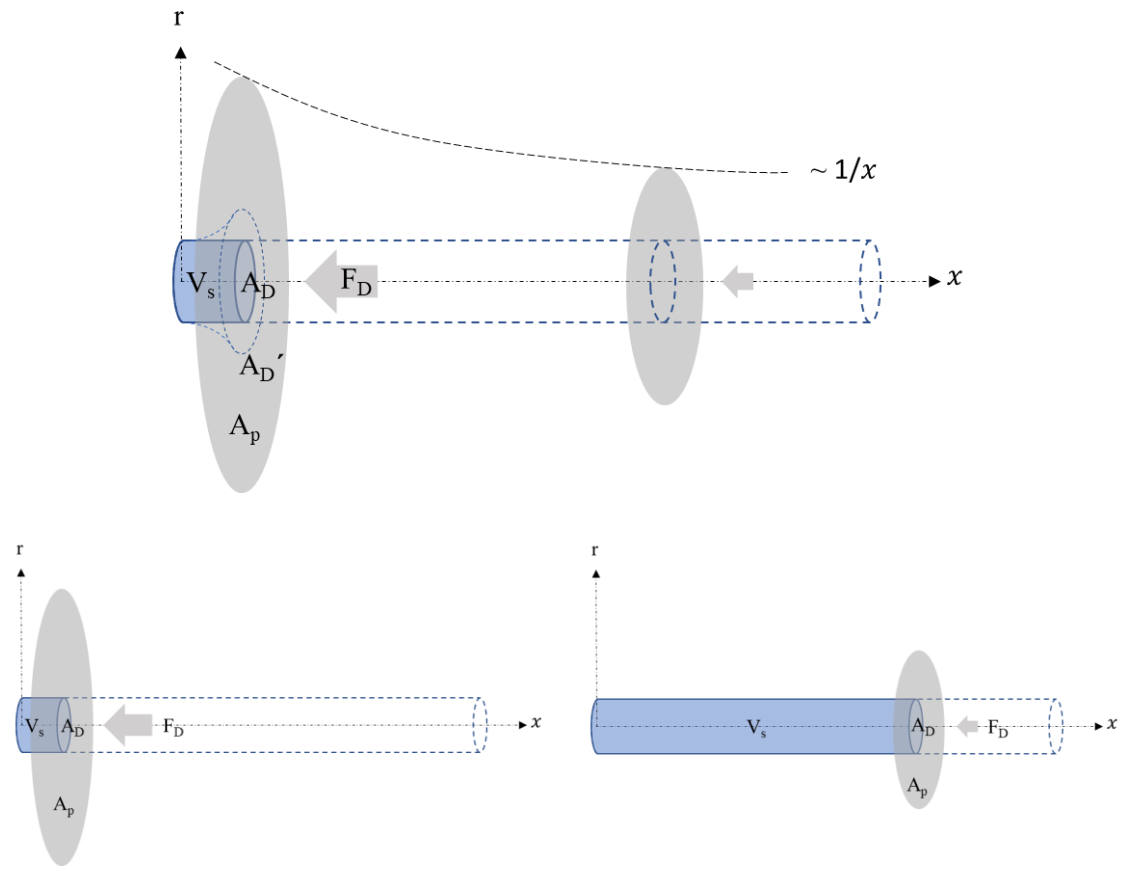

Fig. (A.1) Description of reduction in drag force to the local spray volume for Case 1

Fig. (A.1) illustrates the decrease in drag force with respect to x, and it corresponds to the pressure force as stated in the previous context. To simplify this approach, let Δp be a constant for a local spray volume V_s. This assumption enables us to express the extent of the drag force effect by solely the size of the area subjected to the

pressure force A_p. To circumvent complicated calculations, let A_p ~ 1/ x^2. Moreover, the local spray volume is considered in a shape of a cylinder, which allows the frontal area of the local spray volume A_D to be a constant. This leads to (A_D/V_s) ~ $1/x$ and $\left(A_D/A_p\right)$ ~ x^2. Besides, C_D is assumed to be a monotonic change in x, such that it spans a certain range of trial values.

In taking account of the increase in ambient density as depicted in Fig. 4.1, e.g., $2\rho_g$ and $5\rho_g$, the use of augmented A_D is suggested as the reflection of elevated drag force caused by the denser ambient. In the experimental observations by Shimizu et al., 1984, [59], they described that spray angle increases as the ambient pressure increases, implying the effect from denser ambient. Lefebvre et al., 2017 [29] also prescribed the increase in aerodynamic drag on the resultant droplets by an increase in gas density, with the tendency of a greater deceleration in the axial direction than in the radial direction. Accordingly, this is illustrated in Fig. (A.1) as showing the wider spreading in the frontal area $A_D{}'$ than A_D, and the A_D is when resides in the reference ambient $1\rho_g$.